

EXPERIMENTAL AND NUMERICAL INVESTIGATION OF CFS-CONCRETE  
COMPOSITE TRUSSES

A THESIS SUBMITTED TO  
THE GRADUATE SCHOOL OF APPLIED SCIENCES  
OF  
MIDDLE EAST TECHNICAL UNIVERSITY

BY  
HAZAL GÜLDÜR

IN PARTIAL FULFILLMENT OF THE REQUIREMENTS  
FOR  
THE DEGREE OF MASTER OF SCIENCE  
IN  
CIVIL ENGINEERING

JULY 2018



Approval of the thesis:

**EXPERIMENTAL AND NUMERICAL INVESTIGATION OF CFS-  
CONCRETE COMPOSITE TRUSSES**

submitted by **HAZAL GÜLDÜR** in partial fulfillment of the requirements for the degree of **Master of Science in Civil Engineering Department, Middle East Technical University** by,

Prof. Dr. Halil Kalıpçılar  
Dean, Graduate School of **Natural and Applied Sciences**

\_\_\_\_\_

Prof. Dr. İsmail Özgür Yaman  
Head of Department, **Civil Engineering**

\_\_\_\_\_

Assoc. Prof. Dr. Eray Baran  
Supervisor, **Civil Engineering Dept., METU**

\_\_\_\_\_

**Examining Committee Members:**

Prof. Dr. Cem Topkaya  
Civil Engineering Dept., METU

\_\_\_\_\_

Assoc. Prof. Dr. Eray Baran  
Civil Engineering Dept., METU

\_\_\_\_\_

Prof. Dr. Kağan Tuncay  
Civil Engineering Dept., METU

\_\_\_\_\_

Assoc. Prof. Dr. Ozan Cem Çelik  
Civil Engineering Dept., METU

\_\_\_\_\_

Asst. Prof. Dr. Saeid Kazemzadeh Azad  
Civil Engineering Dept., Atılım University

\_\_\_\_\_

**Date:** 27.07.2018

**I hereby declare that all information in this document has been obtained and presented in accordance with academic rules and ethical conduct. I also declare that, as required by these rules and conduct, I have fully cited and referenced all material and results that are not original to this work.**

Name, Last name: Hazal Gldr

Signature:

## **ABSTRACT**

### **EXPERIMENTAL AND NUMERICAL INVESTIGATION OF CFS- CONCRETE COMPOSITE TRUSSES**

Güldür, Hazal  
M. Sc., Department of Civil Engineering  
Supervisor: Assoc. Prof. Dr. Eray Baran

July 2018, 96 pages

Cold-formed steel (CFS) structural systems have been intensely studied especially due to the economy and ease of implementation that they provide. A common failure mode of CFS members is the local instability of the section. The aim of this study is to control the local instability in CFS floor trusses by providing concrete infill inside compression chord members. Numerical and experimental studies were conducted in order to investigate the flexural behavior of steel-concrete composite trusses made of CFS sections. Main test parameters were the presence of concrete infill, orientation of top chord CFS member, presence of shear enhancing connectors, and the presence of a concrete slab. The finite element (FE) model of the CFS floor trusses was created and three types of analysis, namely Materially Nonlinear Analysis (MNA), Geometrically and Materially Nonlinear Analysis (GMNA) and Geometrically and Materially Nonlinear Analysis with Imperfections (GMNIA), were conducted. While the FE model was able to simulate the actual strain behavior for the stiffened elements of the compression chord CFS section, the measured and numerically predicted strain values differ significantly for the lip part of the section. Additional analytical studies were conducted in order to predict the behavior of composite trusses without the need

of detailed analysis or load tests. The procedure adopted for the analytical approach is based on calculating the chord cross-sectional strain and then determining the initial stiffness, yield and maximum load capacities using this strain information.

**Keywords:** Thin-Walled Member, Cold-Formed Steel, Steel-Concrete Composite CFS, CFS truss, CFS flooring system

## ÖZ

### **HAFİF ÇELİK PROFİLLER VE BETONDAN OLUŞAN KOMPOZİT KAFES KİRİŞLERİNİN DENEYSEL VE ANALİTİK OLARAK İNCELENMESİ**

Güldür, Hazal  
Yüksek Lisans, İnşaat Mühendisliği Bölümü  
Tez Yöneticisi: Doç. Dr. Eray Baran

Temmuz 2018, 96 sayfa

Hafif çelik yapısal sistemler, sağladıkları ekonomi ve uygulama kolaylığı gibi avantajlar nedeniyle son zamanlarda yoğun bir şekilde çalışılmaya başlanmıştır. Hafif çelik yapısal elemanlarda sıklıkla görülen göçme biçimi kesitte oluşan lokal burkulmadır. Bu çalışmada, basınç başlığı elemanlarının içerisine beton dolgu yerleştirilerek hafif çelik kafes kirişlerinde lokal burkulmaların kontrol edilmesi incelenmiştir. Bu şekilde oluşturulmuş kompozit kirişlerin eğilme davranışlarının incelenmesi amacıyla nümerik ve deneysel çalışmalar yapılmıştır. Başlıca deney parametreleri, beton dolgu, basınç başlığı yerleşimi, kesme elemanlarının ve beton döşemenin varlığı olarak belirlenmiştir. Hazırlanan sonlu elemanlar modelinde Doğrusal Olmayan Malzeme Analizi (MNA), Doğrusal Olmayan Malzeme ve Geometri Analizi (MGNA) ve Geometrik Kusurlar ile Doğrusal Olmayan Malzeme Analizi (MGNA) olarak üç tip analiz gerçekleştirilmiştir. Sonlu elemanlar modeli güçlendirilmiş elemanlarda gerçek gerinim davranışını simüle etmekte başarılı olsa da, elemanın dudak kısmında nümerik olarak belirlenen ile deney sonuçları arasında

önemli farklılıklar bulunmaktadır. Kompozit kafes kirişlerinin davranışlarının öngörülebilmesi ve detaylı analiz ve deneylere gerek kalmadan belirlenebilmesi için analitik çalışmalar yapılmıştır. Analitik çalışmanın prosedürü başlık kesitsel gerinim değerlerinin belirlenmesine ve buna bağlı olarak başlangıç rijitliği, akma ve maksimum yük değerlerinin belirlenmesine dayanmaktadır.

**Anahtar Kelimeler:** İnce Cidarlı Elemanlar, Hafif Çelik, Çelik-Beton Kompozit, Hafif Çelik Kafes Sistemler, Hafif Çelik Döşeme Sistemler



*To My Mother...*

## ACKNOWLEDGEMENTS

I would first like to thank my thesis advisor Dr. Eray Baran for his support and encouragement. The door to his office was always open whenever I ran into a trouble spot or had a question about my research or writing. He consistently allowed this thesis to be my own work, but steered me in the right direction whenever he thought I needed it.

I would also like to thank Dr. Cem Topkaya who was involved in the numerical analysis and the results of the experiments for this research. He has provided a throughout endorsement in the analysis of the results and the reached conclusions.

The research assistant at the Middle East Technical University Mert Pehlivan has always been there during the experiments and helped for the experiments to be conducted correctly. I would also like to thank Korhan Kocamaz for his great support, he has been there for me in every problem I faced and every breakdown. He has been only supportive in any way possible. The friends at the Middle East Technical University İrem Ağaçcıođlu, Beyazıt Bestami Aydın, Gökben Demir, Münci Tunç Kalaycıođlu, Müge Özgenođlu, Başak Seyisođlu, Güncel Vara have been a great support, listened to me at every problem and encouraged me. Also the help of the laboratory technicians could not be neglected. The experiments conducted have all been prepared with their help.

I would like to thank my friends Nilya Bengül, Çađan Dizdar, Rengin Günaydın, Ömer Cem Kaya, Koray Solak, Ceren Sarıbyık, İtır Özinanır Sarıhan, Sinem Şenyurt and Tuğçe Uçar that have always been there my whole life, made me feel their support even when they are not near, and forgave me for my absence.

The final gratitude belongs to my family, that have always encouraged me and let me see and experience things I would not have imagined. They have been my greatest mentor and advisor. Without their help and support I would not have achieved to be where I am at the moment.

## TABLE OF CONTENTS

ABSTRACT.....	v
ÖZ.....	vii
ACKNOWLEDGEMENTS .....	x
TABLE OF CONTENTS .....	xi
LIST OF TABLES .....	xiv
LIST OF FIGURES .....	xv
CHAPTERS	
1. INTRODUCTION AND LITERATURE REVIEW.....	1
1.1. Introduction .....	1
1.2. Cold Formed Steel Members.....	2
1.2.1. Material Properties .....	2
1.2.2. Geometric Imperfections.....	5
1.3. Design Methods for Thin-Walled Members.....	7
1.3.1. Effective Width Method.....	8
1.3.2. Direct Strength Method.....	11
1.4. CFS Trusses .....	12
1.5. Concrete CFS Composite Systems .....	13
1.6. Aim and Objective.....	15
1.7. Thesis Outline.....	15
2. EXPERIMENTAL STUDY.....	17
2.1. Truss Specimens .....	17
2.2. Experimental Setup.....	25

2.3.	Load Test Results .....	28
2.3.1.	Observed Failure Modes .....	28
2.3.2.	Effect of Top Chord Orientation .....	30
2.3.3.	Effect of Concrete Infill .....	31
2.3.4.	Effect of Shear Enhancements .....	34
2.3.5.	Effect of Concrete Slab .....	36
3.	FINITE ELEMENT MODELLING.....	39
3.1.	Description of Finite Element Model .....	39
3.1.1.	Analysis Methods.....	44
3.2.	Analysis Results .....	45
3.2.1.	Bare CFS Specimens.....	45
3.2.1.1.	Specimen WT_Control.....	45
3.2.1.2.	Specimen WB_Control .....	52
3.2.2.	Concrete Infilled Specimens .....	55
3.2.2.1	Specimens WT_C_0 and WT_C_100.....	55
3.2.2.2.	Specimens WB_C_0 and WB_C_100 .....	60
3.2.2.4.	Specimen WB_Slab .....	64
4.	ANALYTICAL STUDIES .....	69
4.1.	Calculation of Cross-Sectional Strains .....	70
4.1.1.	Bare CFS Trusses .....	72
4.1.2.	Concrete Infilled Trusses .....	76
4.1.3.	Truss with Concrete Slab .....	79
4.2.	Truss Stiffness and Load Capacity Predictions .....	81
4.2.1.	Comparison of Analytically Determined and Measured Responses.....	85

5. SUMMARY AND CONCLUSIONS .....	89
REFERENCES.....	93

## LIST OF TABLES

### TABLES

Table 1. Truss top chord configurations used in specimens .....	21
Table 2. Details of cross-sectional strain calculations .....	73
Table 3. Estimated maximum strain and strength values.....	83
Table 4. Truss cross-sectional properties .....	85
Table 5. Measured and the predicted yield and ultimate load values for trusses WT_C and WT_C_100 .....	87
Table 6. Measured and the predicted yield and ultimate load values for trusses WB_C and WB_C_100 .....	88
Table 7. Measured and the predicted yield and ultimate load values for truss WB_Slab .....	88

## LIST OF FIGURES

### FIGURES

Figure 1. Cold-forming process; (a) roll-forming [2], (b) press-braking [3] .....	2
Figure 2. Typical stress-strain curves: (a) hot-rolled steel, (b) CFS [1].....	3
Figure 3. Stress-Strain curves obtained from coupon tests [6] .....	4
Figure 4. Definition of geometric imperfection types [10] .....	6
Figure 5. Buckling modes of a lipped channel section: (a) local buckling, (b) distortional buckling, (c) global buckling .....	7
Figure 6. Post-buckling strength model [17].....	9
Figure 7. Stress distribution in stiffened compression elements.....	9
Figure 8. Stiffened (a) and Unstiffened (b) element subjected to uniform compression [14] .....	10
Figure 9. Signature curve of a lipped channel section [21].....	12
Figure 10. CFS section dimensions.....	17
Figure 11. Geometric details of the truss configuration.....	18
Figure 12. Specimen WT_Control (a) and WB_Control (b).....	18
Figure 13. The effect of number of connection screws on truss response [30].....	19
Figure 14. Screw and rivet used in truss specimens.....	20
Figure 15. Specimen WT_C (a) and WB_C (b).....	22
Figure 16. Specimen WB_Slab .....	23
Figure 17. Tested coupon samples .....	24

Figure 18. Stress-strain behavior obtained from coupon samples .....	24
Figure 19. Schematics of experimental setup.....	25
Figure 20. Detail used at loading points.....	26
Figure 21. Experimental setup .....	27
Figure 22. Strain gages attached on CFS member .....	27
Figure 23. Failure shape: (a) WT_Control, (b) WB_Control.....	28
Figure 24. Deformed shape of specimen WB_Slab .....	29
Figure 25. Concrete cracking in specimen WB_Slab .....	29
Figure 26. Effect of top chord orientation (load-midspan deflection) .....	30
Figure 27. Effect of top chord orientation (strut force-midspan deflection).....	31
Figure 28. Effect of concrete (Specimens WT_C and WB_C).....	32
Figure 29. Effect of concrete infill on midspan section strains.....	33
Figure 30. Effect of shear enhancements .....	34
Figure 31. Effect of shear enhancements on midspan section strains .....	36
Figure 32. Effect of the presence of concrete slab .....	37
Figure 33. Effect of concrete slab on midspan section strains .....	38
Figure 34. Finite element model for bare truss .....	39
Figure 35. Finite element model for truss with concrete slab .....	40
Figure 36. Elements used in FE models: (a) Shell 181, (b) Beam 188 [32] .....	41
Figure 37. Geometry for Solid 186 element [32].....	41
Figure 38. Steel material model used in FE analyses.....	43
Figure 39. Path locations to extract cross-sectional strains in FE model.....	45
Figure 40. Measured and predicted load-deflection response of specimen WT_Control .....	46



Figure 41. Specimen WT_Control deformed shape: (a) MGNA, (b) MGNIA.....	46
Figure 42. Strain gage locations in specimen WT_Control .....	47
Figure 43. Top chord load-strain response in specimen WT_Control.....	48
Figure 44. Bottom chord load-strain response in specimen WT_Control.....	49
Figure 45. Specimen WT_Control top chord midspan strain values; experiment vs. model values.....	50
Figure 46. Specimen WT_Control bottom chord midspan strain values; experiment vs. model values .....	51
Figure 47. Measured and predicted load-deflection response of specimen WB_Control .....	52
Figure 48. Specimen WB_Control deformed shape: (a) MGNA, (b) MGNIA.....	53
Figure 49. Specimen WB_Control top chord midspan strain distribution.....	54
Figure 50. Specimen WB_Control bottom chord midspan strain distribution.....	54
Figure 51. Measured and predicted load-deflection response of Specimen WT_C.	55
Figure 52. Specimen WT_C strain gage locations.....	56
Figure 53. Top chord load-strain response in specimen WT_C.....	58
Figure 54. Bottom chord load-strain response in specimen WT_C .....	58
Figure 55. Specimen WT_C numerically determined and experimentally measured top chord strain distribution .....	59
Figure 56. Specimen WT_C numerically determined bottom chord strain distribution .....	60
Figure 57. Measured and predicted load-deflection response of specimen WB_C .	61
Figure 58. Specimen WB_C strain gage locations.....	62
Figure 59. Top chord load-strain response in specimen WB_C .....	62
Figure 60. Bottom chord load-strain response in specimen WB_C.....	63

Figure 61. Specimen WB_C numerically determined and experimentally measured top chord strain distribution .....	63
Figure 62. Specimen WB_C numerically determined bottom chord strain distribution .....	64
Figure 63. Measured and predicted load-deflection response of specimen WB_Slab .....	65
Figure 64. Specimen WB_Slab strain gage locations .....	66
Figure 65. Top chord load-strain response in specimen WB_Slab .....	66
Figure 66. Bottom chord load-strain response in specimen WB_Slab .....	67
Figure 67. Specimen WB_Slab bottom chord midspan strain values; experiment vs. model values.....	68
Figure 68. Cross-sectional strains due to axial and bending effects .....	70
Figure 69. Truss external moment due to two-point and distributed loading .....	71
Figure 70. Truss WT_Control comparison of estimated chord strains .....	74
Figure 71. Truss WB_Control comparison of estimated chord strains .....	75
Figure 72. Truss WT_C comparison of estimated chord strains.....	77
Figure 73. Truss WB_C comparison of estimated chord strains.....	78
Figure 74. Truss WB_slab comparison of estimated chord strains.....	80
Figure 75. Schematic analytical calculation assumptions: (a) yield load, (b) ultimate load.....	82
Figure 76. Determination of maximum bottom chord stress using idealized stress-strain behavior.....	83
Figure 77. Cross-sectional geometric properties for trusses .....	84
Figure 78. Comparison of analytical and experimental responses for trusses WT_C and WT_C_100 .....	86

Figure 79. Comparison of analytical and experimental responses for trusses WB_C and WB_C_100.....	86
Figure 80. Comparison of analytical and experimental responses for truss WB_Slab .....	87



## CHAPTER 1

### INTRODUCTION AND LITERATURE REVIEW

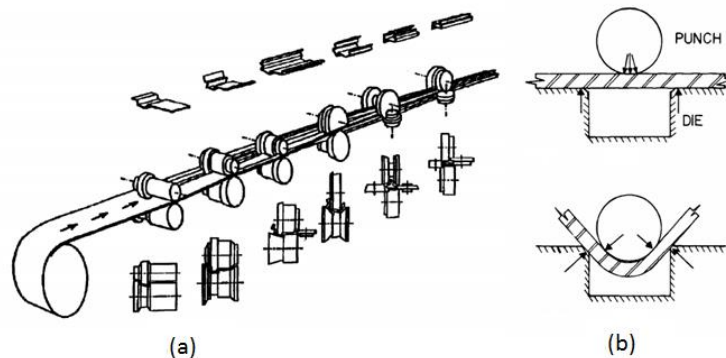
#### 1.1. Introduction

Cold-formed steel (CFS) members have started to be widely used in structural systems since towards the end of the twentieth century, mainly due to the reduced construction duration with ease of fabrication and their much higher strength-to-weight ratio compared to hot-rolled sections. CFS construction produces less waste material and therefore considered to be a greener choice of construction type. The sections are mass produced and transferred to the construction site with less cost and time. They can also be assembled or reassembled at the site. CFS construction is considered to be more economic, environmentally friendly and rapid. Today, the use of cold formed structures has become wider especially for residential, industrial and commercial buildings.

In this chapter a general overview of the research conducted on CFS system properties and behavior is presented. Firstly, the cold-forming procedure and its effects to the material properties are discussed. The stress-strain behavior and how this behavior is affected from the manufacturing procedure is explained. This behavior is a result of yield strength increase and formation of residual stresses. Secondly, the geometric imperfections, which include local deviations, bowing, warping and twisting are stated. The proposed analysis methods for modeling these imperfections in the literature are also presented. This is followed by the design methods of thin-walled structural members. The Effective Width Method and the Direct Strength Method are introduced. Finally, a review of the research conducted on composite flooring systems comprising concrete and CFS is presented.

## 1.2. Cold Formed Steel Members

The most common application method of cold forming is the cold-rolled forming method, where the sections are produced as strips and the section shape is established by letting this strip through a number of rolls without applying heat. A variety of sections with different shapes and thicknesses can be produced this way. The thickness generally ranges between 1.2 and 6.4 mm and the a depth of the section ranges between 51-305 mm [1]. This provides consistent quality and design flexibility for designers. In addition to roll-forming, press-braking method is also being used for fabrication of CFS sections (Figure 1).



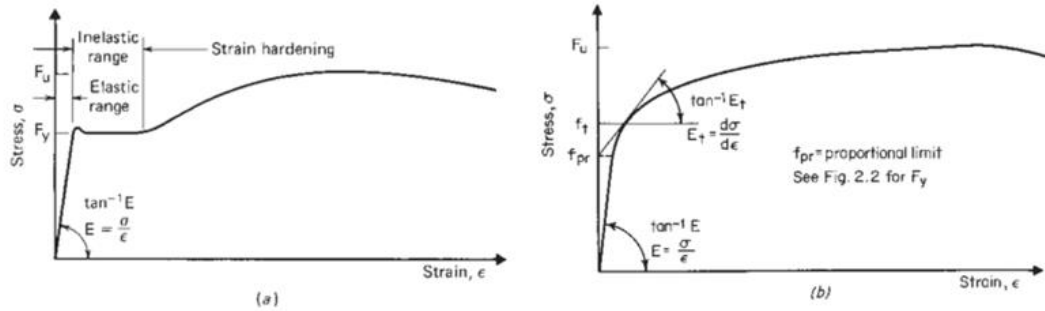
**Figure 1.** Cold-forming process; (a) roll-forming [2], (b) press-braking [3]

### 1.2.1. Material Properties

Investigations on the behavior of CFS members started in the 1960s. The results of the experimental study conducted by Kenneth [3] revealed that cold-forming causes significant increase in the yield strength of the member both at the corners and the flat portion. The yield strength of the corners is always higher due to large plastic deformations.

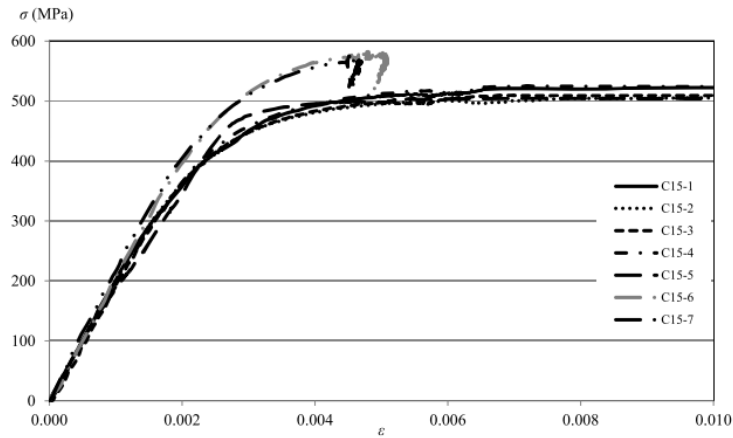
The stress-strain behavior of the cold-formed steel shows differences when compared to the conventional hot-rolled steel. Instead of forming a plateau at the yielding point, the cold-formed steel has a stress-strain response with no definite yield point. Therefore, instead of sharp yielding, it rather exhibits a linear behavior followed by

gradual yielding. The typical stress-strain curves of hot-rolled steel and CFS are presented in Figure 2.



**Figure 2.** Typical stress-strain curves: (a) hot-rolled steel, (b) CFS [1]

The effect of the plastic deformations occurring during the manufacturing of CFS sections has been studied by numerous researchers. Chajes et al. [4] performed an experimental study and concluded that the increase in the yield and ultimate strength is approximately proportional to the amount of cold stretching applied. Karren and Winter [5] investigated the stress-strain behavior of CFS sections. The yield strength of the corners was measured to be larger than the virgin steel strip by up to 102%. This is explained by the different plastic deformations occurring at various fibers with a high range. Therefore, when the corners of the section are tested, the fibers yield at different stresses forming a gradual yielding stress-strain curve. A more recent study conducted by Kyvelou et al. [6] proved not only the increase in yield strength but also the reduction in ductility at the corners of the section. In the study several coupons from a channel section were tested. A comparison of stress-strain behavior obtained from the coupon samples extracted from the corner and flat regions of a CFS channel profile is given in Figure 3. The corner strength was found to be approximately 15% higher than the strength of the flat regions with a significant reduction in ductility.



**Figure 3.** Stress-Strain curves obtained from coupon tests [6]

Presence of residual stresses occurring during forming of CFS shapes is well known. The residual stresses in CFS are caused by bending operations that involve large plastic deformations, as opposed to hot-rolled steel sections, where residual stresses occur due to uneven cooling. Weng and Peköz [7] investigated the residual stresses in CFS sections. They stated that while inner surface of CFS sections is subjected to compressive residual stresses, the outer surface is subjected to tensile residual stresses.

Batista and Rodrigues [8] have investigated the residual stresses by taking strip elements from the mid-section of CFS profiles. They measured the strain using mechanical and electrical strain gages and also calculated the residual stresses through the deflected shape of the strips. Once the strips are cut off from the section, due to the residual stresses they deform and form a curve. From the deflection of the curve; they have calculated the radius of curvature and the strain values at the upper and lower surfaces of the strip. They have concluded that the values of transverse stresses are very low compared to those in the longitudinal direction.

Abdel-Rahman and Sivakumaran [9] have also observed the low magnitude of the transverse residual stresses and suggested that they could be neglected. Two models [7,9] have been proposed on the distribution of the longitudinal residual stresses. The difference between these models is that while Weng and Peköz [7] ignores the

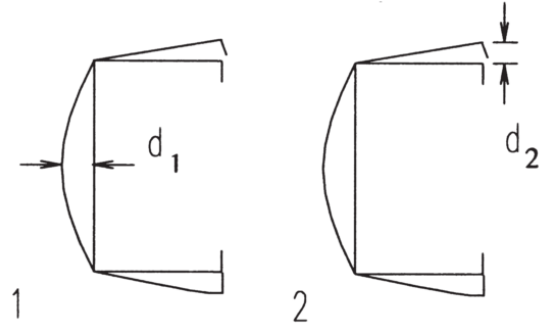


increase of the residual stresses at the corner regions and determines the longitudinal residual stresses as 50% of the yield strength of the flat material; Abdel-Rahman and Sivakumaran [9] has determined the longitudinal residual stresses as 40% of the yield strength of the flat material at the corners and 12-18% of the yield strength of the flat material at the flat region. Both models assume that the longitudinal residual stresses vary linearly along the thickness of the material. The maximum tensile stress is observed at the outer surface and the maximum compression stress is observed at the inner surface. Furthermore, since the membrane component is ignored for the longitudinal residual stresses only the bending component is assumed to be present and the maximum tensile and compressive stresses at the inner and outer surfaces are assumed to be equal in magnitude.

Using the previous assumptions, Schafer and Peköz [10] have determined the longitudinal residual stresses as the summation of the membrane and flexural residual stresses. After their experimental research they have concluded that the membrane residual stresses are not as critical as the flexural residual stresses, which can range up to 50% of the yield strength. According to their results the residual stresses are on average 67% of the yield strength in the corners, 43% of the yield strength in the edge stiffened elements and 71% of the yield strength in the stiffened elements.

### **1.2.2. Geometric Imperfections**

Geometric imperfection is defined as the deviation of member from perfect geometry. Geometric imperfections include bowing, warping, twisting and local deviations such as dents and undulations in plate. These imperfections are usually grouped into two types. As indicated in Figure 4, in type 1 the geometric imperfections are defined as the maximum deflection of a stiffened element whereas in type 2 they are defined as the maximum deviation of a stiffened lip or an unstiffened flange [10].



**Figure 4.** Definition of geometric imperfection types [10]

Width to thickness ratios ( $w/t$ ) of less than 200 and 100 are suitable for type 1 and type 2 imperfections, respectively. The magnitude of type 1 imperfection is determined based on an exponential curve fit as given in Equation 1. For type 2 imperfections the maximum deviation from initial shape is determined as approximately equal to the thickness of the section (Equation 2). In these expressions  $d_1$ ,  $d_2$  and  $t$  are in mm unit.

$$d_1 \approx 6te^{-2t} \quad (1)$$

$$d_2 \approx t \quad (2)$$

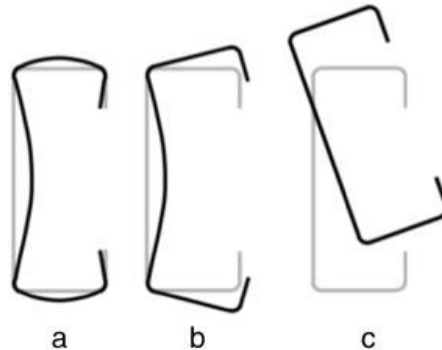
Geometric imperfections are crucial for the behavior of CFS members as they are usually vulnerable to cross-sectional instability. Dawson and Walker [11] studied the effects of different geometric imperfection parameters on simply-supported plates as a representative for stiffened CFS elements. Dat and Peköz [12] investigated the effect of imperfections and the eccentricity on the flexural behavior of CFS columns. Mulligan and Peköz [13] focused on the influence of local buckling on the structural behavior of CFS members.

Although little information is available in the literature on the imperfection variation along the length of the member, the maximum imperfection values are available. It has been proved that the geometric imperfection is closely related to the lowest eigenmode. Mulligan and Peköz [13] explained this behavior as the interaction of the local and overall buckling that leads to an imperfection sensitivity. It is proved that

the part of the additional deflection proportional to the first buckling mode, is much more significant with respect to the other parts when the first buckling load is reached [12].

### 1.3. Design Methods for Thin-Walled Members

As mentioned before the drawback of thin-walled elements is that they are very prone to local buckling and cross-sectional distortions. However, these complications can provide post-buckling strength that may result in a strength increase. As a result of these complications the design method of CFS differs from conventional steel design [14]. The ultimate load capacity of the member is usually different than the elastic critical load calculated due to physical non-linearity such as plasticity effects, geometrical and material imperfections, and the post-buckling strength reserve. The plasticity effect is tied to the material behavior, whereas the imperfection-sensitivity and the post-buckling strength are associated with the nature of buckling mode [15].



**Figure 5.** Buckling modes of a lipped channel section: (a) local buckling, (b) distortional buckling, (c) global buckling

The three buckling modes shown in Figure 5 are usually encountered in CFS members. Local buckling is defined as the mode that only involved plate buckling of the web of the flanges while the intersecting and adjoining lines of the section remain undistorted. In other words, the plate edges are elastically restrained. The distortional

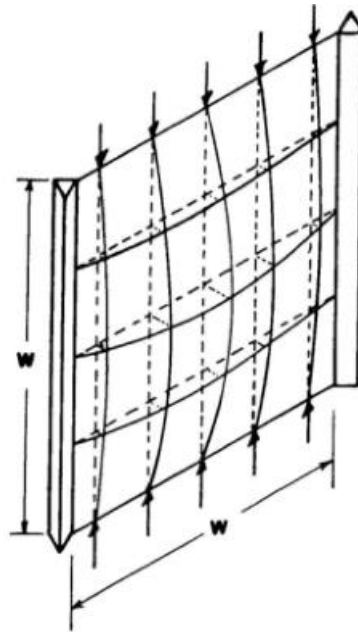
buckling mode is classified as the mode involving change in cross-sectional shape excluding local buckling. It is associated with the presence of stiffeners. While the presence of edge stiffeners improves the performance of the section against local buckling, it leads to distortional buckling which is another type of instability. The global or flexural-torsional buckling is defined as the mode in which the cross-section remains unchanged while bending and twisting is observed.

Currently the two simplified methods that are commonly used for the design of CFS members are Effective Width Method and Direct Strength Method.

### **1.3.1. Effective Width Method**

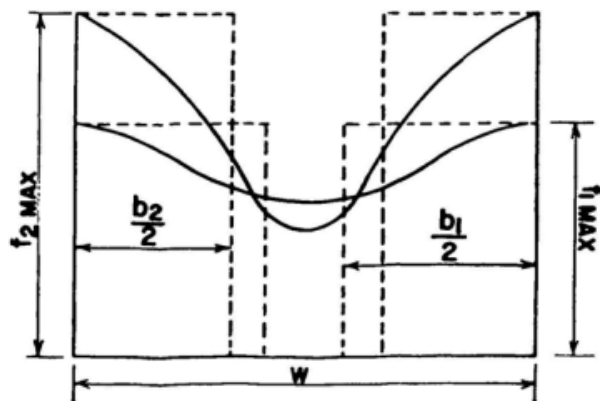
Effective Width Method (EWM) was proposed by Von Karman and modified for CFS by Winter [16]. The main idea of the EWM is that the local plate buckling results in some parts of the plates forming the entire CFS cross section becoming “ineffective” in resisting the load effects. In order to include this reduction in design, the gross area of the section is decreased to an effective area.

The method is based on the idea of the plate behavior where an axial load is applied to the plate as shown in Figure 6. The grid structure consists of longitudinal and transverse bars that represent the actual material of the plate. As the load is increased the longitudinal bars show buckling behavior and the transverse bars act as a restraint to the deflection by preventing the collapse of the longitudinal bars. The transverse bars correspond to the membrane stresses and they become effective as soon as the applied load causes buckling in the longitudinal bars. As a result, the bars close to the middle of the plate deflect most and lose their participation in any further load increase. Therefore, a total collapse is only observed when the bars close to the supports yield. This phenomenon is named as the post-buckling strength [17].



**Figure 6.** Post-buckling strength model [17]

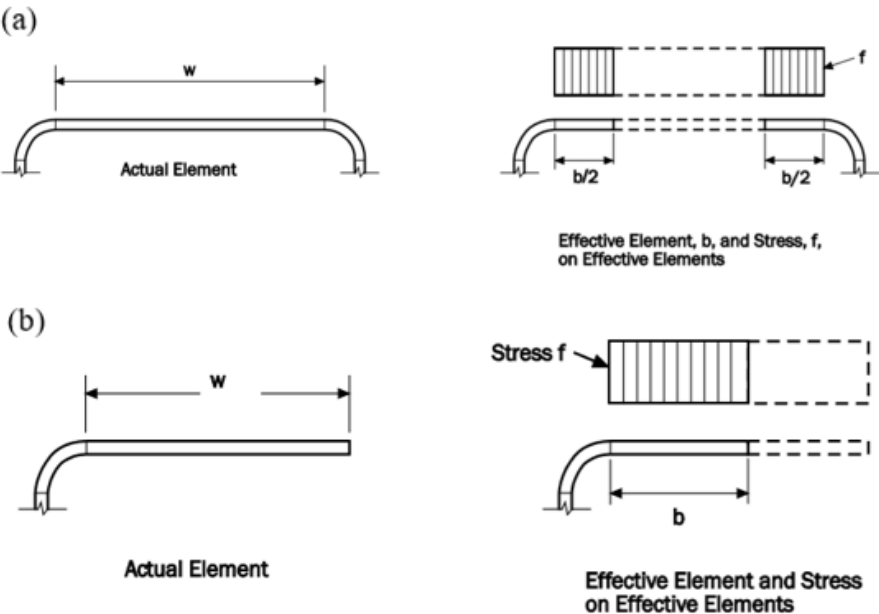
The resulting stress distribution on the plate is shown in Figure 7. As the load increases the stress distribution within the cross section becomes less uniform. The plate finally fails when the yield strength of the material is reached near the supports and no further redistribution of the load is possible.



**Figure 7.** Stress distribution in stiffened compression elements

In order to apply this phenomenon to the design the EWM was introduced and has been in use since 1946 [14]. Instead of considering the non-uniformity of the stress, the EWM assumes that the load is carried by a fictitious width. The value of these fictitious widths is calculated so that the area under the non-uniform stress distribution is equal to the rectangular areas that are formed by assuming a constant stress acting on plate pieces. The equations for the calculation of this width is presented in the AISI Specification [14] for stiffened and unstiffened elements and for uniform and gradient loading types.

The stress distributions for uniformly loaded stiffened and unstiffened elements are shown in Figure 8. Once the effective widths of the plates are determined according to loading and stiffening type, the effective area is calculated for the section. The further calculations are completed for the section capacity for local and global buckling capacities.

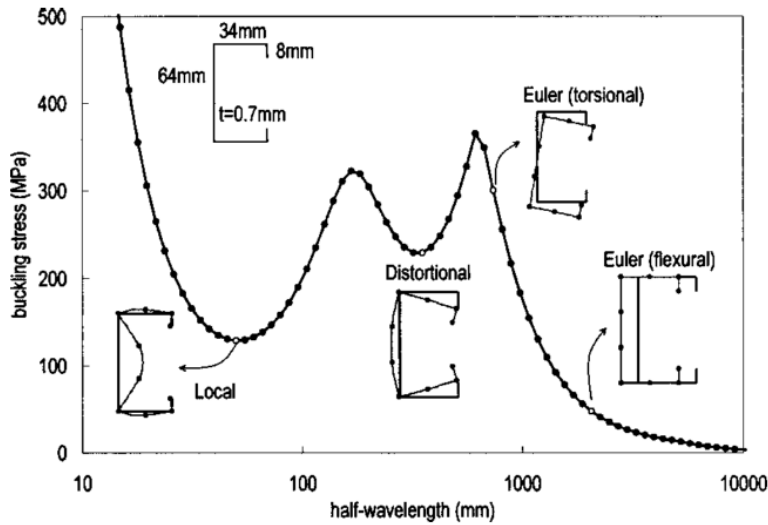


**Figure 8.** Stiffened (a) and Unstiffened (b) element subjected to uniform compression [14]

The EWM simulates the local-global interaction where the reduced section properties influence global buckling. Although this method has proved to be quite successful in predicting strength and idealizing the behavior, it has theoretical and practical drawbacks. Researchers [18,19] have reported that the EWM is not quite successful in predicting distortional buckling failure and that it ignores the inter-element equilibrium and compatibility and focuses on plate behavior. In other words, the effective area is separately calculated for each plate and the interaction between the plates forming the section is ignored. In terms of practicality, the required number of iterations to calculate the value of effective width and the complications due to the stiffeners added to the section for optimization are considered as deficiency.

### **1.3.2. Direct Strength Method**

Direct Strength Method (DSM) has been developed by Schafer and Peköz [20] to overcome the complexity and the inefficiency of the Effective Width Method. This method was included in the AISI Specifications in 2004 [14]. The DSM considers the gross cross section instead of individual plates for the elastic buckling solutions. This has especially become a need when the sections became more complex with edge and intermediate stiffeners introduced. The method assumes that by using the elastic buckling stress of the entire section with a suitable strength design curve for local instability, it is possible to predict the critical buckling loads [16]. Once the elastic buckling solutions are available, which is quite usual nowadays using the recommended softwares, the calculations are simple and the gross-sectional properties are used. Finite Strip Method is usually the preferred method to determine the elastic buckling capacity of CFS sections. The FSM is a numerical method that discretizes the section into longitudinal strips. By considering the support conditions, the finite strip buckling analysis determines the signature curve that provides local, distortional and global buckling loads or moments depending on the input loading. A sample signature curve for a lipped channel section is presented in Figure 9. Each buckling mode is associated with a particular deformed shape and a half-wavelength value. The determination of the buckling modes in terms of stress and half-wavelength provides a complete signature curve.



**Figure 9.** Signature curve of a lipped channel section [21]

#### 1.4. CFS Trusses

For fabrication of CFS trusses generally C, U and hat shaped sections are preferred. One of the most commonly used C shaped sections is lipped C section with intermediate web stiffener where lips act as stiffeners for the flange elements and the web is stiffened by additional stiffeners. Stiffeners provide additional post-buckling strength for slender elements by stress redistribution. The literature review yielded little information on the studies of CFS truss systems. The available research has generally focused on roof trusses.

Dawe and Wood [22] have tested CFS roof trusses at a small scale and investigated the behavior of heel connection. The main failure mode is observed to be the local buckling of the top chord which has been followed by the distortion of the heel plates due to inadequate stiffening of the plates. They also concluded that post-buckling ductility is exhibited by the specimens that have failed due to local buckling of the top chord. Dawe et al. [23] have further investigated the roof trusses through testing of full scale specimens. The most significant increase in the capacity is observed when the top chord and the heel connection is reinforced with shallow members. The loading applied is altered and it is determined that the ultimate capacity of the truss



specimen is reduced by 21% when half-span point loading is used instead of full-span point loading.

### **1.5. Concrete CFS Composite Systems**

Composite structures of hot-rolled steel and concrete have been widely used due to the need for cost-effective composite structural components. By combining the benefits of the two construction material, the composite systems have been considered as an efficient way to achieve economy. In steel-concrete composite members, steel elements are usually responsible for resisting tensile forces while compressive forces are resisted by concrete. The use of cold-formed steel with concrete provides a system that makes use of the advantages of both materials while avoiding the weaknesses that they carry by nature. Extensive research has been carried out on the behavior of hot-rolled steel and concrete composite members. The establishment of the bond between the two elements is essential in order to achieve the expected strength and flexibility. As bonding elements are introduced to the system, concrete and steel are prevented from acting individually, and as a result, the stiffness and the load carrying capacity of the system is increased. The overall enhancement of the capacity of the system is directly related to the effectiveness of the force transfer between the CFS and concrete. When the slip between the steel and concrete is prevented and they are forced to act together, the capacity of the resulting composite system is expected to be higher. Although the general principles of the design of composite beams are applied for both hot-rolled and CFS sections, different shear connectors are used in two systems. Welding of shear studs is not suitable while establishing the shear connection between the concrete and the CFS section due to the small thickness values [24]. Therefore, other types of shear connectors have been experimentally tested by numerous researchers.

Use of composite action in CFS-concrete systems has been investigated by several researchers. Hanaor [24], Hsu et al. [25] and Youns et al. [26] have studied the CFS composite beams with concrete slab. Hanaor [24] investigated the connection of the composite beams according to two different assembling types. In the first type

concrete slab is poured on CFS beams with the help of a profiled deck. The composite action between the profiled deck and the concrete slab is not mandatory. In the second type a thin concrete layer is directly poured over the CFS section. After the positioning of CFS sections side by side, a topping layer of concrete is cast. However, in either of these methods the CFS section flange is not embedded in the concrete slab.

Lakkavalli and Liu [27] have performed push-out tests and large scale beam tests on composite sections where the flange of the CFS is embedded in the concrete. They tested three types of shear connectors, which were pre-drilled holes, pre-fabricated bent-up tabs and self-drilled screws. The effect of the shear connector type and the connector spacing are discussed for varying section thickness. Among the three methods investigated self-drilled screws yielded in the least improvement with an increase of only 13% in ultimate capacity. As the spacing of the shear connectors decrease, the capacity of the section does not necessarily increase. This finding is attributed to the effect of overlapping stress fields. Finally, the authors concluded that as the thickness of the CFS increases a better composite action is achieved.

Ipe et al. [28] and Haris et al. [29] tested concrete infilled composite CFS sections. Ipe et al. [28] have tested the flexural behavior of concrete filled CFS channel sections with various shear connectors in both positions where the web of the section is facing up and down. When the load-deflection behavior of these specimens is considered, the largest capacity increase is observed for the web facing up specimens with bolt type and lip bar type shear connectors. The capacity of the concrete infilled sections was observed to be 32% higher than the bare CFS section. With the inclusion of the shear connectors the observed capacity is reported to increase by up to 120%.

Although there are previous research efforts conducted to identify the composite behavior none of these studies focused on CFS truss systems where the top chord is fully embedded inside the concrete. They mainly focused on partly submerged sections with flanges embedded in concrete slab or fully filled sections without trusses. CFS trusses are already used as floor beam in the industry, however the slab is attached through corrugated steel sheets with no direct contact between the CFS

section and the concrete slab. The CFS truss experiments previously performed have shown that the top chord buckling is the main failure mode due to the relatively low buckling capacity of the thin walled sections. Therefore, this study was initiated in order to study the effectiveness of concrete infill in controlling the local instability of top chord members observed in CFS floor trusses.

### **1.6. Aim and Objective**

The main focus of this thesis is to investigate the composite behavior of steel-concrete composite CFS floor trusses when subjected to flexural loading. In order to control the local instability of the top chord concrete is introduced to the system. With the shear connectors, it is intended to increase the buckling capacity of the top chord and increase the load carrying capacity of the truss system. The aim is to quantify the enhancement that concrete provides in the compression capacity of the top chord of the truss. By providing the concrete infill in compression chord member the failure mode of the truss is expected to change from compression chord buckling to tension chord yielding. Such change in the failure mode would result in an increase the load carrying capacity of the floor system.

### **1.7. Thesis Outline**

This thesis is composed of five chapters, through which the experimental, numerical and analytical studies and the results are explained in detail. Introduction and literature review have been presented in this chapter. The theoretical background of the CFS sections and design methods are also briefly reviewed in this chapter.

Chapter 2 covers the experimental studies and results in detail. In this chapter the experimental procedure, measuring devices and the material properties are explained. The obtained results are presented and the effect of test parameters are discussed.

The focus of Chapter 3 is the numerical model. The assumptions made during the construction of the model and the material models used are presented in this chapter.

The results obtained for each specimen and their comparison with the experimental results have been provided.

Chapter 4 explains the analytical studies. The strain distribution as well as the yield and ultimate loads are predicted and these results have also been verified with the experimentally obtained results.

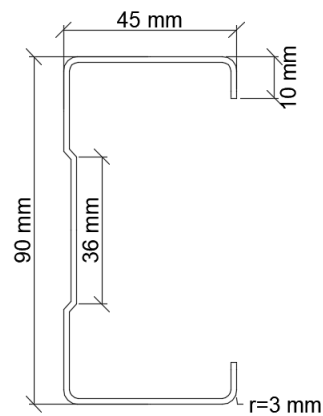
Finally, Chapter 5 covers the conclusions reached during this study and suggests further research topics.

## CHAPTER 2

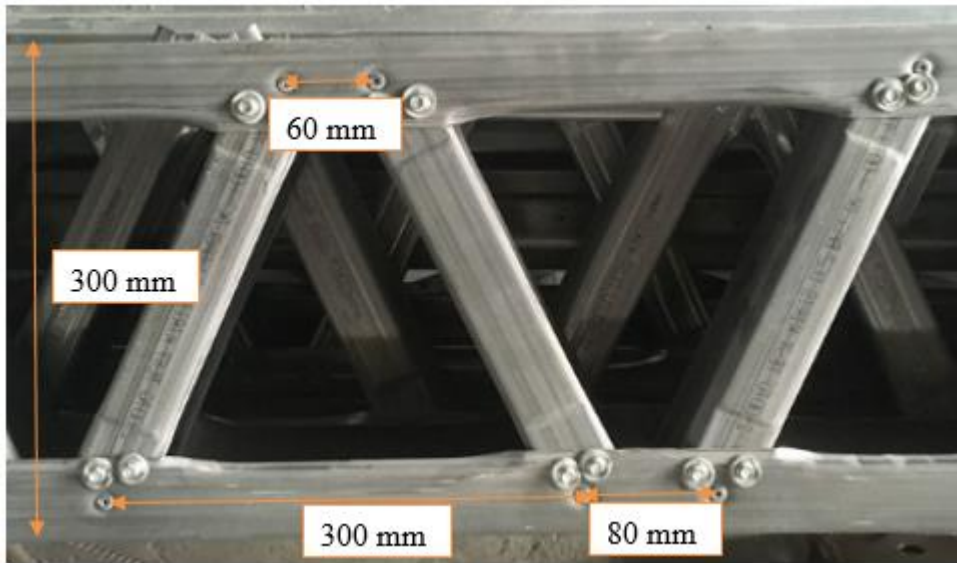
### EXPERIMENTAL STUDY

#### 2.1. Truss Specimens

Load tests were conducted on 6 m long 300 mm deep CFS truss specimens. The trusses were fabricated using 1.6 mm thick CFS lipped channel sections with 90 mm overall depth and 45 mm flange width. Geometric details of the CFS section and the truss configuration are provided in Figures 10 and 11, respectively.

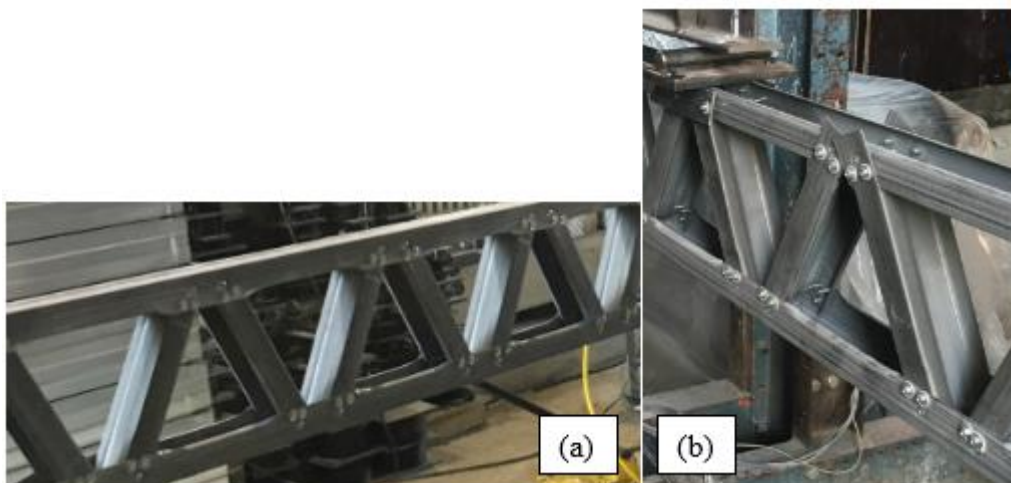


**Figure 10.** CFS section dimensions



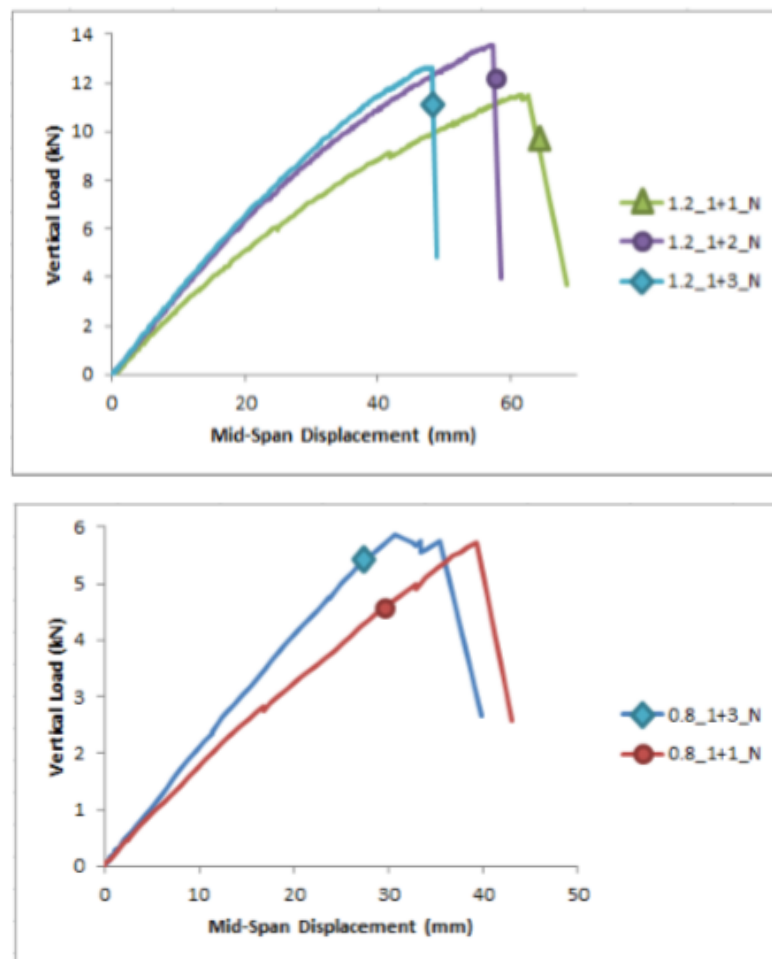
**Figure 11.** Geometric details of the truss configuration

Truss specimens with the two top chord configurations shown in Figure 12 were manufactured. As seen, the top chord member in truss specimens was facing either down (Figure 12a) or up (Figure 12b). Since the web of the channel section defines the position of the chord member, these specimens were named as WB (web at bottom) and WT (web at top).



**Figure 12.** Specimen WT\_Control (a) and WB\_Control (b)

The diagonal and the chord members in truss specimens were connected using two rivets and four screws. The previous studies done at the Middle East Technical University [30] with the same truss configuration using 1.2 and 0.8 mm thick sections have shown that increasing the number of the screws usually results in improved overall response of truss specimens. Overall load versus midspan deflection response of 1.2 and 0.8mm thick truss specimens tested by Dizdar [30] are shown in Figure 13. Where the specimen names represent the connection configuration (section thickness\_number of rivets + number of screws). The truss stiffness seems to saturate when a rivet and two additional screws were used to connect each flange of the diagonal member to the chord. Based on this observation each diagonal chord connection in the current study was formed by two rivets and four additional screws.



**Figure 13.** The effect of number of connection screws on truss response [30]

The blind rivets and self-tapping screws used at diagonal-to-chord connections in truss specimens were of 4.8 and 5.5 mm in diameter, respectively. A picture of these fasteners is shown in Figure 14.



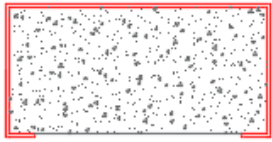
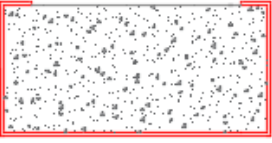
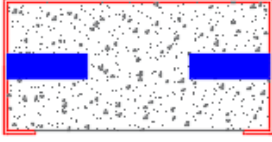
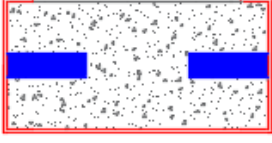



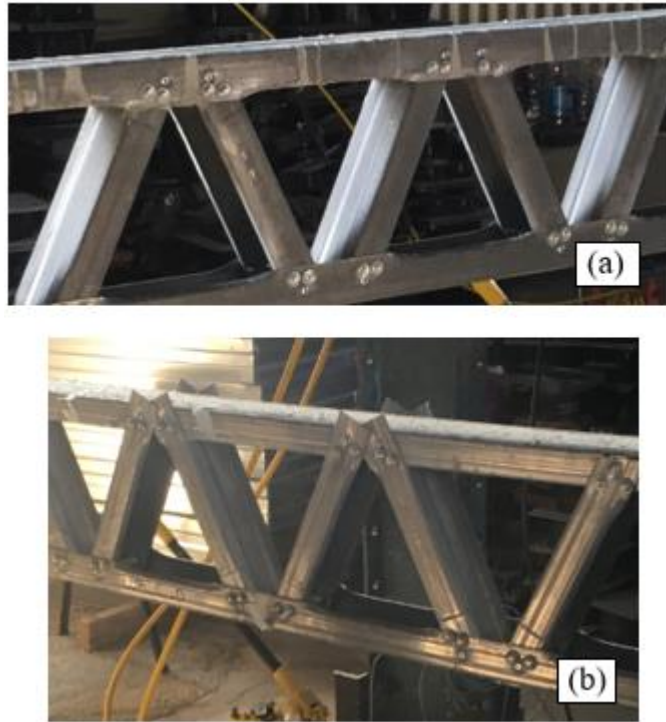
**Figure 14.** Screw and rivet used in truss specimens

The top chord condition in all seven specimens is given in Table 1. In specimens WT\_C and WB\_C, the lipped channel section forming the truss top chord was filled with concrete as shown in Figure 15. As mentioned earlier, the concrete filling provided inside the top chord CFS section was aimed to delay or eliminate the top chord local/distortional buckling observed in conventional CFS floor trusses. Presence of a composite action between the top chord CFS section and the concrete filling would also improve the truss strength and stiffness.



**Table 1.** Truss top chord configurations used in specimens

<b>Specimen</b>	<b>Top Chord Condition</b>	<b>Concrete Strength (MPa)</b>
<b>WT_Control</b>		
<b>WB_Control</b>		
<b>WT_C</b>		24.6
<b>WB_C</b>		24.6
<b>WT_C_100</b>		24.6
<b>WB_C_100</b>		32.9
<b>WB_Slab</b>		32.9



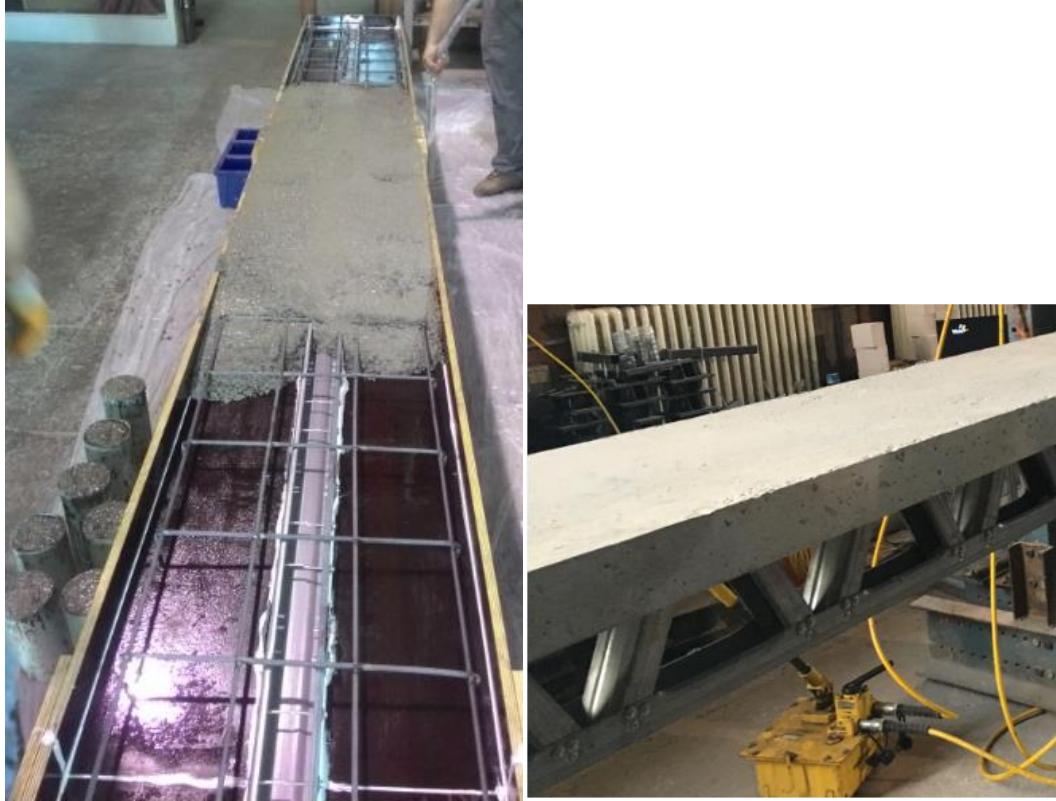
**Figure 15.** Specimen WT\_C (a) and WB\_C (b)

Although the screws and rivets used for connecting the diagonal and chord members provide some horizontal shear force transfer between the concrete and the top chord CFS section; additional screws with 5.5 mm diameter and 50 mm thickness were placed along the top chord at 100 mm spacing in specimens WT\_C\_100 and WB\_C\_100. This was done to increase the horizontal shear force transfer and to improve the composite action between the top chord CFS section and concrete filling.

A single 10 mm diameter reinforcing steel bar was placed inside the top chord CFS section along the entire length of the concrete infilled specimens prior to placement of the concrete filling in order to prevent concrete cracking that may have developed due to temperature and shrinkage effects.

In specimen WB\_Slab, a reinforced concrete slab with 80×600 mm dimensions was placed on top of the top chord CFS section as shown in Figure 16. The reinforcement used inside the slab included four 10 mm diameter reinforcing steel bars along the length and 10 mm diameter reinforcing steel bars placed at 250 mm spacing in the

transverse direction. The concrete was poured at the laboratory by assembling a formwork that carried the wet concrete load until it was hardened (Figure 16).

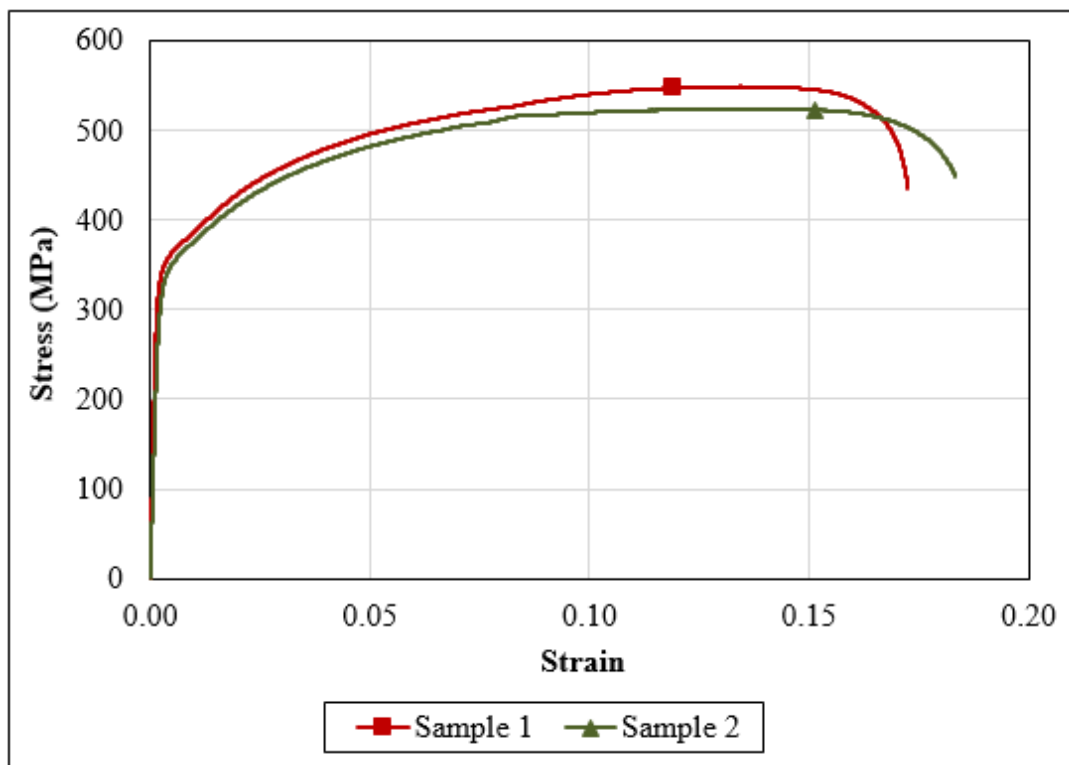


**Figure 16.** Specimen WB\_Slab

Two coupon samples were extracted from the CFS members for the determination of the yield and ultimate strengths. Tensile testing was conducted on coupon samples as shown in Figure 17. The yield strength was determined using the 0.2% offset method as 355 MPa and 341 MPa. The ultimate strength was determined as 550 MPa and 525 MPa. In numerical studies explained in the subsequent sections, average yield and ultimate strengths based on the test results from these two coupon samples were used. The stress-strain response of coupon samples are provided in Figure 18.



**Figure 17.** Tested coupon samples

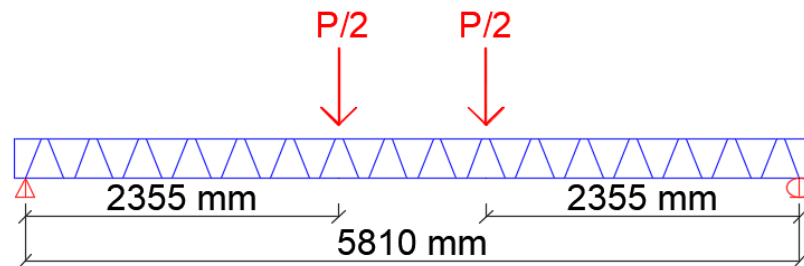


**Figure 18.** Stress-strain behavior obtained from coupon samples

Two mixes of concrete with a target 28-day strength of 30 MPa were used for the specimens that included a concrete filled top chord or a concrete slab. The measured 28-day concrete compressive strength values are presented in Table 1. These values represent the average strengths based on two 15 ×30 cm cylindrical samples. The fact that the first mix of concrete has significantly smaller measured strength than the target value indicates a possible discrepancy between the assumed and actual water content of the material used to prepare the mix.

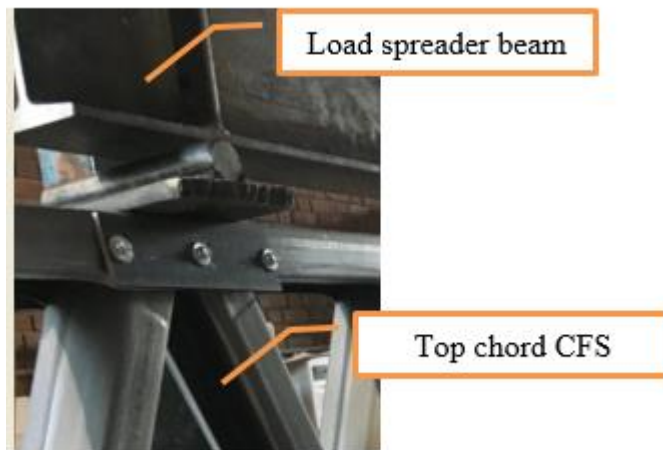
## 2.2. Experimental Setup

The trusses were tested as simply supported elements with a clear span length of 5810 mm. The load was applied to the truss through a steel beam that distributes the total load into two equal forces applied on the trusses. The testing was conducted with two equal loads with the same distance from the midspan so that a constant moment region of 1100 mm occurred in the middle of the test span (Figure 19).



**Figure 19.** Schematics of experimental setup

The loading was applied by a hydraulic jack that had the load spreader beam attached at the end. The load was transferred to the truss top chord through steel cylinders placed over steel plates so that the load was distributed more uniformly. At loading points, additional plates were attached to the opposite sides of the top chord member in order to prevent local deformations at these locations (Figure 20).

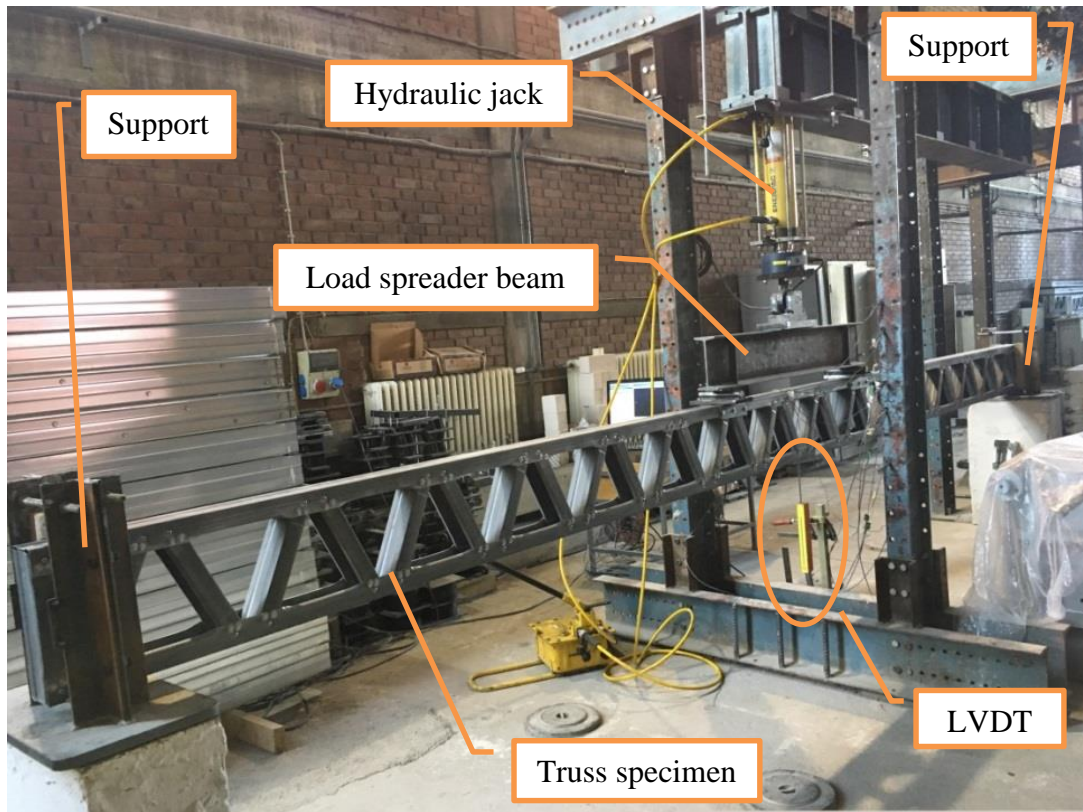


**Figure 20.** Detail used at loading points

Vertical restraint at supports was provided by steel cylinders placed at the truss ends. One of these cylinders was also restrained in the horizontal direction so that a pin support and a roller support were formed in the experimental setup. The lateral support at truss ends was provided by placing wooden blocks between the two steel channel section and the specimen. A teflon sheet was placed between these wooden blocks and the specimen in order to minimize the friction.

The experimental setup used for the tests is presented in Figure 21. A 150 mm Linear Variable Displacement Transducer (LVDT) was used to record the truss midspan deflection. Strain gages were also attached to the top and bottom chord members in some of the truss specimens (Figure 22). The details of strain recordings from these gages are presented in later sections. These strain gages were usually attached to the chord members at midspan section in order to monitor the variation of strains under loading at several locations within the midspan section. In some specimens, additional gages were used at cross sections other than the midspan section.





**Figure 21.** Experimental setup

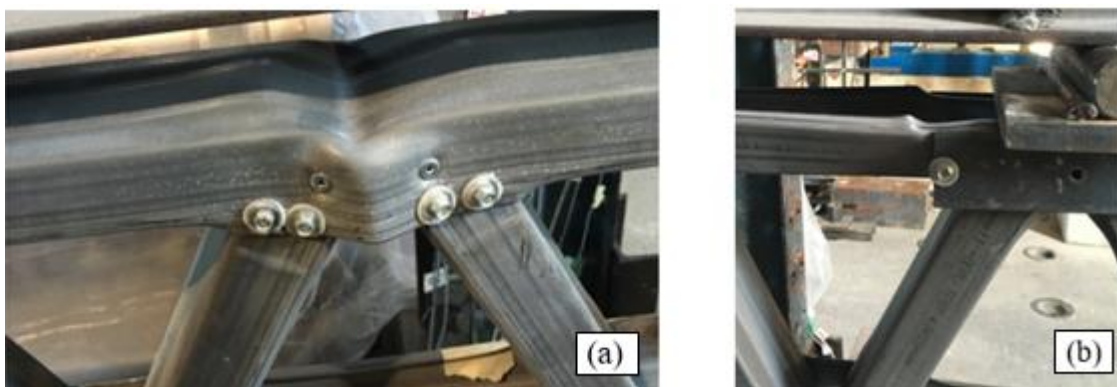


**Figure 22.** Strain gages attached on CFS member

## 2.3. Load Test Results

### 2.3.1. Observed Failure Modes

Among all seven truss specimens, the two specimens tested with no concrete filling or concrete slab (specimens WT\_Control and WB\_Control) experienced local buckling at the top chord. Figure 23 shows the buckled compression chord in these specimens. Similar type of compression chord local/distortional buckling was observed in truss specimens previously tested by Dizdar [ 30].



**Figure 23.** Failure shape: (a) WT\_Control, (b) WB\_Control

Presence of concrete filling inside compression chord CFS section in specimens WT\_C, WB\_C, WT\_C\_100 and WB\_C\_100 and the presence of concrete slab in specimen WB\_Slab prevented the formation of local/distortional buckling. In these specimens, the failure mode was tensile yielding of bottom chord CFS section. The bottom chord yielding is evident with the measured cross-sectional strains, as well as the highly ductile load-deflection response of specimens. Deformed shape of the specimen WB\_Slab at the end of the test is shown in Figure 24. Concrete cracking started at the bottom surface of the slab and extended through the sides in specimen WB\_Slab. Crack pattern observed on one side of the concrete slab in this specimen is shown in Figure 25.





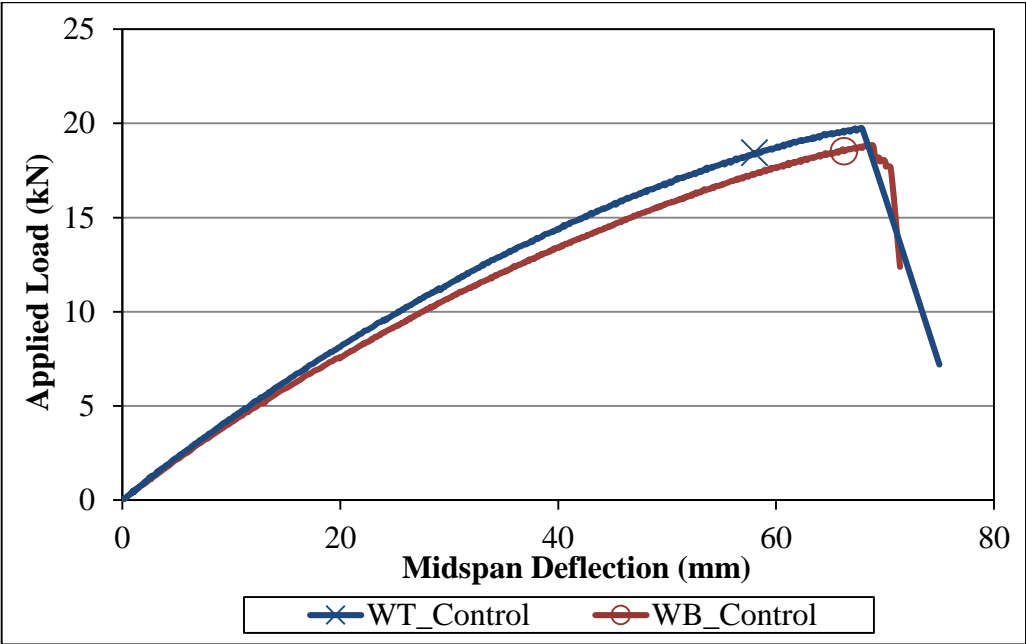
**Figure 24.** Deformed shape of specimen WB\_Slab



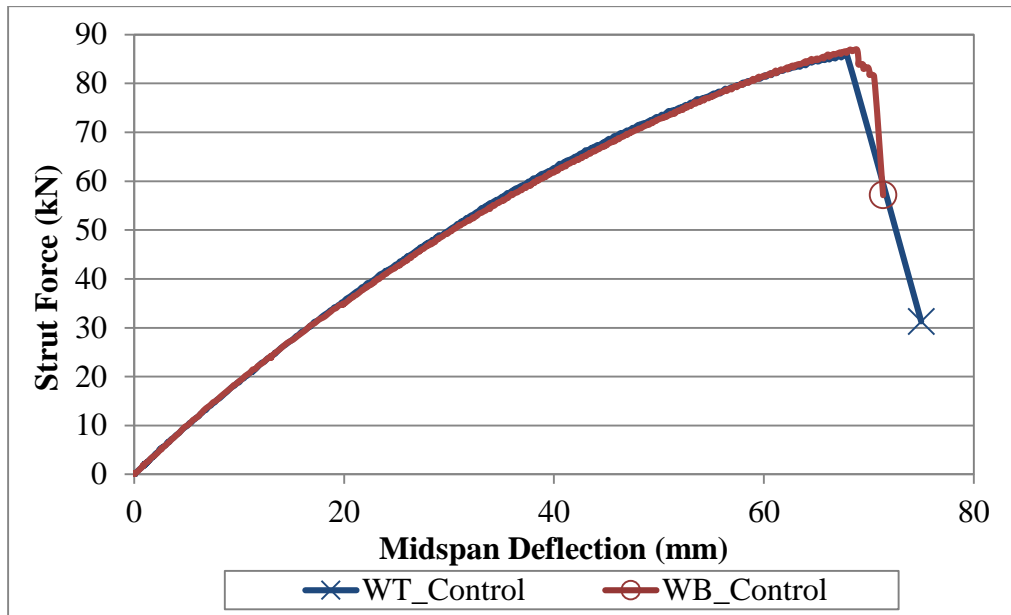
**Figure 25.** Concrete cracking in specimen WB\_Slab

**2.3.2. Effect of Top Chord Orientation**

The truss specimens without concrete (WT\_Control and WB\_Control) were loaded up to the failure. As mentioned earlier, these specimens failed due to local/distortional buckling in compression chord CFS member. While specimen WT\_Control failed at 19.71 kN, specimen WB\_Control failed when the applied load reached 18.83 kN. The measured load versus midspan deflection curves given in Figure 26 show that the stiffness and the load capacity of these specimens differ slightly, even though both curves have similar overall shapes. The applied vertical load was converted into the corresponding top chord force values by making use of the shear span and truss depth. Variation of top chord force with the midspan deflection for these two specimens is plotted together in Figure 27. Both orientations of the compression chord resulted in identical strut force versus midspan deflection response. Based on this observation, it can be concluded that the difference in the stiffness values of the two specimens is related to the moment of inertia of the section. When the compression chord is facing up (web-bottom orientation) the centroid of the channel section is located at a lower height; therefore, the inertia of the whole section is reduced.



**Figure 26.** Effect of top chord orientation (load-midspan deflection)



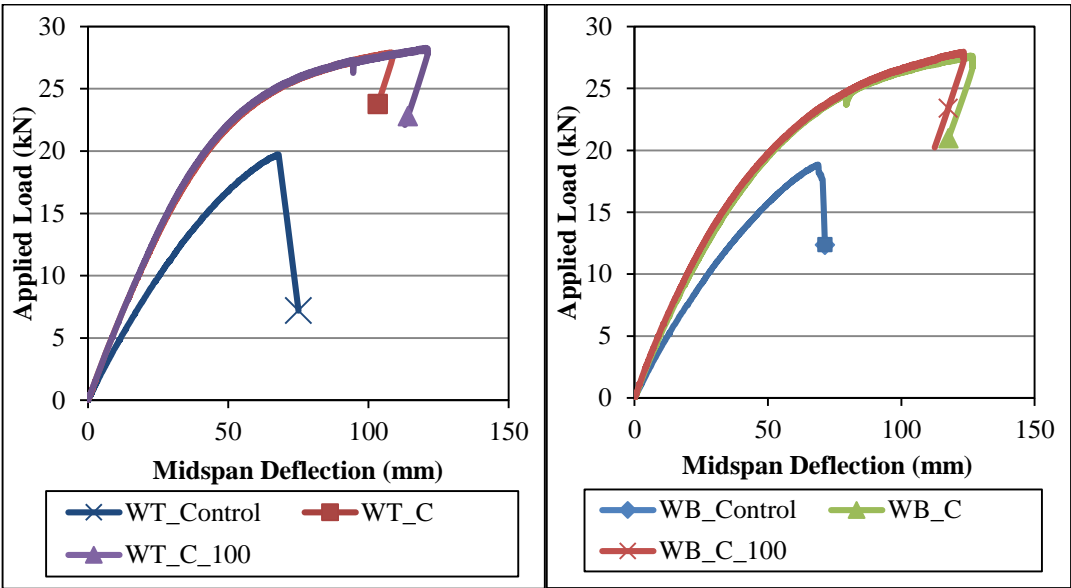
**Figure 27.** Effect of top chord orientation (strut force-midspan deflection)

The top chord in specimen WB\_Control was subjected to local/distortional buckling adjacent to one of the loading points. The additional plates attached to the sides of the top chord member at the loading points were not sufficient to prevent buckling at that region. The reason for this could be related with the screw connection between the side plates and the top chord. These plates were not directly in contact with the flanges of the top chord due to heads of the screws connecting the compression chord to diagonal members. As a result, the screws used to attach the side plates to the compression chord flanges may have caused additional distortion in this region.

### 2.3.3. Effect of Concrete Infill

The effect of concrete infill is clearly observed in the load versus midspan deflection curves shown in Figure 28. Truss specimens with concrete infilled compression chord exhibited higher load capacity and stiffness compared to the companion trusses tested with no concrete infill. While the web at top specimen configuration (WT) experienced a 41% load capacity increase; for the web at bottom configuration (WB) load capacity is increased by 47%. The larger capacity increase of specimen WB\_C

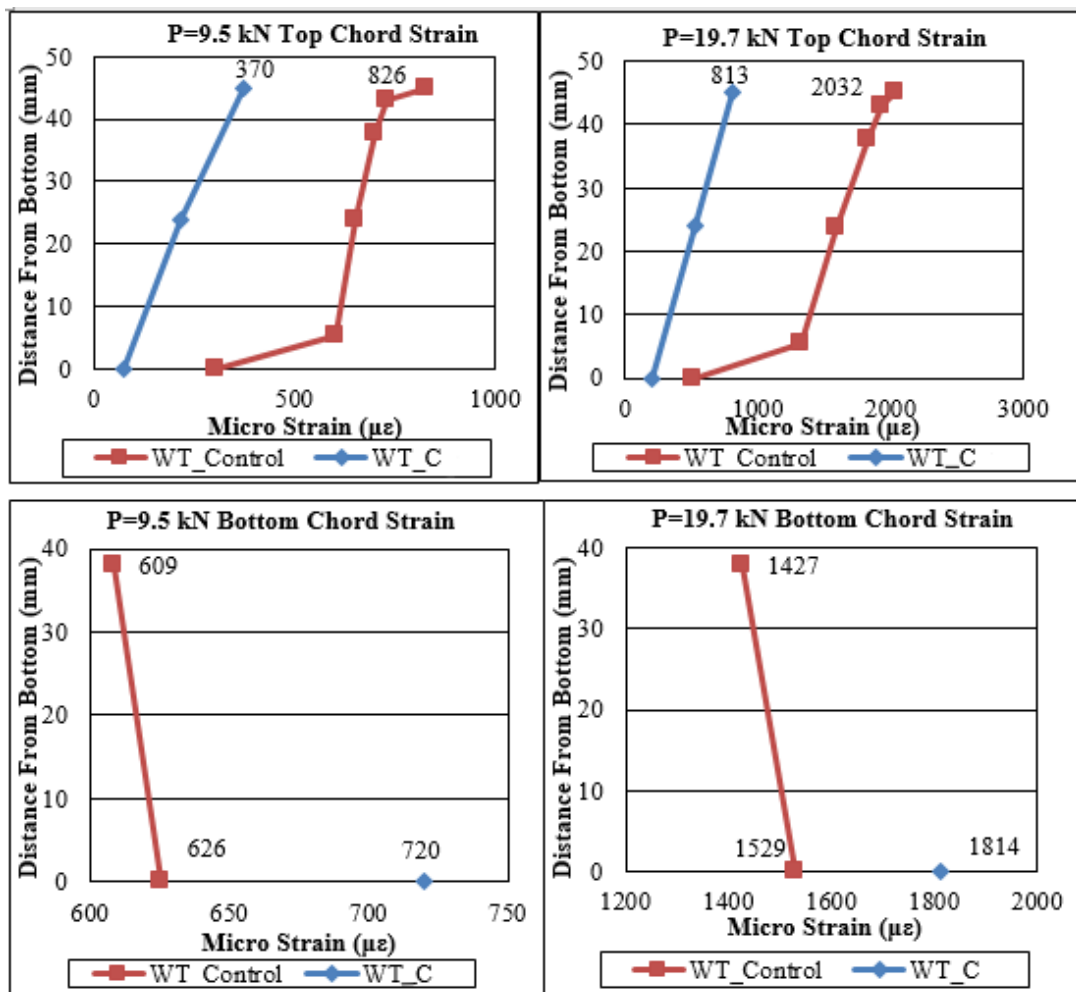
when compared to specimen WB\_Control can be explained by the buckling behavior of specimen WB\_Control mentioned in the previous section. Due to the side plates used at the loading points an additional distortion might have been introduced in the compression chord member. This caused a buckling failure in specimen WB\_Control before the expected capacity was reached. When the concrete infill was provided, buckling of the compression chord was prevented and the specimen was able to maintain the expected load capacity, resulting in a significant increase in load capacity.



**Figure 28.** Effect of concrete (Specimens WT\_C and WB\_C)

Strain profiles determined experimentally at the midspan cross section of plain truss and concrete infilled truss specimens are compared in Figure 29, for load levels of 9.5 kN and 19.7 kN. The 19.7 kN is the maximum load applied to specimen WT\_Control before the failure was observed, while 9.5 kN is selected as approximately the half of the maximum applied load. With the effect of infill, the top chord strain was reduced by up to 40%. One of the reasons for the reduction of truss compression chord strains is the addition of concrete infill inside compression chord member which increase the stiffness of the truss. Another reason is the shifting up of

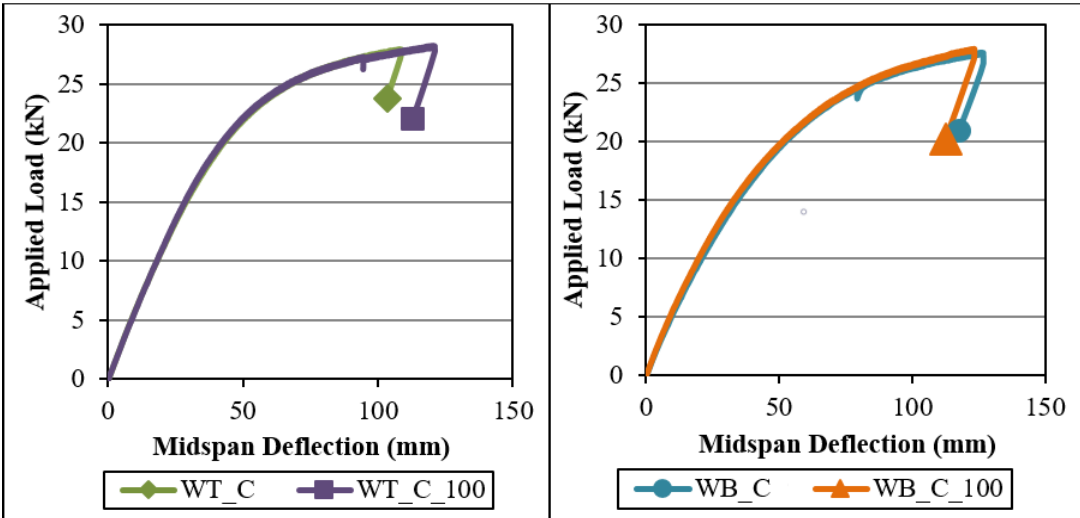
the neutral axis in the truss cross section. For the truss compression chord the effects due to these two factors is additive, i.e. they both caused a reduction in strains. For the truss tension chord, on the other hand, the effects are not additive, and the net result is an increase in tension chord strains. As expected an opposite effect is observed at the bottom chord. The bottom chord strain is increased by up to 19%. Another important observation is that as the top chord buckling was prevented, the bottom chord strains reached to yield strain value.



**Figure 29.** Effect of concrete infill on midspan section strains

**2.3.4. Effect of Shear Enhancements**

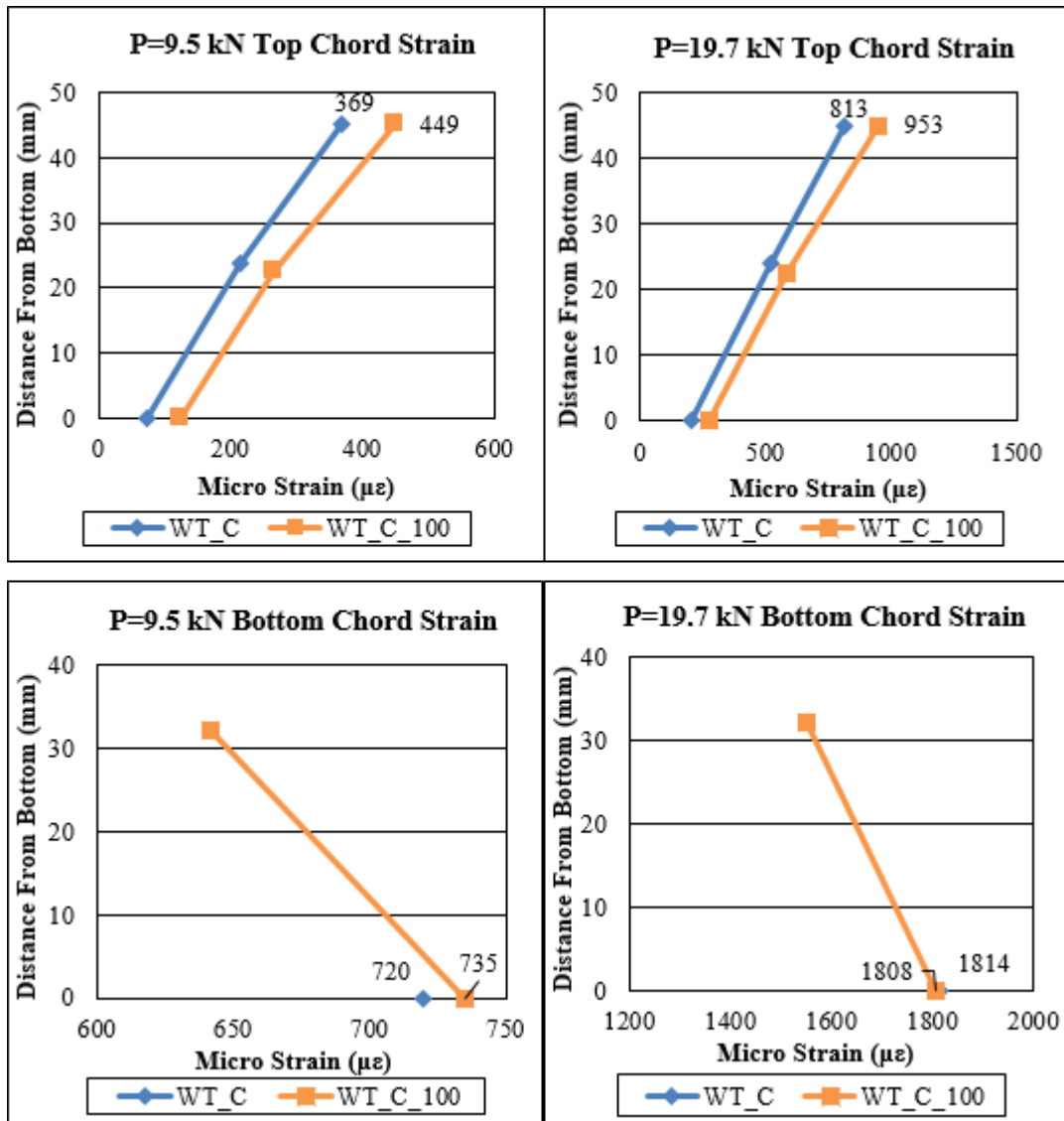
The shear enhancements were included in compression chord of truss specimens in the form of self-drilled screws provided at 100 mm spacing. The main idea of adding these enhancements was to improve the bond between concrete and the top chord of the member. Therefore, they were expected to reduce the relative slip between the CFS top chord member and concrete infill and as a result provide a uniform force transfer between the two materials. The effect of the shear enhancements can be seen in Figure 30.



**Figure 30.** Effect of shear enhancements

No slip was observed between the top chord CFS member and concrete infill during load testing of truss specimens tested both with and without shear enhancement. Therefore, although the shear enhancements provided a better bond connection between the concrete infill and CFS section, they did not have an effect on the overall load-deflection response of truss specimens. This implies that the connections included for the construction details are enough to establish a sufficient bond between the concrete infill and the top chord of CFS trusses.

The strain comparison of the shear enhanced and the companion specimens are plotted in Figure 31. The strain comparisons are provided for load values of 9.5 kN and 19.7 kN, where the load of 19.7 kN corresponds to the maximum load that the specimen WT\_Control resisted during the test. Although no specific difference is observed for the load-deflection curves, the strains show differences especially at the top chord member. The difference between the strain values of these specimens is 21% under the load of 9.5 kN and 17% when the load was 19.7 kN. At the bottom chord the effect of the shear enhancements are much less; 2 % under the load of 9.5 kN and less than 1% when the load was 19.7 kN. These strain differences determined for the bottom chord member can be considered to be within the variation in strain measurements. The difference in top chord strains between the cases of the shear enhanced and the companion trusses is related with the bonding effect of the concrete and the top chord steel. With the application of the shear enhancements, the bond between the concrete infill and the top chord gets stronger and a better force transfer between the two materials occurs.



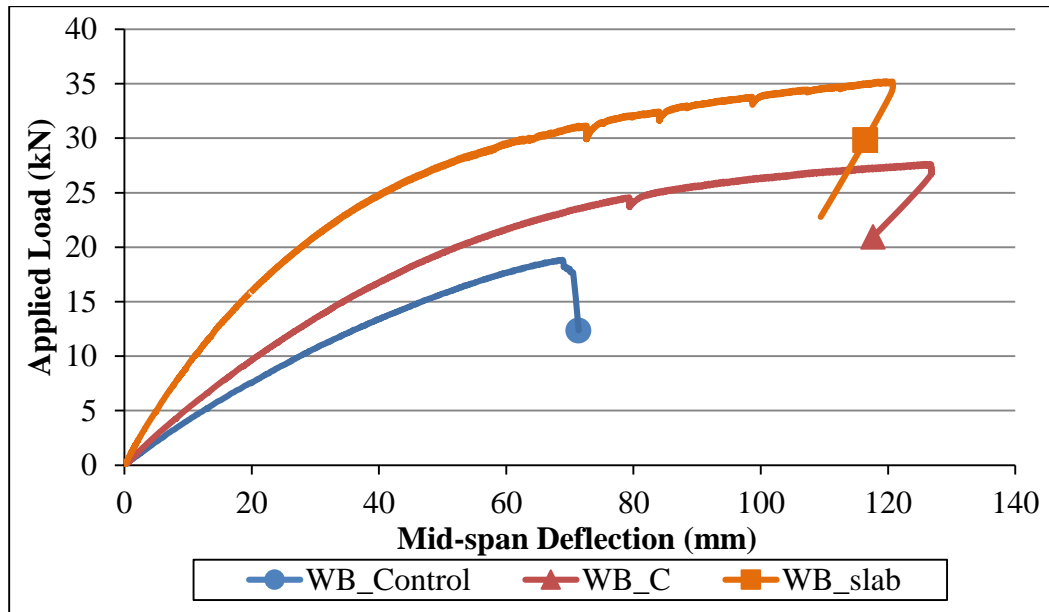
**Figure 31.** Effect of shear enhancements on midspan section strains

### 2.3.5. Effect of Concrete Slab

Results obtained from the specimen that includes a concrete slab placed over the CFS truss are compared to those obtained from the trusses with concrete infilled and bare CFS compression chord. A comparison of load-deflection responses is provided in Figure 32. With the addition of concrete slab, the moment of inertia of the truss section was increased and the neutral axis moved up within the section. As a result, the flexural response was improved with increased stiffness and load capacity. Presence of the slab increased the truss stiffness by approximately twice compared to

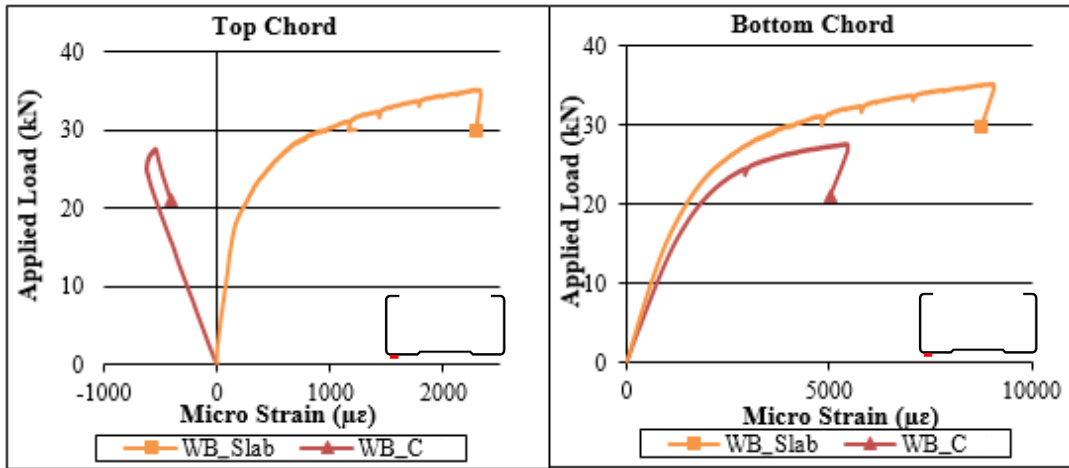


the specimen with concrete infilled top chord. There is also an increase of 27% in load capacity of the truss with the introduction of concrete slab. For both of these specimens the load capacity is controlled by yielding in tension chord CFS section.



**Figure 32.** Effect of the presence of concrete slab

The comparison of the strain gage recordings of specimen WB\_C and WB\_slab are presented in Figure 33. As can be seen, while the strain gage attached at the bottom of the top chord is under tension for the WB\_slab, the strain gage attached at the same location for the specimen WB\_C is initially under compression. This implies that the neutral axis of the specimen WB\_slab resides inside the top chord. For specimen WB\_Slab the bottom chord strain values reaches up to  $9260 \mu\epsilon$ , which is well beyond the yield strain value and is an indication of extensive yielding of the bottom chord member.



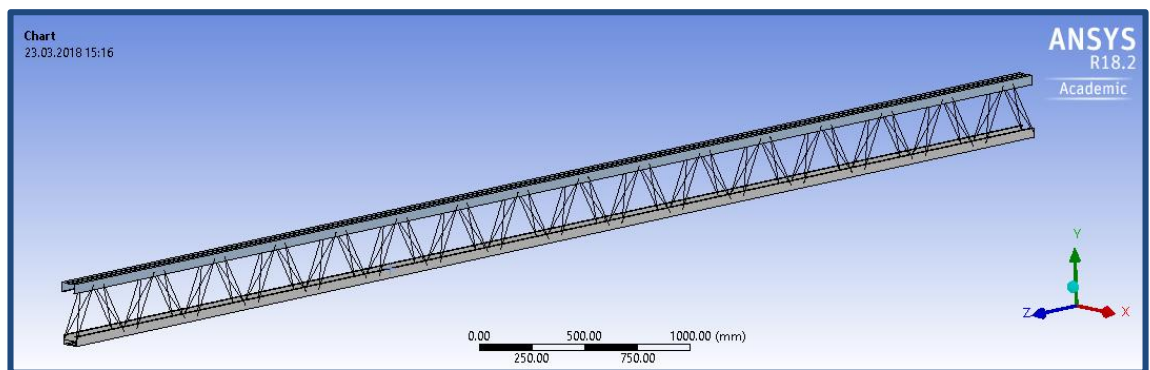
**Figure 33.** Effect of concrete slab on midspan section strains

## CHAPTER 3

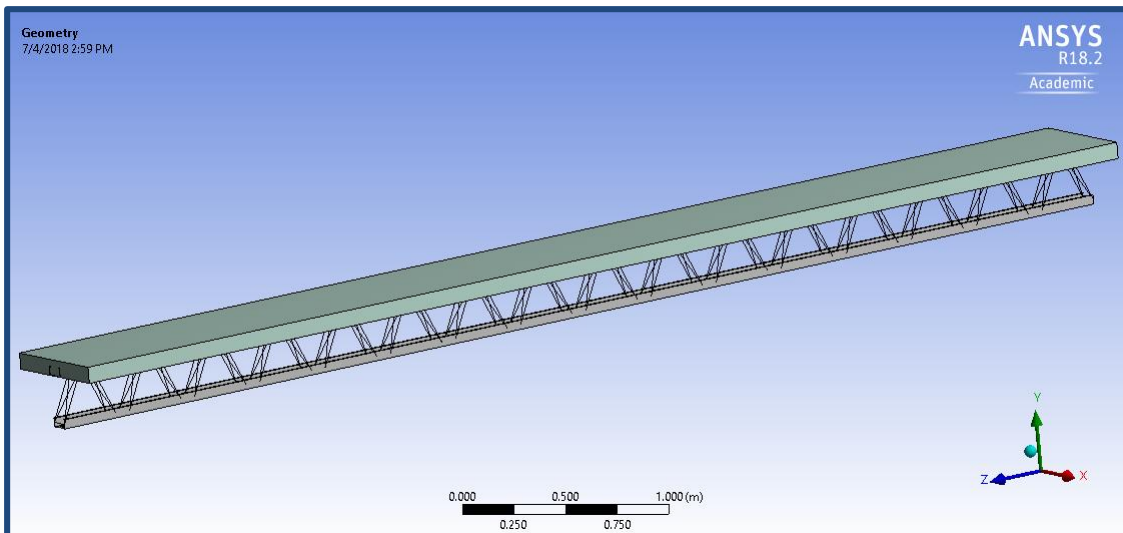
### FINITE ELEMENT MODELLING

#### 3.1. Description of Finite Element Model

The numerical model of test specimens was generated in ANSYS Workbench 18.2 [31]. The top and bottom chords were modelled continuously using linear shell elements (Shell 181). The diagonal elements were modelled using circular cross section beam elements (Beam 188). Cross-sectional area of these beam elements were determined based on axial stiffness of diagonal members in truss specimens. In order to include the effect of connection flexibility in the model, the area of the beam elements representing the truss diagonal members was adjusted to be 13% of the area of the CFS section forming the diagonal members [30]. The created FE model is presented in Figure 34 for the bare truss and in Figure 35 for the truss with concrete slab.

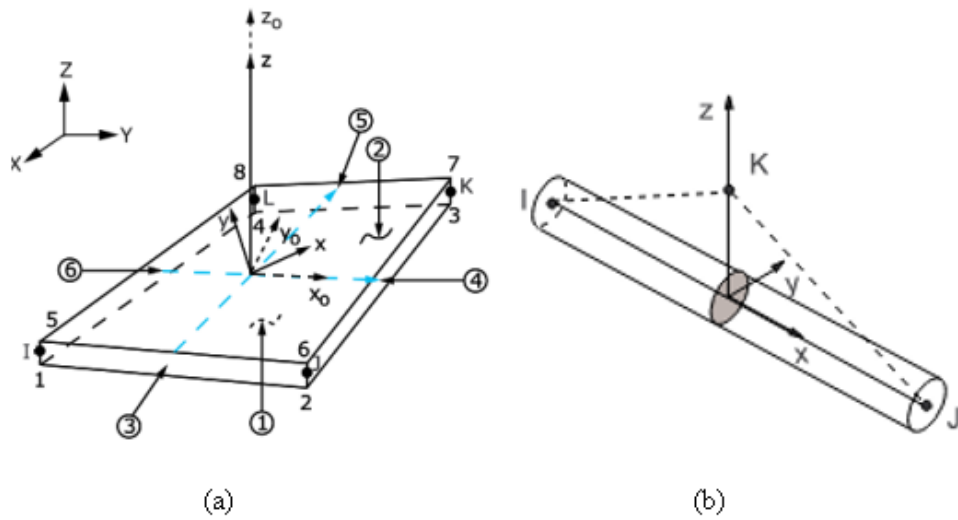


**Figure 34.** Finite element model for bare truss



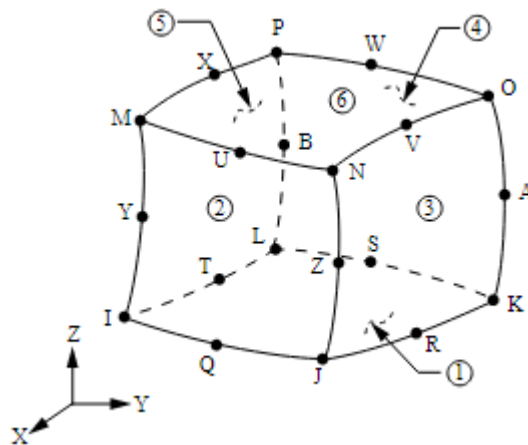
**Figure 35.** Finite element model for truss with concrete slab

Shell 181 elements, used to model the truss chords (shown in Figure 36a) are suitable to analyze thin to moderately thick shell structures [32]. They are appropriate for linear, large rotation or large strain nonlinear applications. The element has four nodes with six degrees of freedom at each node. Beam 188 elements used for diagonal members are three-dimensional 2-node beam elements (Figure 36b). They are based on Timoshenko beam theory and are appropriate for linear, large rotation or large strain nonlinear applications. Stress stiffness terms are included in the element, which enables the analysis of lateral, torsional and flexural stabilities [32].



**Figure 36.** Elements used in FE models: (a) Shell 181, (b) Beam 188 [32]

Solid 186 element shown in Figure 37 was used for modeling the concrete. Solid 186 is a 20-node homogeneous structural solid element that exhibits quadratic displacement behavior [32].



**Figure 37.** Geometry for Solid 186 element [32]

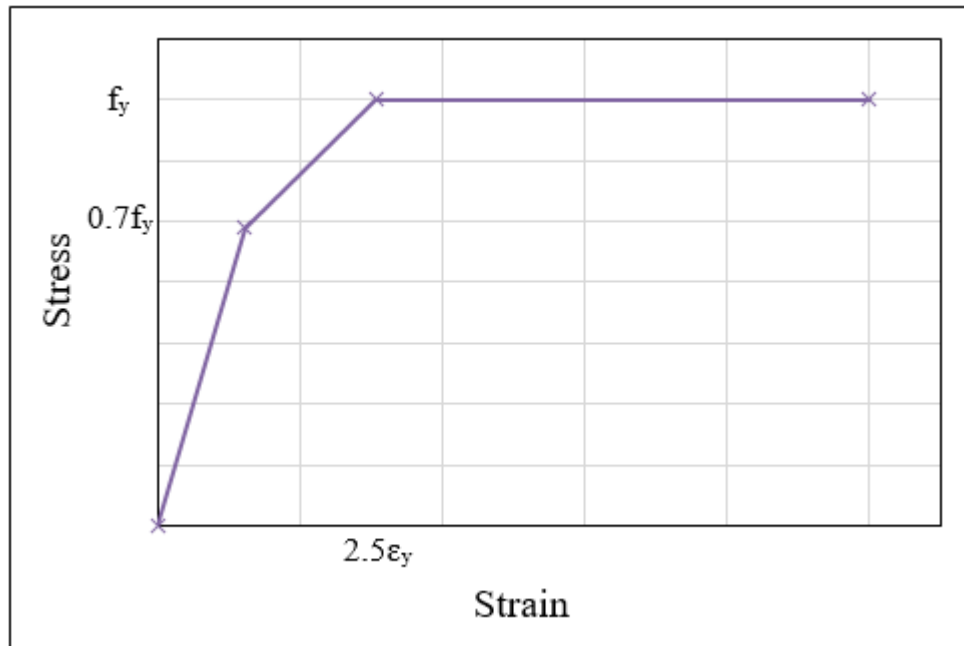
The boundary conditions in models were specified according to the support conditions used during the tests. At both truss ends, the top chord was only restrained

in the lateral direction, whereas the bottom chord was simply supported. One end of the bottom chord was restrained in longitudinal, lateral and vertical directions while the other end was set to be free in the longitudinal direction. Different from the actual experimental setup, lateral supports were introduced to the system at chord-diagonal connection joint locations at the top chord in order to obtain a more stable numerical response.

The connection between the diagonal elements and the chords was simulated using contact elements (CONTA 174, TARGE 170) as bonded connection. Since the axial flexibility of the connection between the diagonal and chord members was reflected in the model by adjusting the cross-sectional area of diagonal members, the connection was modelled as bonded.

Bodies forming the CFS chord members as well as the concrete filling and concrete slab were typically divided into 10 mm sized uniform meshes. For the concrete included models, the bond between the concrete and steel parts was established using contact elements and bonded type connection. Since no slip deformation was observed between the CFS section and the concrete infill during the tests, this type of connection was considered to be suitable.

The measured strength values were used for the definition of steel material model. The yield strength and ultimate strength values used in FE models were 350 MPa and 500 MPa, respectively. The residual stresses that are known to be present in CFS members were included in FE models by reducing the elastic limit, as shown in Figure 38. Based on the adopted stress-strain model for steel, first yielding occurs at 70% of the actual yield strength. After yielding, the material hardens up to yield strength at a strain value that corresponds to 2.5 times the yield strain.



**Figure 38.** Steel material model used in FE analyses

According to experimental observations there was no visible concrete crushing in truss specimens tested with concrete infilled compression chord and concrete slab. Limited concrete cracking was observed in the truss specimen tested with concrete slab, as mentioned earlier. Based on these observations, a linear elastic material model was used for concrete in the FE models prepared for concrete infilled specimens. The required mechanical properties were defined according to the material tests performed on concrete samples. The compressive strength and the modulus of elasticity values were specified as 30 MPa and 31800 MPa, respectively. For the specimen WB\_Slab the Drucker & Prager concrete model was used for the FE analysis. The mechanical properties were defined as 30 MPa for the compressive strength, 2 MPa for the tensile strength and 31800 MPa for the modulus of elasticity.

Each FE model was loaded by applying nodal displacements. Such a displacement controlled loading eliminated the numerical convergence problems that are commonly faced with when force-controlled loading is used.

### 3.1.1. Analysis Methods

Three type of analysis, namely Materially Nonlinear Analysis (MNA), Geometrically and Materially Nonlinear Analysis (GMNA) and Geometrically and Materially Nonlinear Analysis with Imperfections (GMNIA) were conducted using the FE models. For the MNA model, only material nonlinearity was activated. For the GMNA model, both the material nonlinearity and the geometric nonlinearity were activated. The geometric nonlinearity was triggered by allowing large deformations in the model. In this analysis, second order effects and buckling deformations were considered. In the GMNIA model, the imperfections in CFS members were imposed in the model according to the determined eigenmodes of the system. The mode shapes were determined through a linear eigenmode analysis using the existing boundary conditions. The deflected shape obtained from the eigenmode analysis was exported from the model and used to specify the initial imperfections. The imperfection amplitudes were determined with the formulation suggested by Schafer and Peköz [10].

$$d_1 \approx 6te^{-2t} \quad (3)$$

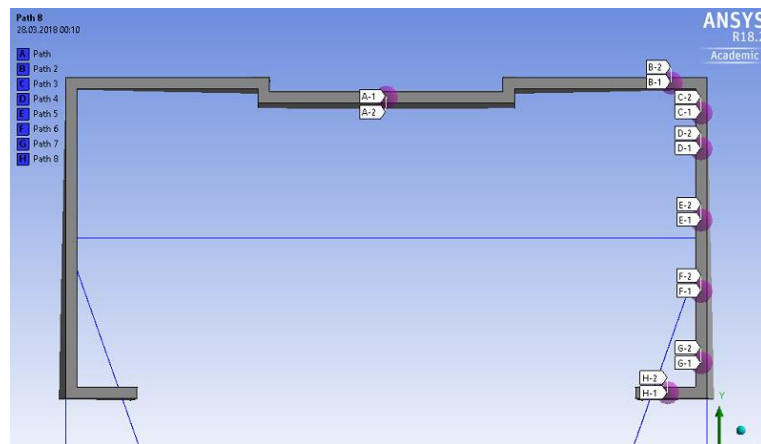
where  $d_1$  is the imperfection amplitude and  $t$  is the CFS member thickness in mm.

In MNA, the loading was continued up to the point where the experimental failure was observed or the experiment was terminated. For GMNA and GMNIA, since the geometric nonlinearity was activated, buckling of the top chord CFS member was observed. Such buckling failure was usually evident with nonconvergence in the analysis. For the specimens without concrete, the analysis was terminated when deviation from the behavior was observed, which was usually detected when instability problems due to buckling and sudden load decrease was observed in the load-deflection graphs. The results obtained from the model are compared to the analysis results in the following parts.



### 3.2. Analysis Results

Comparison of the measured and predicted behavior of trusses is presented in terms of both the global load-deflection response and the local strain response. In order to record the cross sectional strains from FE models, strain probes were inserted in the model at the points where strain gages were used on truss specimens during experimental phase. Nodal paths similar to the one shown in Figure 39 were defined to extract the numerically determined strain profiles through depth of CFS chord members.



**Figure 39.** Path locations to extract cross-sectional strains in FE model

#### 3.2.1. Bare CFS Specimens

##### 3.2.1.1. Specimen WT\_Control

A comparison of experimentally measured and numerically predicted load-deflection response of specimen WT\_Control is given in Figure 40. All three types of analyses resulted in identical initial stiffness. In models including geometric nonlinearities (GMNA and GMNIA), the load carrying capacity is estimated as approximately 3% lower than the experimentally determined load capacity. Compression chord buckling was observed in these models and further increase of load application was not possible. The difference between GMNIA and GMNA is visible only when the ultimate load is reached, in other words, when buckling occurs. When imperfections are present in the model, the truss tends to fail at a slightly lower load and midspan

deflection. Deformed shapes obtained from GMNA and GMNIA are shown in Figure 41.

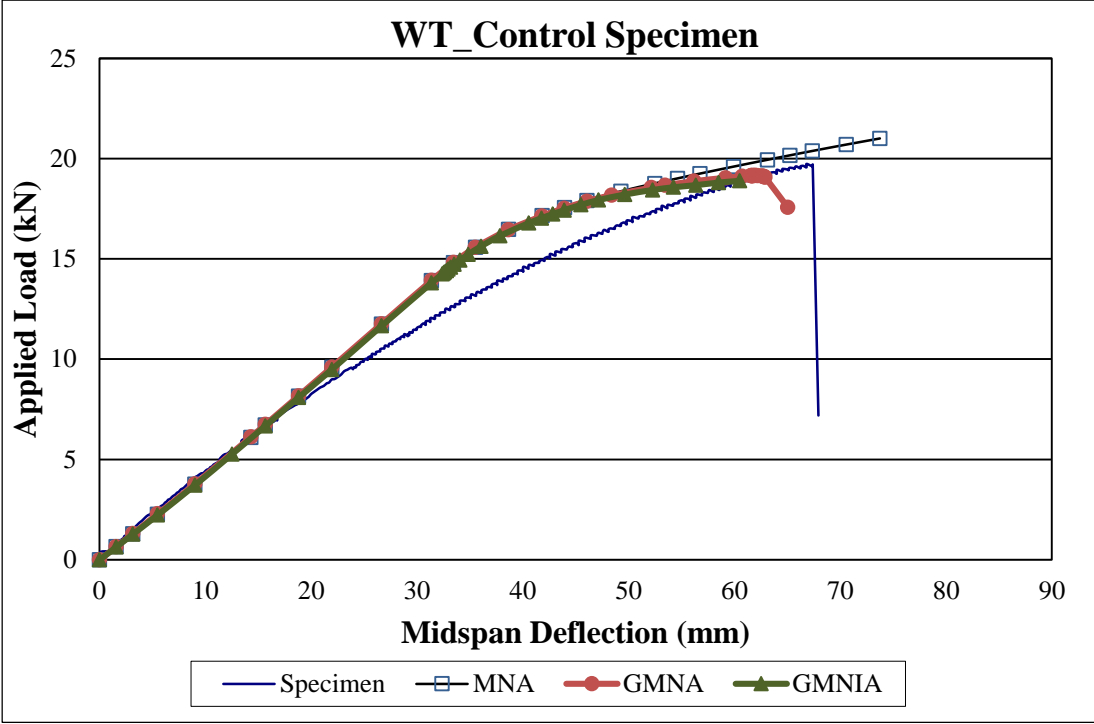


Figure 40. Measured and predicted load-deflection response of specimen WT\_Control

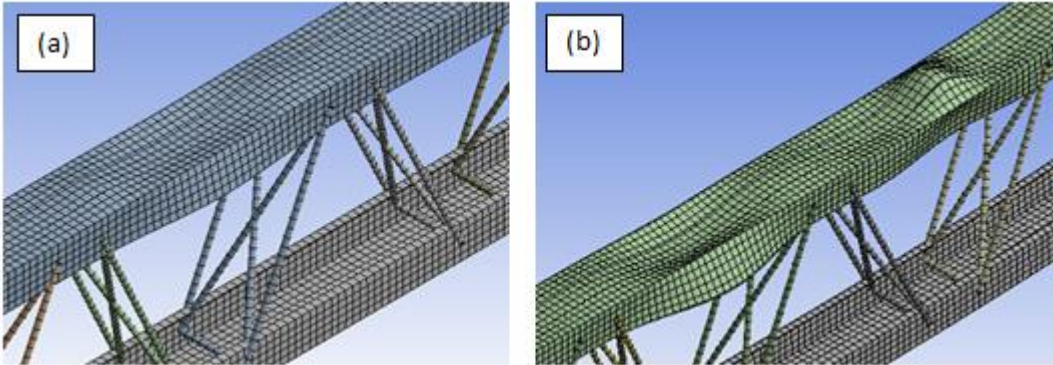
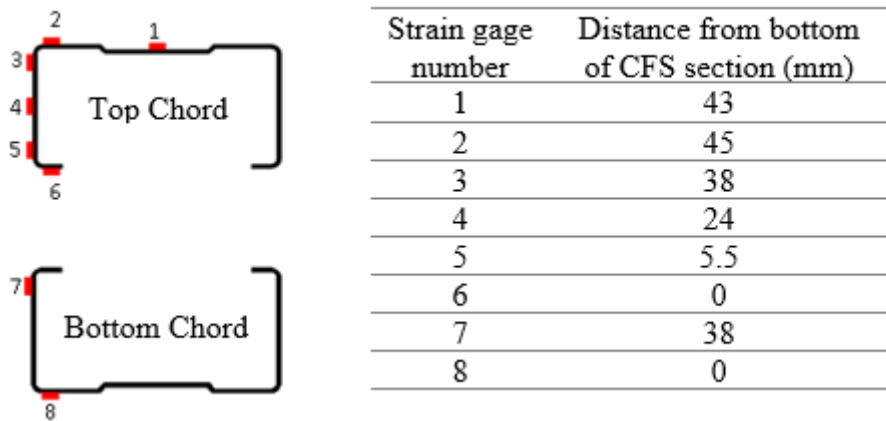
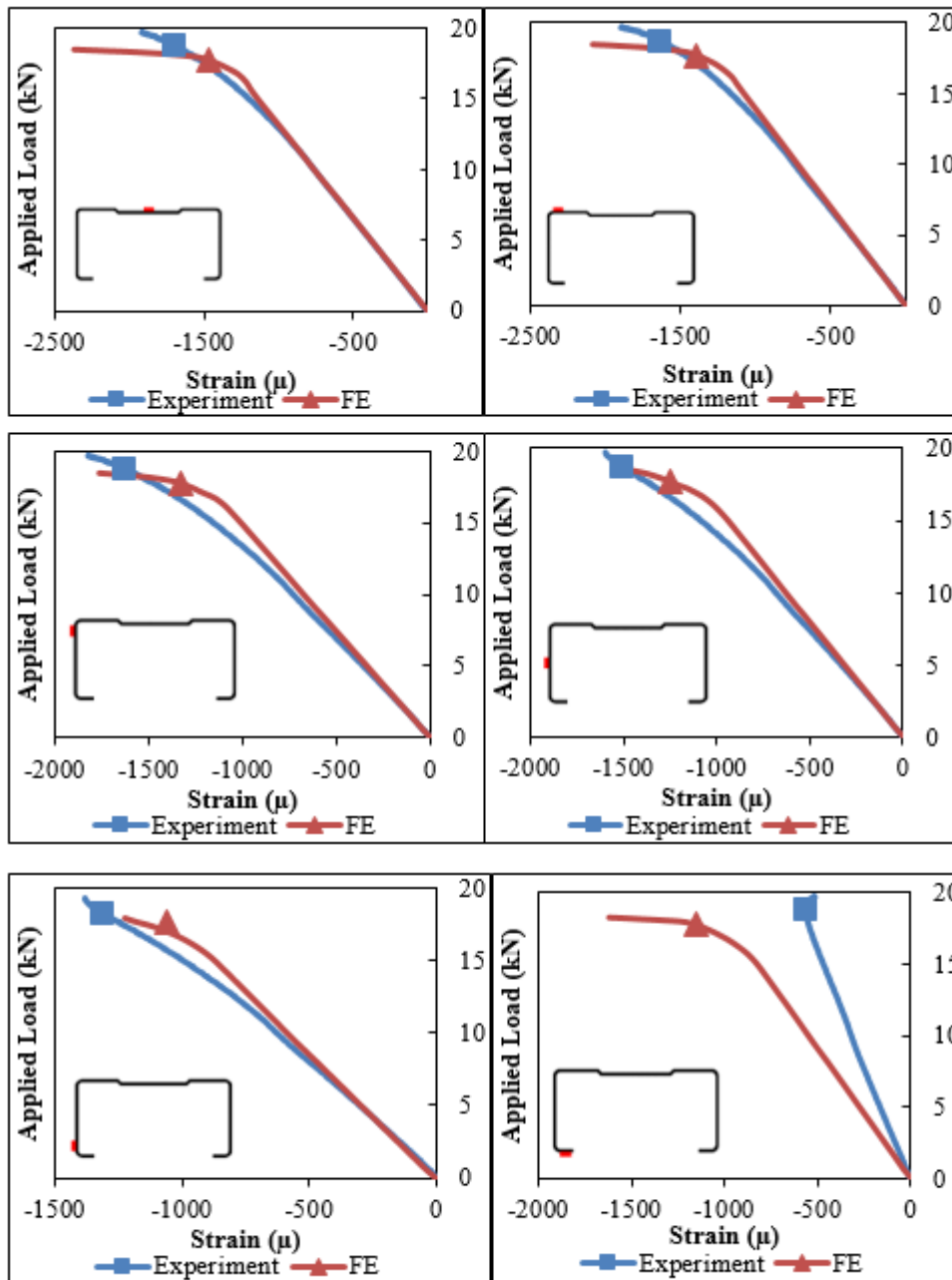


Figure 41. Specimen WT\_Control deformed shape: (a) MGNA, (b) MGNIA

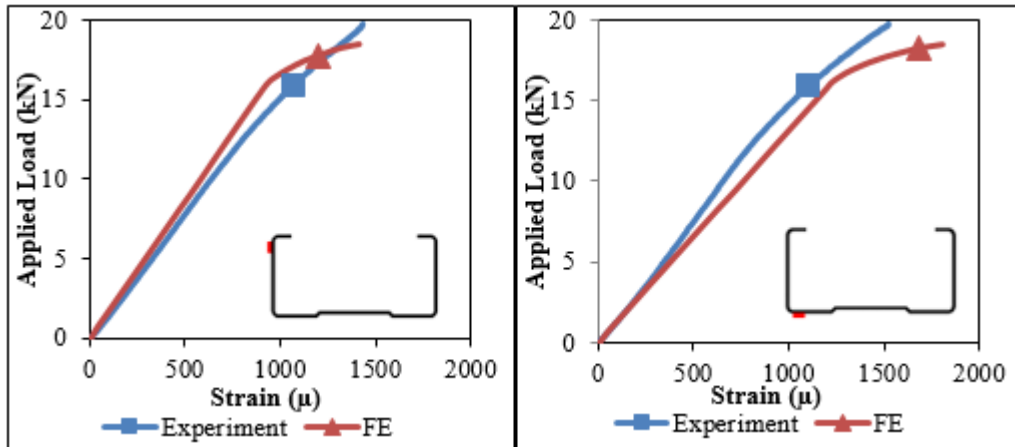
The strain gage locations on the top and bottom chords of the specimens are given in Figure 42. Variation of top and bottom chord strains at midspan cross section determined from GMNIA is presented respectively in Figure 43 and Figure 44 together with the measured load-strain response. The numerical strain values represent CFS section strains recorded at these locations. Negative values in the plots indicate compressive strain and positive values indicate tensile strain. The plots in Figure 43 indicate that while the model is able to simulate the actual behavior for strain gages inserted at the stiffened elements of the compression chord CFS section, the measured and numerically predicted strain values differ significantly for the lip part of the section. The measured lip strains are significantly smaller than those predicted by the FE model. This suggests that the lip part of the CFS section in compression chord does not resist stresses as effectively as the rest of the cross section. As evident in the plots provided in Figure 43 compressive strain values exceeding  $2000 \mu\epsilon$  were measured by the strain gages located in the web of the top chord CFS. This is an indication of steel yielding within the member at this location. The numerically determined bottom chord CFS member strain variations shown in Figure 44 are also in good agreement with the measured response.



**Figure 42.** Strain gage locations in specimen WT\_Control

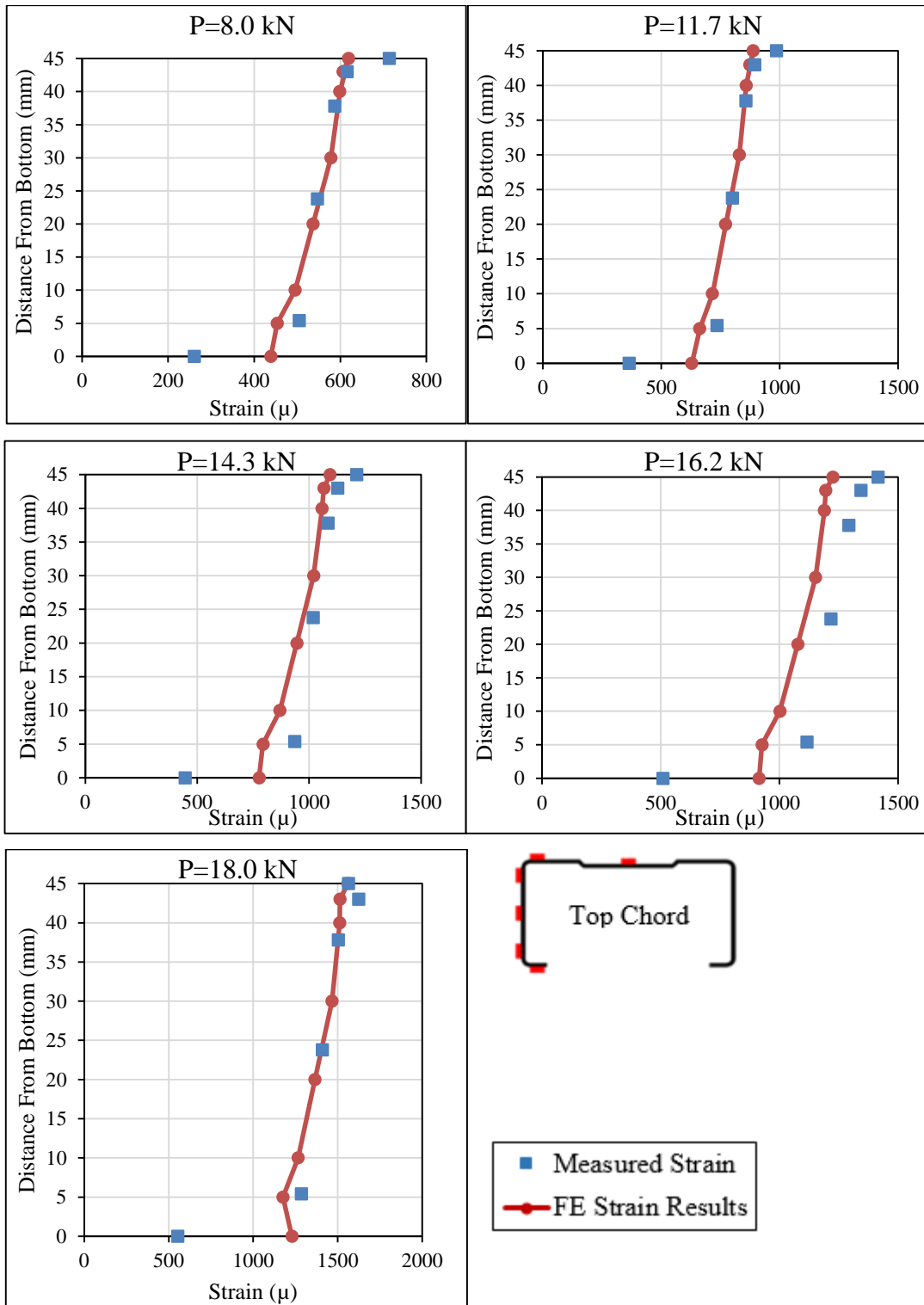


**Figure 43.** Top chord load-strain response in specimen WT\_Control

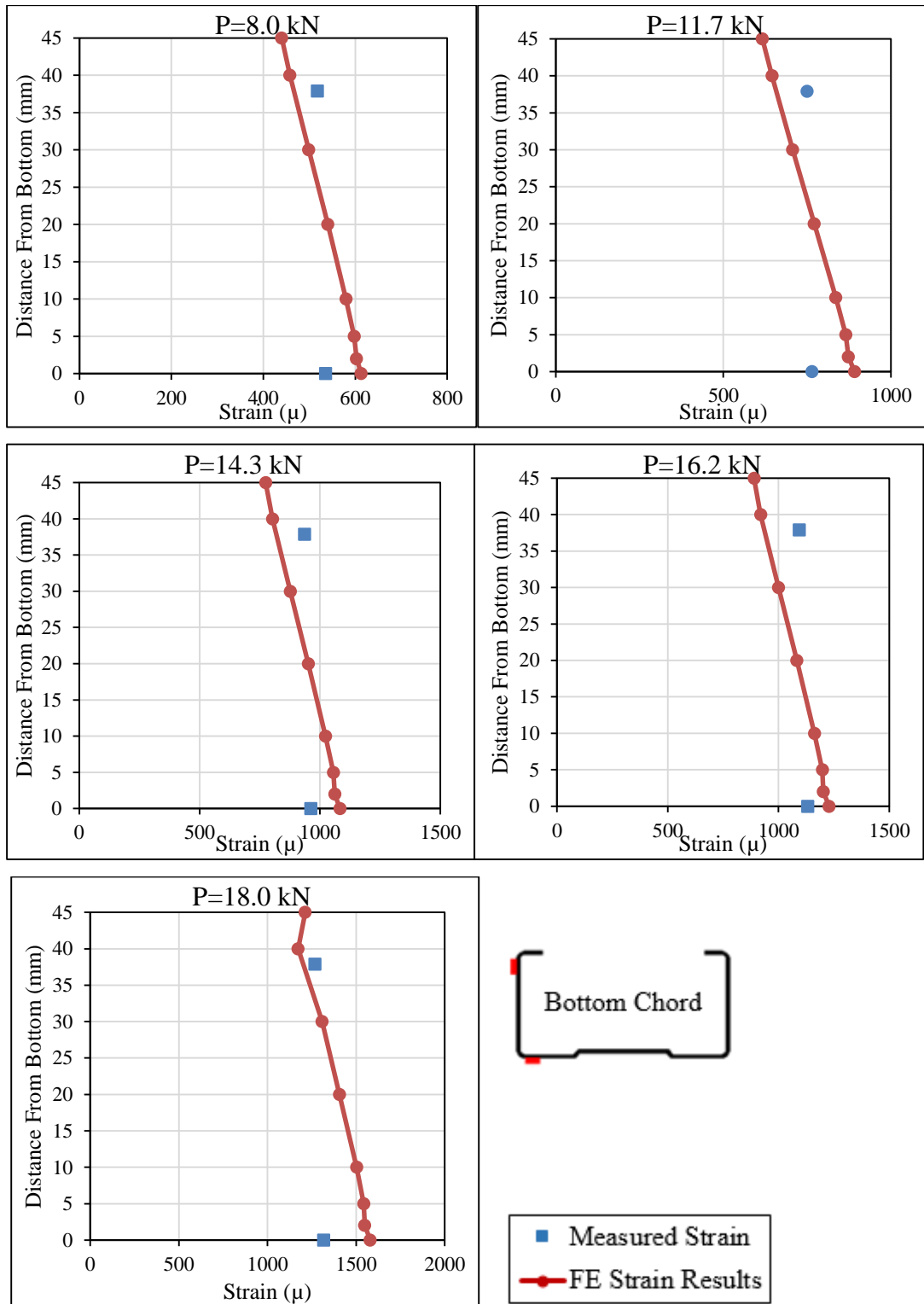


**Figure 44.** Bottom chord load-strain response in specimen WT\_Control

Cross-sectional strain profiles from GMNIA for the midspan section of the top chord and bottom chord members are plotted in Figure 45 and Figure 46, respectively. Superimposed on the same plots are the strain values recorded by strain gages during load testing of the corresponding truss specimen. Strain profiles were plotted for several load values including the loads corresponding to the linear-elastic response and the maximum load capacity of the truss. For all load levels shown, the measured and predicted strain profiles are observed to agree well. As mentioned earlier, the strain gage located at the lip of compression chord CFS member consistently indicates smaller strain than the expected value.



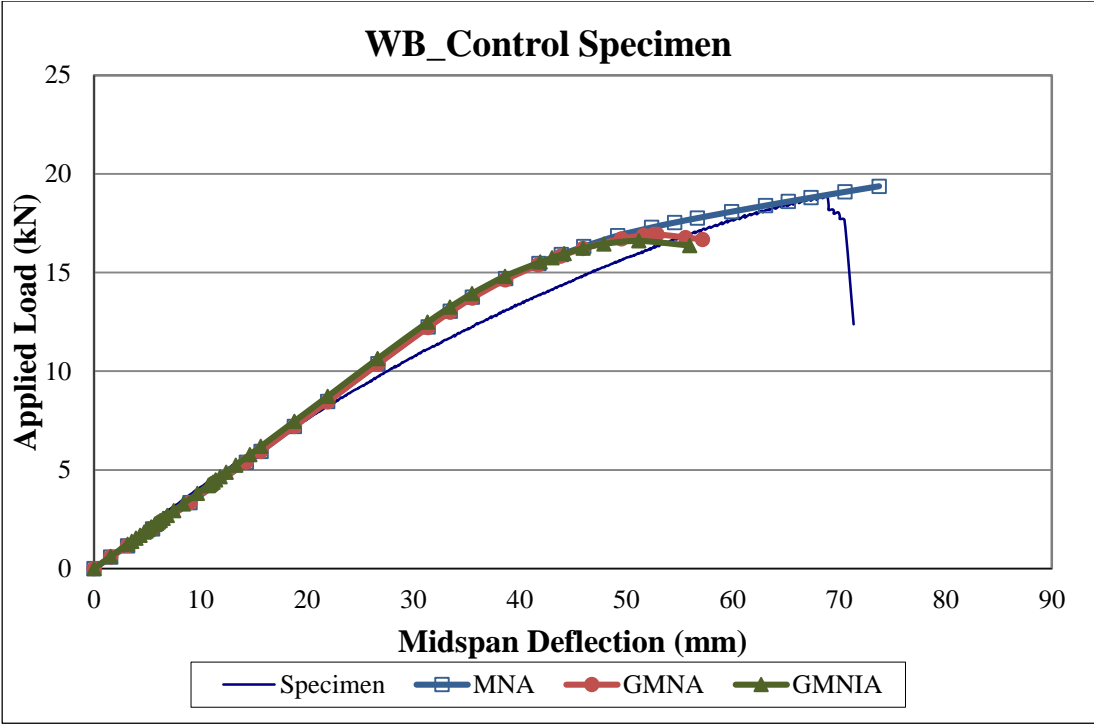
**Figure 45.** Specimen WT\_Control top chord midspan strain values; experiment vs. model values



**Figure 46.** Specimen WT\_Control bottom chord midspan strain values; experiment vs. model values

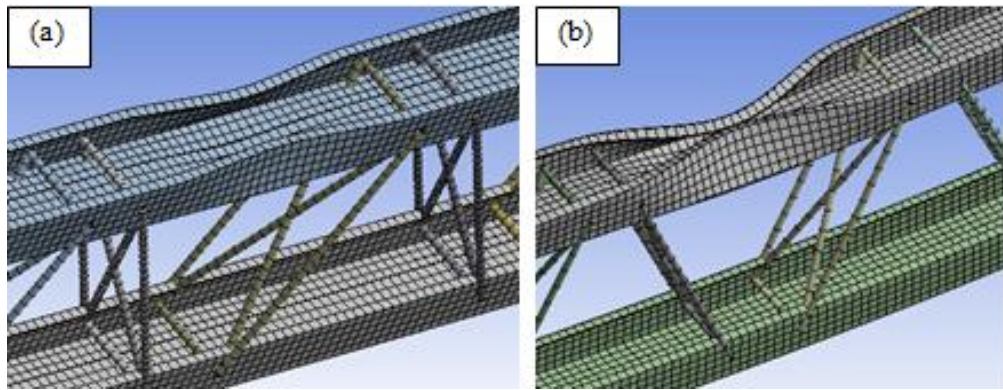
**3.2.1.2. Specimen WB\_Control**

Comparison of the load-displacement response determined from the three levels of finite element analyses with the experimentally determined response of specimen WB\_Control is presented in Figure 47. GMNA and GMNIA resulted in underestimation of the load capacity by approximately 10%. The FE models correctly captures the compression chord local buckling failure mode, as shown in Figure 48.



**Figure 47.** Measured and predicted load-deflection response of specimen WB\_Control





**Figure 48.** Specimen WB\_Control deformed shape: (a) MGNA, (b) MGNIA

The cross-sectional strain comparisons were only conducted for the FE results, since no strain measurement is available for this specimen. The strain distribution for top and bottom chord CFS sections are plotted in Figure 49 and Figure 50, respectively. The strain profiles indicate the presence of flexural effect on both chord members. Bottom chord strain profile remained linear throughout the entire loading, while the top chord strain profile deviated from the initial linear response close to approximately 90% of the maximum load level. At this point, the compressive strain in lip part of the top chord CFS member started to increase abruptly, indicating the initiation of local buckling in the cross section.

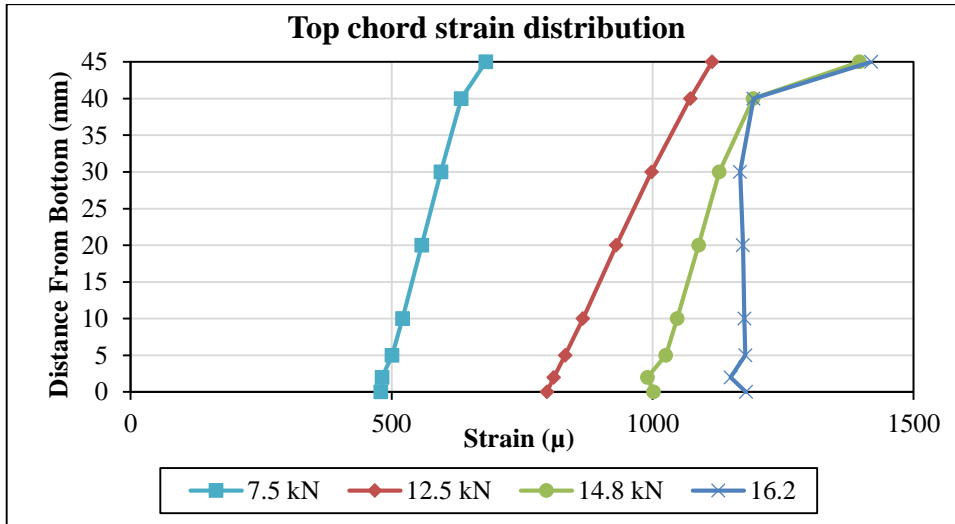


Figure 49. Specimen WB\_Control top chord midspan strain distribution

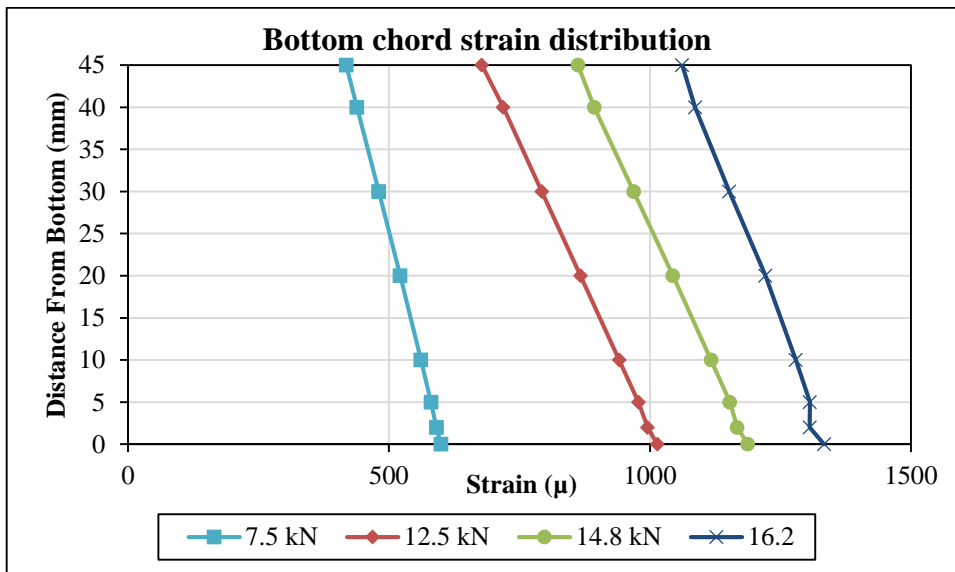
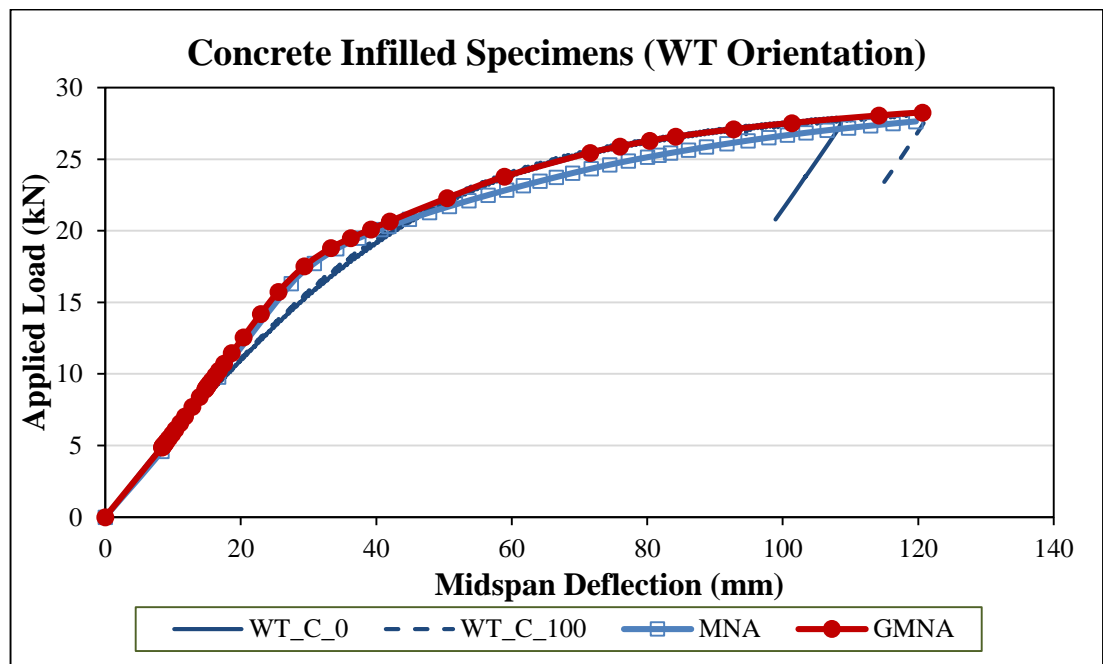


Figure 50. Specimen WB\_Control bottom chord midspan strain distribution

### 3.2.2. Concrete Infilled Specimens

#### 3.2.2.1 Specimens WT\_C and WT\_C\_100

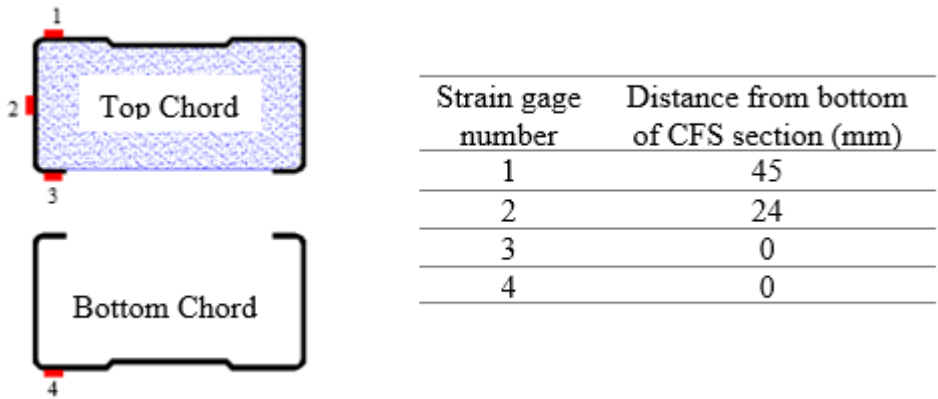
As mentioned earlier, specimens WT\_C and WT\_C\_100 both have the top chord CFS member looking down and filled with concrete. The only difference between these two specimens is the presence of additional self-tapping screws attached on both flanges of the top chord CFS member in specimen WT\_C\_100 in an attempt to improve the bond between the CFS member and concrete infill. However, experimental results indicate that this construction detail had minimal effect on the response of these two specimens. Based on this observation, both of these specimens were represented by a single FE model with bonded type contact between the top chord CFS member and concrete infill. Results obtained from this FE model and the comparison with the experimental results are presented below.



**Figure 51.** Measured and predicted load-deflection response of Specimen WT\_C

Comparison of the numerically predicted and experimentally determined load-deflection responses is provided in Figure 51. A slight difference exists between the results from MNA and GMNA, and both types of analyses resulted in accurate

prediction of the global truss response when compared with the measured response. As mentioned earlier, for the concrete infilled truss FE model and the FE model including a concrete slab placed over the truss, the initial imperfection of the CFS members was not considered. Therefore, no GMNIA was conducted with these models.



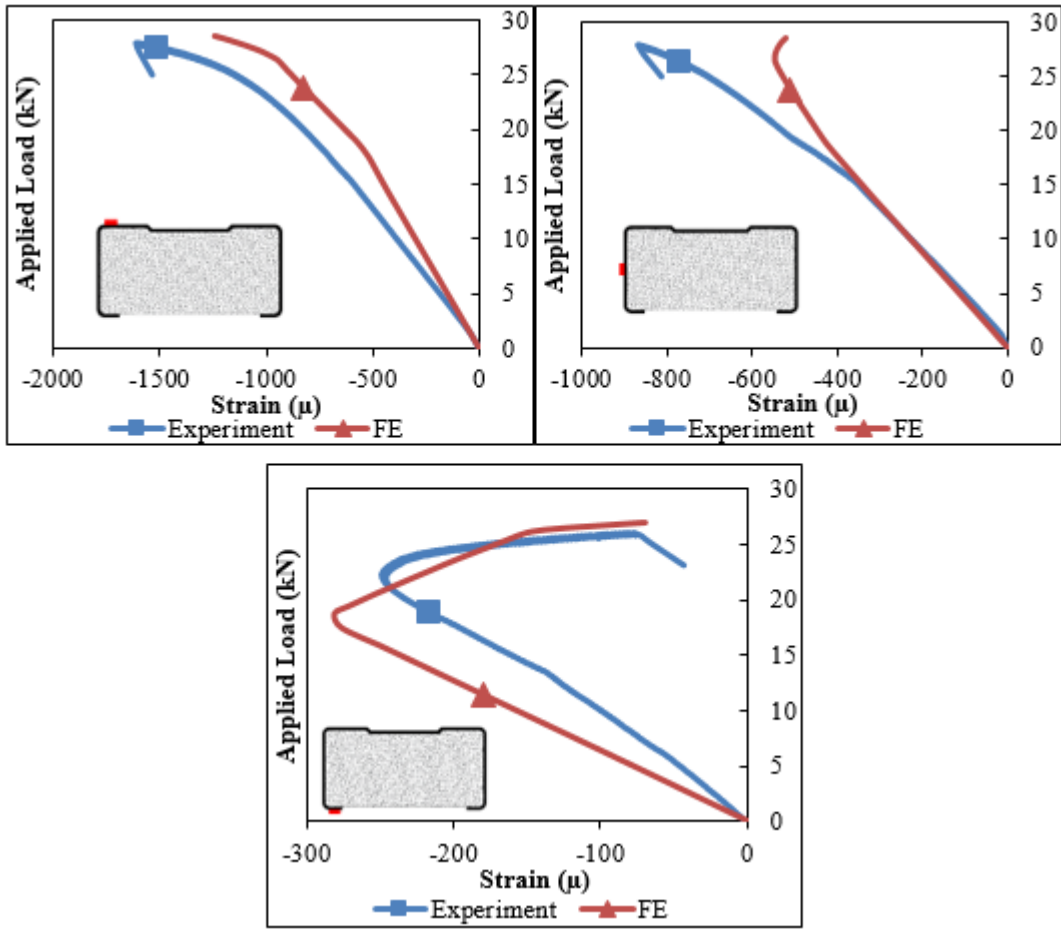
**Figure 52.** Specimen WT\_C strain gage locations

Strain gage locations on top and bottom chord CFS members in specimen WT\_C are indicated in

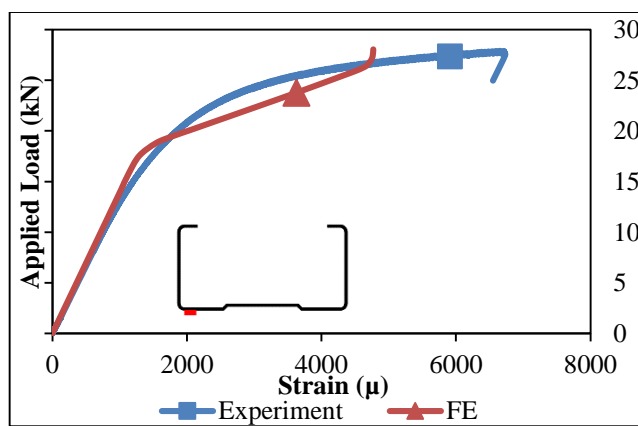
Figure 52. Variation of strain readings from these gages, as well as the corresponding results from FE models are presented in Figure 53 and Figure 54. The FE model is able to predict the cross-sectional strains in compression chord CFS member with acceptable accuracy, except for the lip part of the section. The measured and numerically predicted strain values differ significantly for the lip part. The measured lip strains are significantly smaller than those predicted by the FE model. This suggests that the lip part of the CFS section in compression chord does not resist stresses as effectively as the rest of the cross section. Although a similar behavior was also valid for the case of trusses tested without concrete infill as mentioned earlier, the difference in the concrete infilled specimens is not as critical.

The lip strains in Figure 53 indicate a linear increase with the amount of load at the beginning of loading. In this region, bending deformation of truss chords is small and the tensile strain in the lip due to flexural effect remains below the compressive strain due to chord normal force. With further loading, bending deformation of truss chords becomes more significant and the resulting tensile strain in the lip part of the cross section in top chord member overcomes the compressive strain due to chord normal force. The result is “decompression” of top chord lip strains, as evident in the bottom plot in Figure 53. It is important to note that both the experimental and numerical data show this type of decompression behavior.

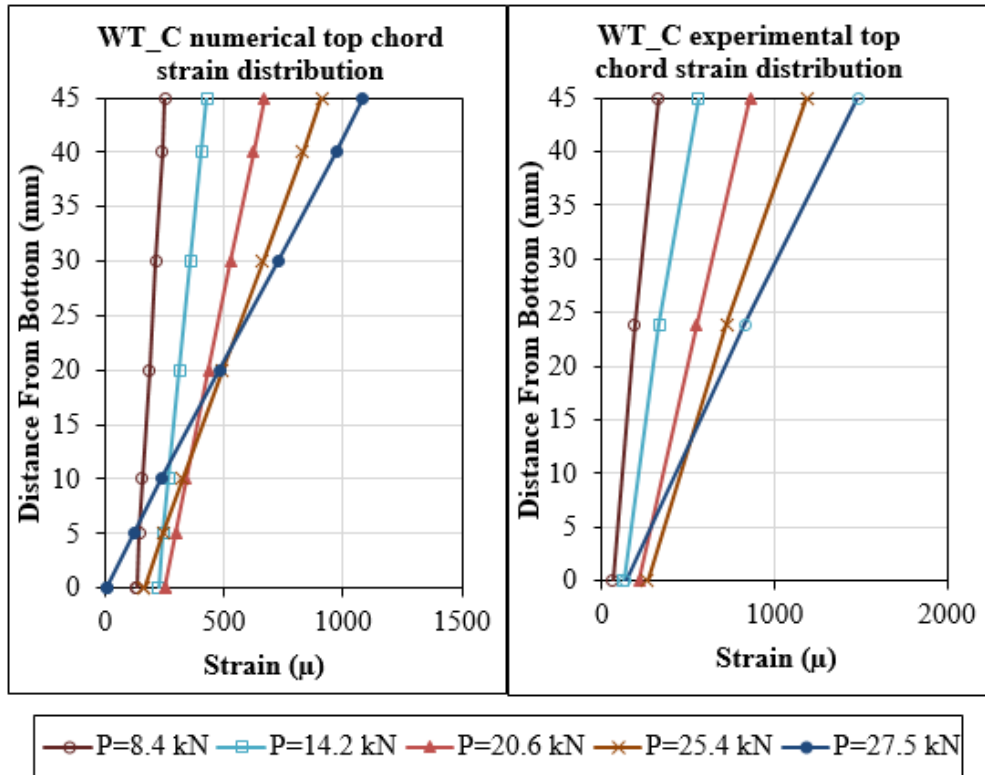
Variation of bottom chord strains with loading is presented in Figure 54 using both the experimental and numerical data. The FE and experimental curves follow each other closely. Significantly large tensile strains occur at the web part of the truss bottom chord, indicating the yielding of this member under load levels well below the experimentally measured maximum load.



**Figure 53.** Top chord load-strain response in specimen WT\_C

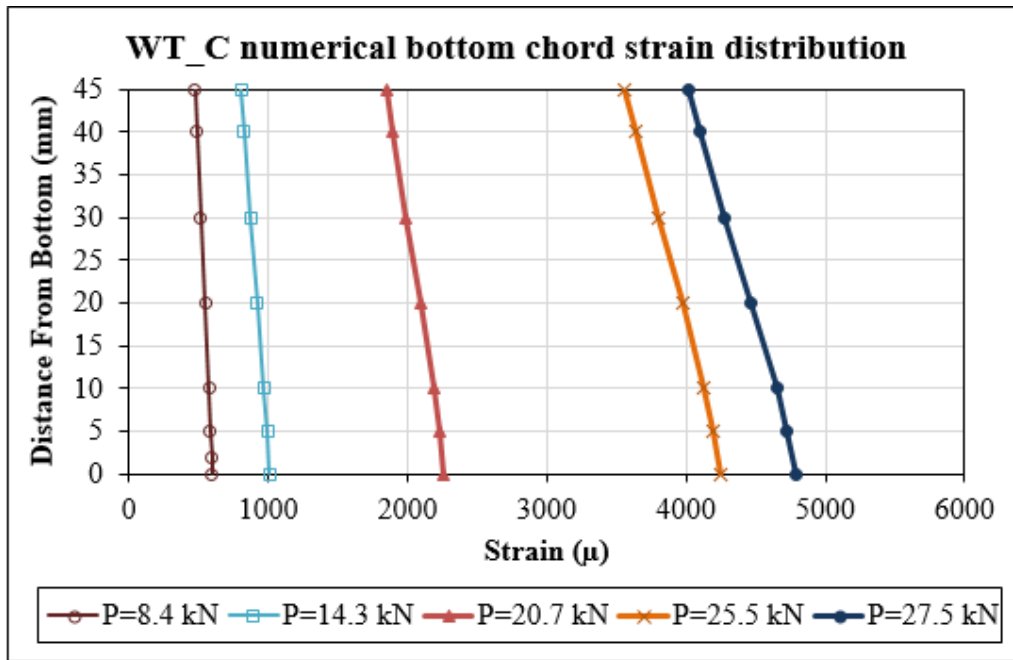


**Figure 54.** Bottom chord load-strain response in specimen WT\_C



**Figure 55.** Specimen WT\_C numerically determined and experimentally measured top chord strain distribution

Variation of measured and predicted top chord CFS member strain profiles under increasing level of load is plotted in Figure 55. Both sets of data indicate larger strain gradient with increasing loading. This is due to the fact that bending deformation of chord members becomes more significant as the loading on the truss is increased. Such increased flexural effect resulted in larger strain gradient on chord members with increasing loading. The numerically determined strain profiles are provided for the bottom chord CFS member in Figure 56. Similar to the top chord member, increased bending effects resulted in larger strain gradient in bottom chord CFS member under increasing loading.

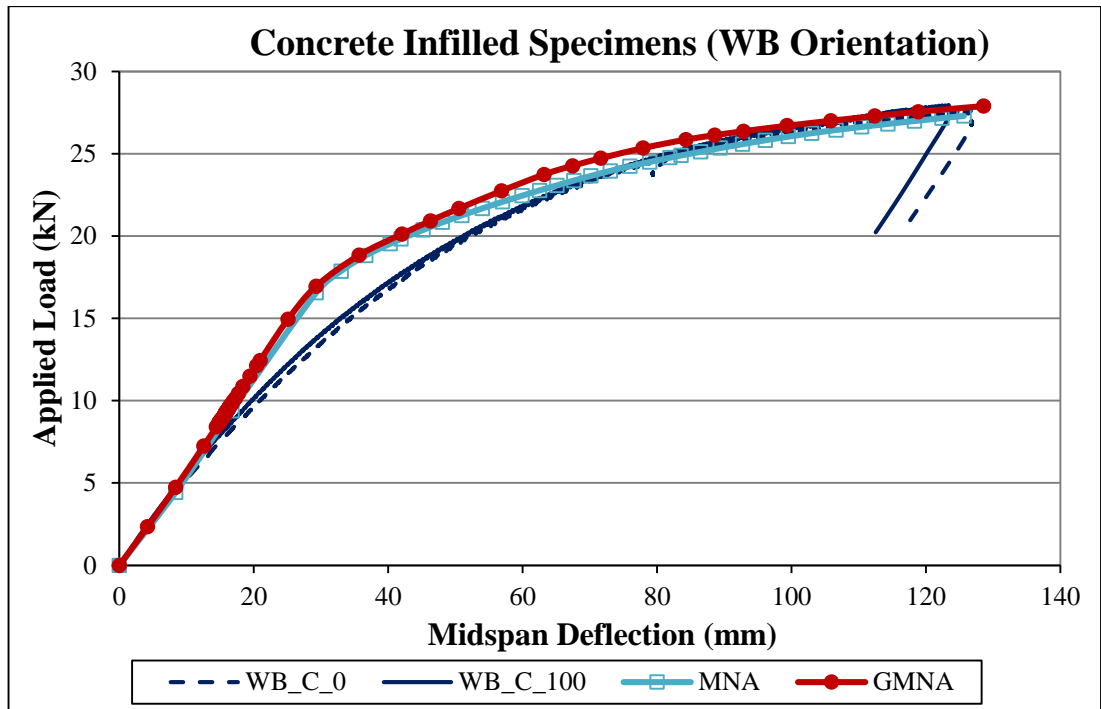


**Figure 56.** Specimen WT\_C numerically determined bottom chord strain distribution

### 3.2.2.2. Specimens WB\_C and WB\_C\_100

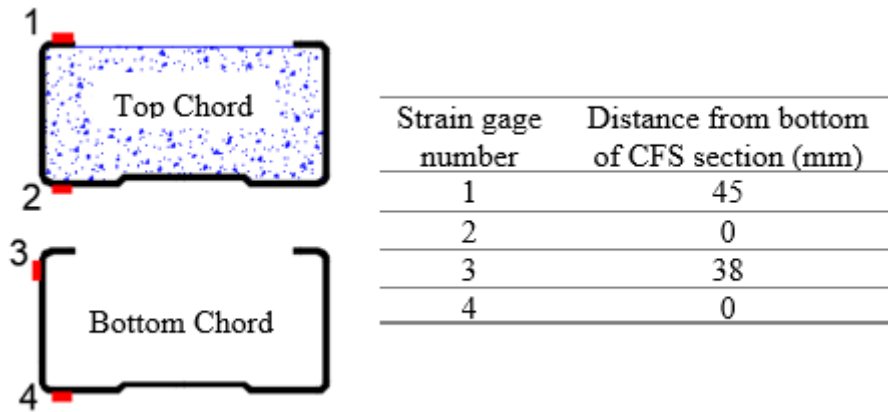
Experimental results obtained from specimens WB\_C and WB\_C\_100 and the numerical results obtained from the FE model representing these specimens are provided in this section. Figure 57 shows that there is an acceptable match between the experimentally determined load-deflection response and those obtained from MNA and GMNA. The numerical results show a faster stiffness reduction than the measured response. This can be attributed to the type of stress-strain material model for steel adopted in FE models. The steel material model that is represented by a perfectly plastic plateau with 30% residual stress assumption may not correctly represent the actual material response.



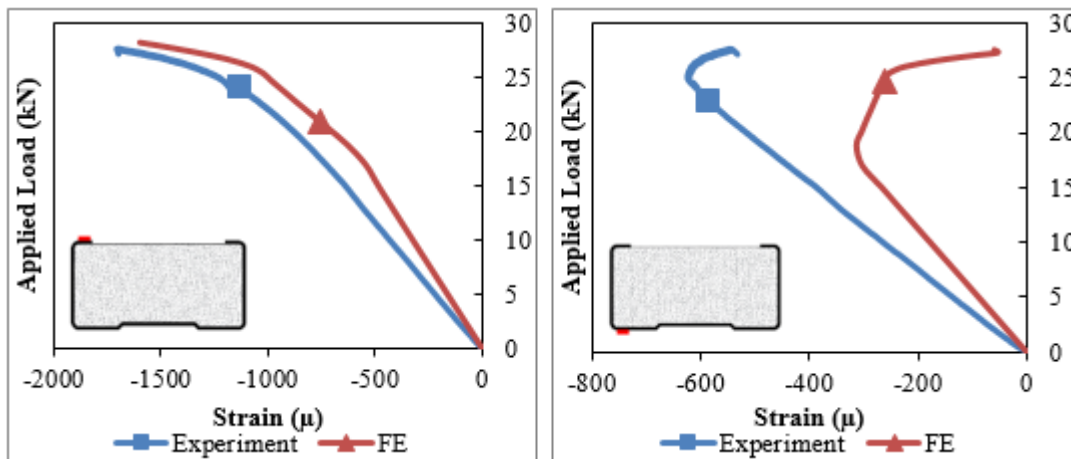


**Figure 57.** Measured and predicted load-deflection response of specimen WB\_C

Strain gage locations on top and bottom chord CFS members in specimen WB\_C are indicated in Figure 58. Variation in top chord CFS member strains is plotted in Figure 59. Strain decompression in web part of the top chord member due to significant flexural effect is also valid for this specimen. Similar to the concrete filled specimens with the top chord in web-at-top configuration, both the measured data and the FE results show the decompression behavior.

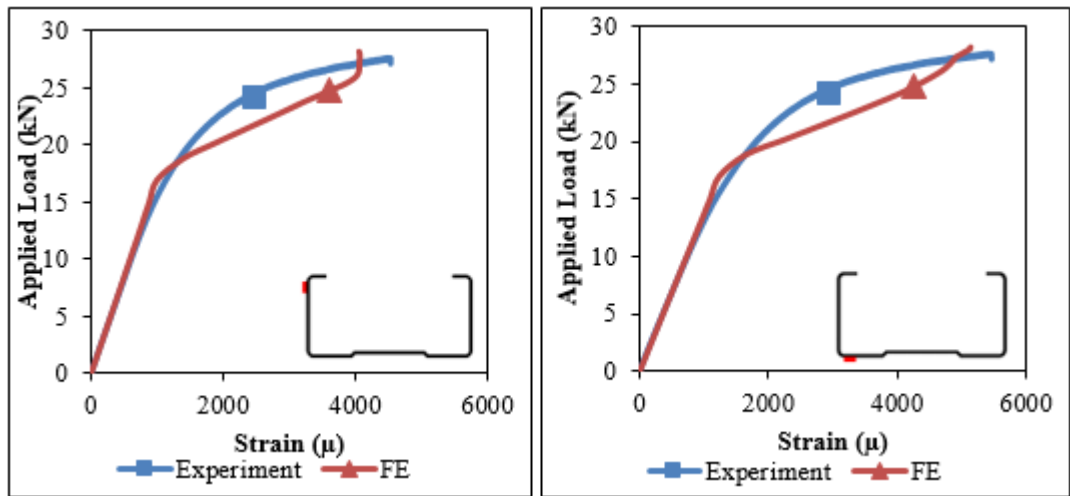


**Figure 58.** Specimen WB\_C strain gage locations

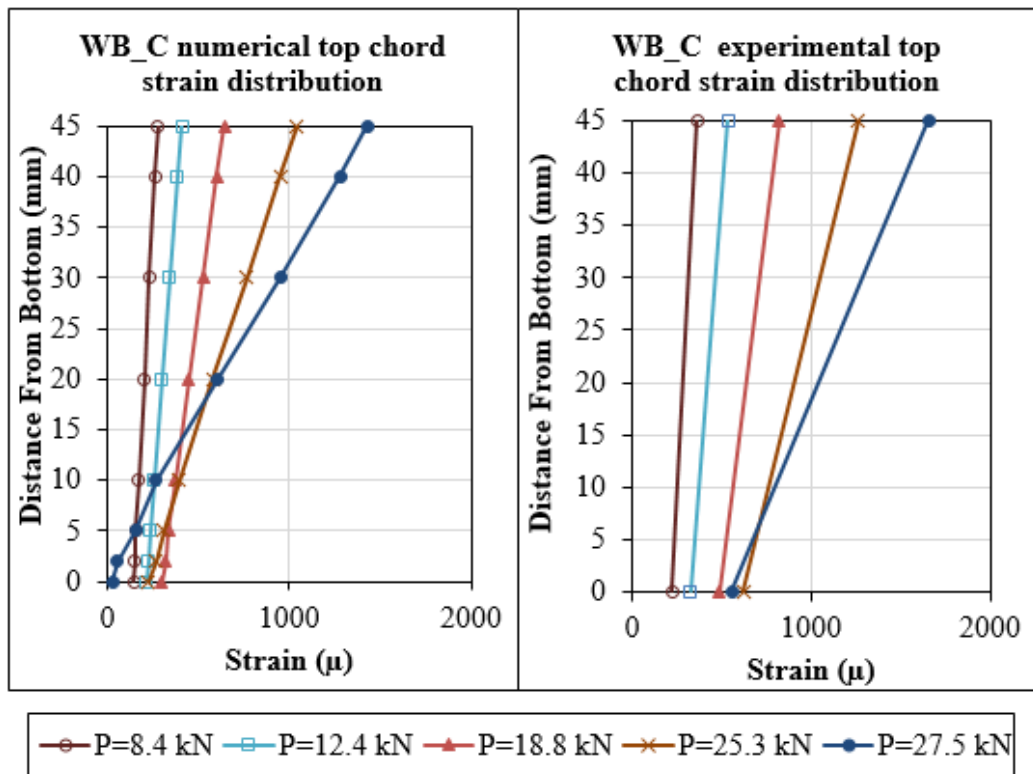


**Figure 59.** Top chord load-strain response in specimen WB\_C

The bottom chord strain comparison given in Figure 60 shows a good agreement between the measured and predicted responses. Similar to the case with the previous group of specimens both the experiments and FE models indicate yielding of bottom chord CFS member, as evident by significantly large strain values. The numerically determined strain variation shows a faster stiffness reduction than the measured response. As mentioned earlier in this section, this is attributed to the steel stress-strain material model used in the FE analysis. Steel material model is idealized as perfectly plastic in post-yield region, which cannot accurately simulate the actual material behavior.

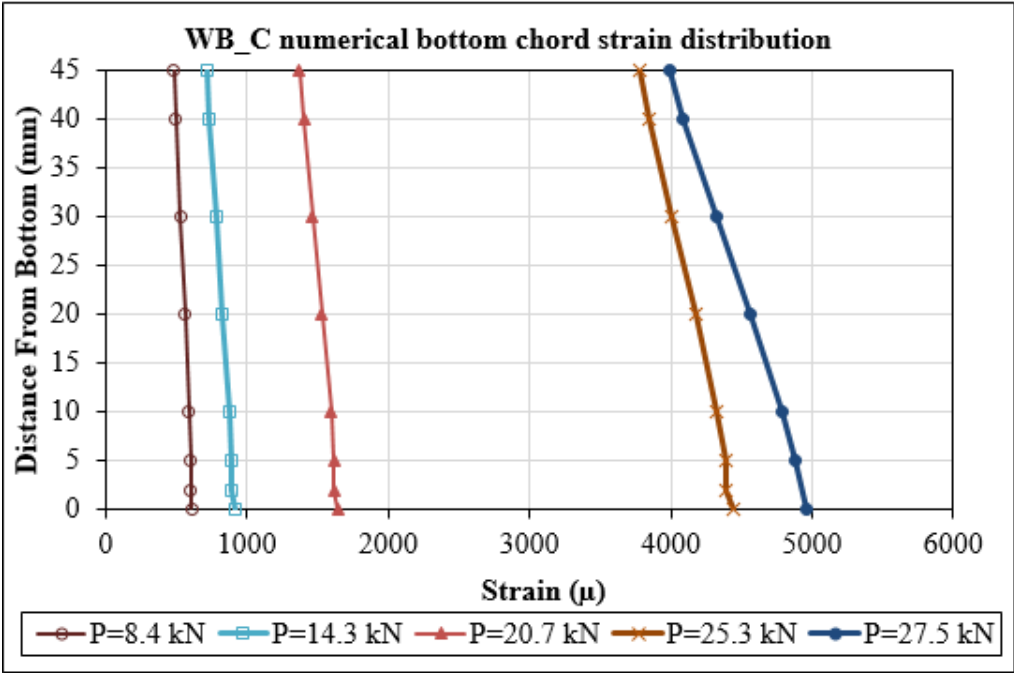


**Figure 60.** Bottom chord load-strain response in specimen WB\_C



**Figure 61.** Specimen WB\_C numerically determined and experimentally measured top chord strain distribution

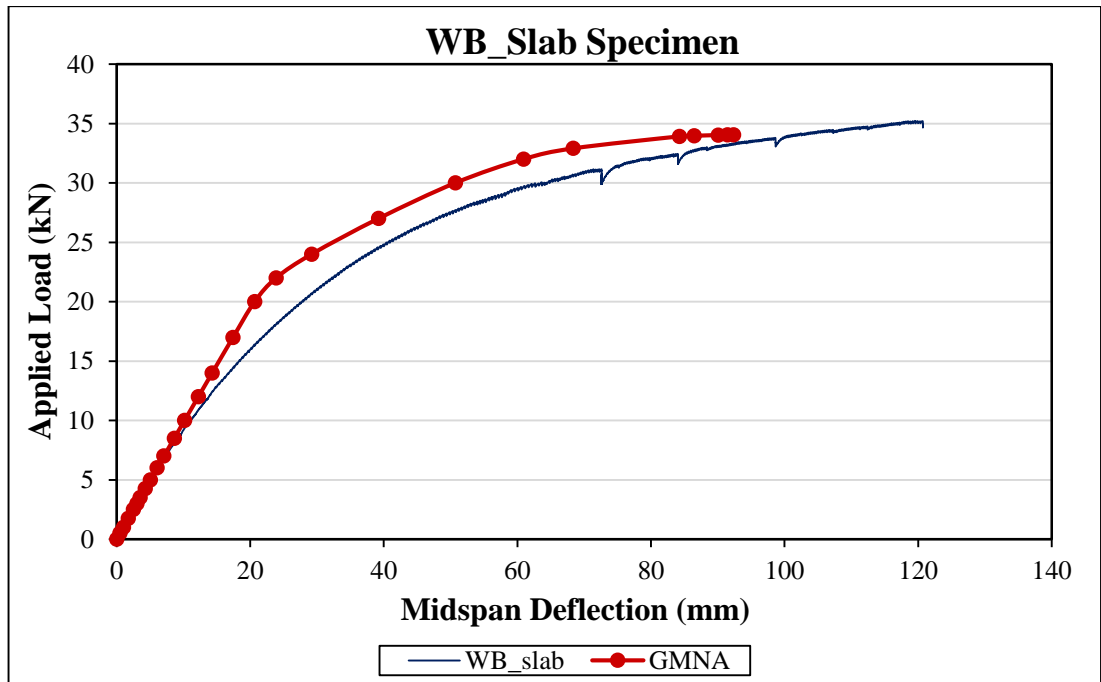
Variation of measured and predicted top chord CFS member strain profiles under increasing level of load is plotted in Figure 61 for specimen WB\_C. Both sets of data indicate larger strain gradient with increasing loading. This is due to the fact that the flexural effect on chord members becomes more significant as the loading on the truss is increased. The numerically determined bottom chord strain profiles provided in Figure 62 show the similar response, as well.



**Figure 62.** Specimen WB\_C numerically determined bottom chord strain distribution

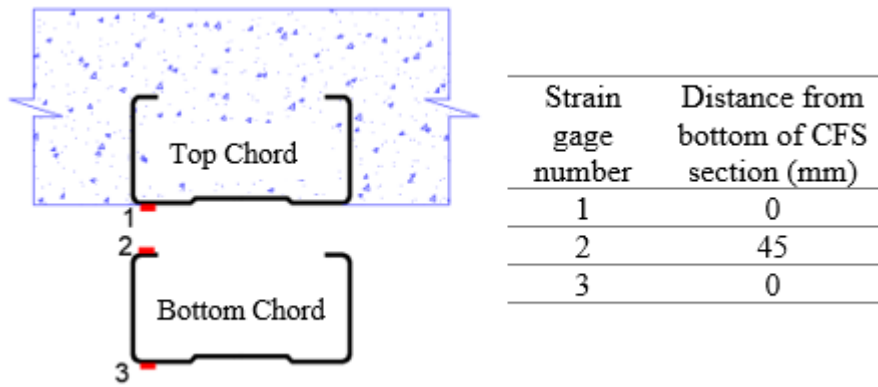
**3.2.2.4. Specimen WB\_Slab**

Numerical response obtained from the FE model of the truss specimen tested with a 600 mm wide by 80 mm thick concrete slab is presented in this section. The numerically determined load-deflection response from GMNA is given in Figure 63 together with the experimental response. Location of strain gages in specimen WB\_Slab is shown in Figure 64 and the data obtained from these gages are presented in Figure 65–67.

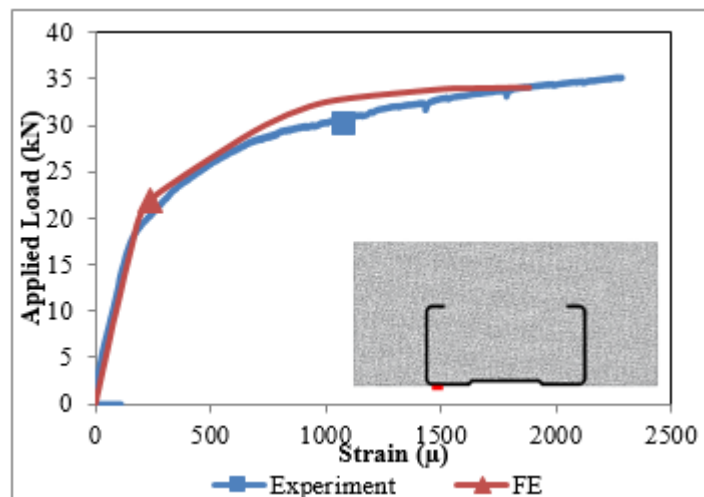


**Figure 63.** Measured and predicted load-deflection response of specimen WB\_Slab

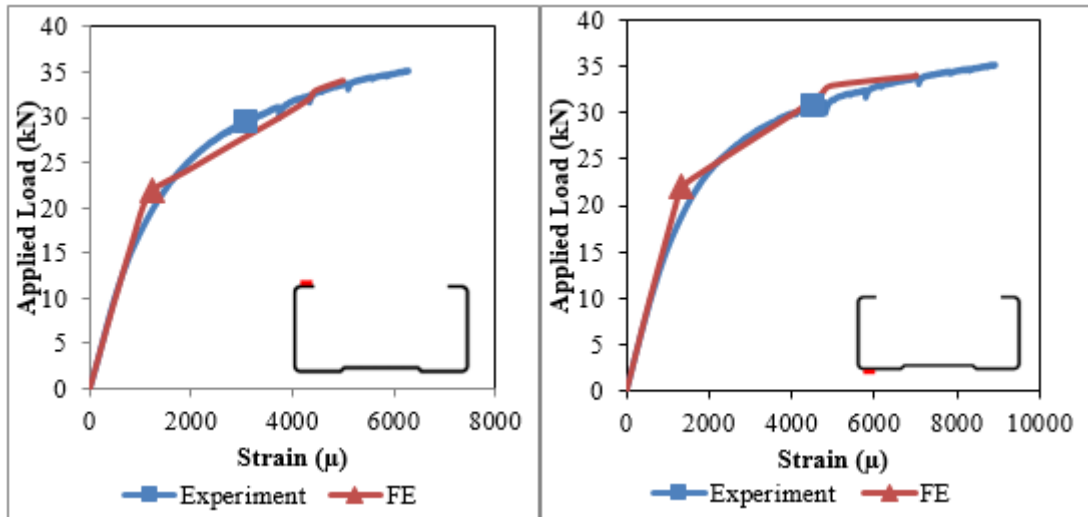
Even though the FE model slightly overpredicts the truss stiffness the overall response is accurately captured, as evident in Figure 63. The numerical solution suffered from convergence problems and the analysis was terminated at a midspan deflection value of 92 mm. The numerically determined load-deflection curve deviated from the initial linear response at a load of 17 kN. Similar type of behavior is also evident in the top and bottom chord local strain responses shown in Figure 65 and 66. The significantly high strain values indicate material yielding in both the top chord and bottom chord CFS members. This is valid for both the experimentally determined and numerically predicted strain responses.



**Figure 64.** Specimen WB\_Slab strain gage locations

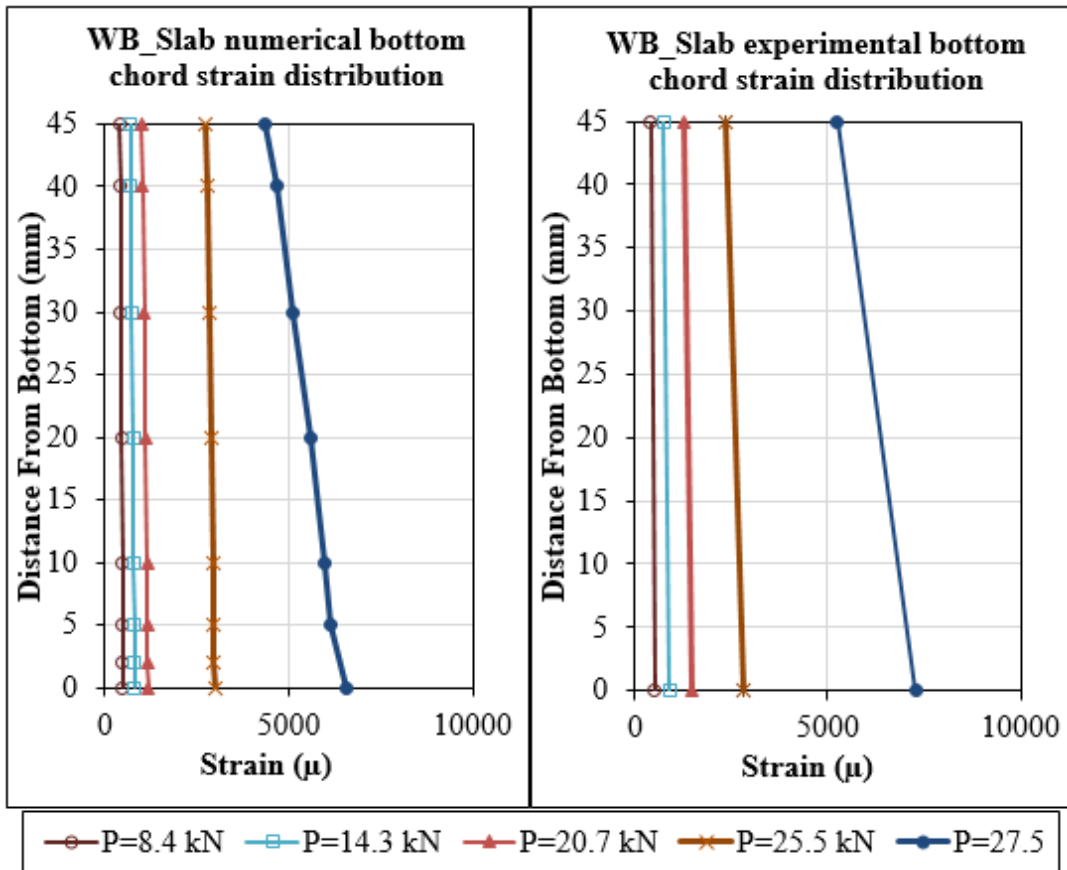


**Figure 65.** Top chord load-strain response in specimen WB\_Slab



**Figure 66.** Bottom chord load-strain response in specimen WB\_Slab

As observed for the previously explained specimens, the strain response for chord members closely resembles the experimentally obtained results for specimen WB\_Slab. Numerically determined strain profiles under different load levels for both chord members are presented in Figure 67. A slight increase in strain gradients is observed for both chord members prior to yielding of the material, indicating an increasing bending effect with the loading. The strain gradient increases significantly following the yielding of the bottom chord.



**Figure 67.** Specimen WB\_Slab bottom chord midspan strain values; experiment vs. model values

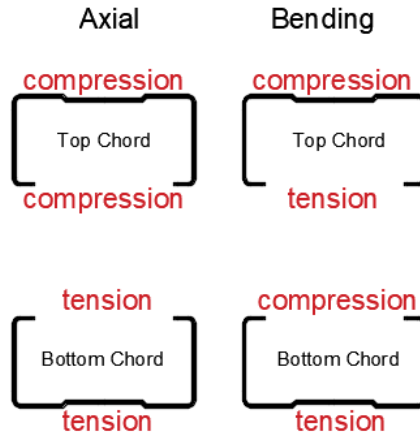


## CHAPTER 4

### ANALYTICAL STUDIES

Experimental and numerical behavior of CFS trusses with concrete infilled top chord and concrete slab are explained in earlier chapters. To predict the behavior of these trusses without the need of such a detailed analysis, an analytical study has been conducted. This chapter explains the procedures on predicting the cross-sectional strains in CFS chord members, as well as the yield and ultimate load capacities of trusses.

The analysis is based on determining the cross-sectional strains in CFS chord members due to normal force and bending moment. As explained earlier, the top and bottom chord members in CFS trusses are subjected to bending moments in addition to normal forces as shown in Figure 68. Under gravity loading the axial force is tension in the bottom chord and compression in the top chord. Due to bending effect, on the other hand, the lower fibers in both chord members are in tension while the upper fibers are in compression. Based on this observation, the chord strain values measured during the experiments and those obtained from FE models were verified using a simple mechanics approach. Furthermore, important response parameters in load-displacement behavior of trusses were verified using similar approaches. For the load-displacement behavior, the initial stiffness as well as the yield and ultimate load values were analytically determined and these values were compared with the experimental results.



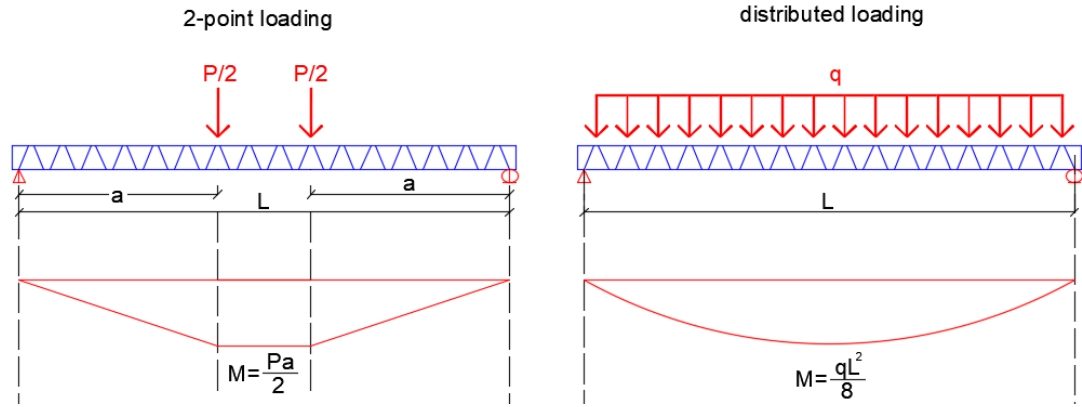
**Figure 68.** Cross-sectional strains due to axial and bending effects

#### 4.1. Calculation of Cross-Sectional Strains

The externally applied load on trusses induces both axial strain and bending strain on chord members. The chord strains were estimated by calculating the sum of strains due to these two effects. The axial strain component was calculated by first computing the axial force developed on the chord due to the external moment:

$$\varepsilon_{axial} = \frac{M_{truss}}{dEA} \quad (4)$$

where,  $d$  is the distance between the centroids of top and bottom chord,  $M_{truss}$  is the external moment acting on the truss at the midspan section,  $E$  is the modulus of elasticity for steel and  $A$  is the cross-sectional area of the chord members. The external moment  $M_{truss}$  was evaluated considering the principles of statics as illustrated in Figure 69.



**Figure 69.** Truss external moment due to two-point and distributed loading

The bending strain in chord members was calculated by making use of the vertical deflections measured at the midspan section of truss specimens. Assuming that the midspan deflection of the truss is equal to the midspan deflection of the chord member itself, the chord bending moment ( $M_{chord}$ ) and the corresponding curvature were calculated. Value of chord bending moment ( $M_{chord}$ ) that would result in a vertical deflection of  $\Delta$  at midspan section can be calculated using Equations 5 and 6, assuming two-point loading and distributed loading, respectively. Two-point loading represents the externally applied load acting on the truss specimens during the experiments. On the other hand, the reaction forces that develop on the chord members at the diagonal-to-chord joints resulted in distributed type of loading on these members. For these reasons, both of these loading types were considered in the analytical studies.

$$\frac{M_{chord}}{EI} = \frac{24\Delta}{(3L^2 - 4a^2)} \quad 2 - point \text{ loading} \quad (5)$$

$$\frac{M_{chord}}{EI} = \frac{384\Delta}{40L^2} \quad distributed \text{ loading} \quad (6)$$

In Equations 5 and 6,  $EI$  and  $L$  represent the flexural rigidity and the length of CFS chord members, respectively, while  $a$  represents the length of shear span in the case

of a 2-point loading. It should be noted that for trusses with concrete infilled top chord or with a concrete slab, transformed section was used to determine the geometric properties. The chord bending moment determined this way can then be used in Equation 7 to calculate the chord bending strain at the midspan cross section at a location  $y$  distance away from the centroid of chord CFS section.

$$\varepsilon_{bending} = \frac{M_{chord}}{EI} y \quad (7)$$

$$\varepsilon_{total} = \varepsilon_{axial} + \varepsilon_{bending} \quad (8)$$

The axial and bending strains calculated following the procedures outlined above were combined together to determine the total chord strains (Equation 8). These analytically determined chord strains are presented in the form of plots in following sections. The strain profiles were evaluated at two different load levels. The former of the load levels used in these plots corresponds to the linear response of trusses while the latter one corresponds to the condition where the global load-deflection response is nonlinear. Each plot includes analytically determined cross-sectional strain profiles based on the assumptions of two-point loading and distributed loading. Superimposed on some of the plots are the cross-sectional strains from FE models and truss load tests.

#### 4.1.1. Bare CFS Trusses

Analytically determined chord strains for trusses with no concrete infill (WT\_Control and WB\_Control) are presented respectively in Figure 70 and Figure 71. The strain data from the FE model and the experimentally obtained strain values are also presented. These plots indicate that the analytical procedure explained in the previous section provides relatively accurate estimation of cross-sectional strain profiles for both the top and bottom chord CFS members when compared to the experimental results as well as those from the FE models. The plots also indicate that for both the

web-top and web-bottom orientations of the top chord CFS member, two-point loading assumption resulted in slightly better agreement with the FE and experimental results, especially for the bottom chord member. For the web-bottom orientation of the top chord member (truss WB-Control) the analytical procedure resulted in relatively smaller curvatures than the FE results. This indicates that chord bending moments are underestimated by the proposed procedure.

Details of the top chord cross-sectional strain calculations for truss WT\_Control are presented in Table 2. Similar calculations were applied to all trusses to estimate the cross-sectional strains.

**Table 2.** Details of cross-sectional strain calculations

P (kN)	Defl. (mm)	$M_{truss}$ (N.mm)	E (MPa)	d (mm)
8.0	19.7	5812291	200000	271.3
Distributed Loading		Curvature=5.62E-06 /mm		
Distance From Bottom (mm)	Measured Strain ( $\mu\epsilon$ )	Axial Strain ( $\mu\epsilon$ )	Bending Strain ( $\mu\epsilon$ )	Total Strain ( $\mu\epsilon$ )
43	616	350	161	512
45	714	350	172	523
37.8	587	350	132	482
23.8	547	350	53	403
5.4	505	350	-50	300
0	261	350	-80	270
2-Point Loading		Curvature=6.14E-06 /mm		
Distance From Bottom (mm)	Measured Strain ( $\mu\epsilon$ )	Axial Strain ( $\mu\epsilon$ )	Bending Strain ( $\mu\epsilon$ )	Total Strain ( $\mu\epsilon$ )
43	616	591	176	767
45	714	591	188	779
37.8	587	591	144	735
23.8	547	591	58	649
5.4	505	591	-54	536
0	261	591	-87	503

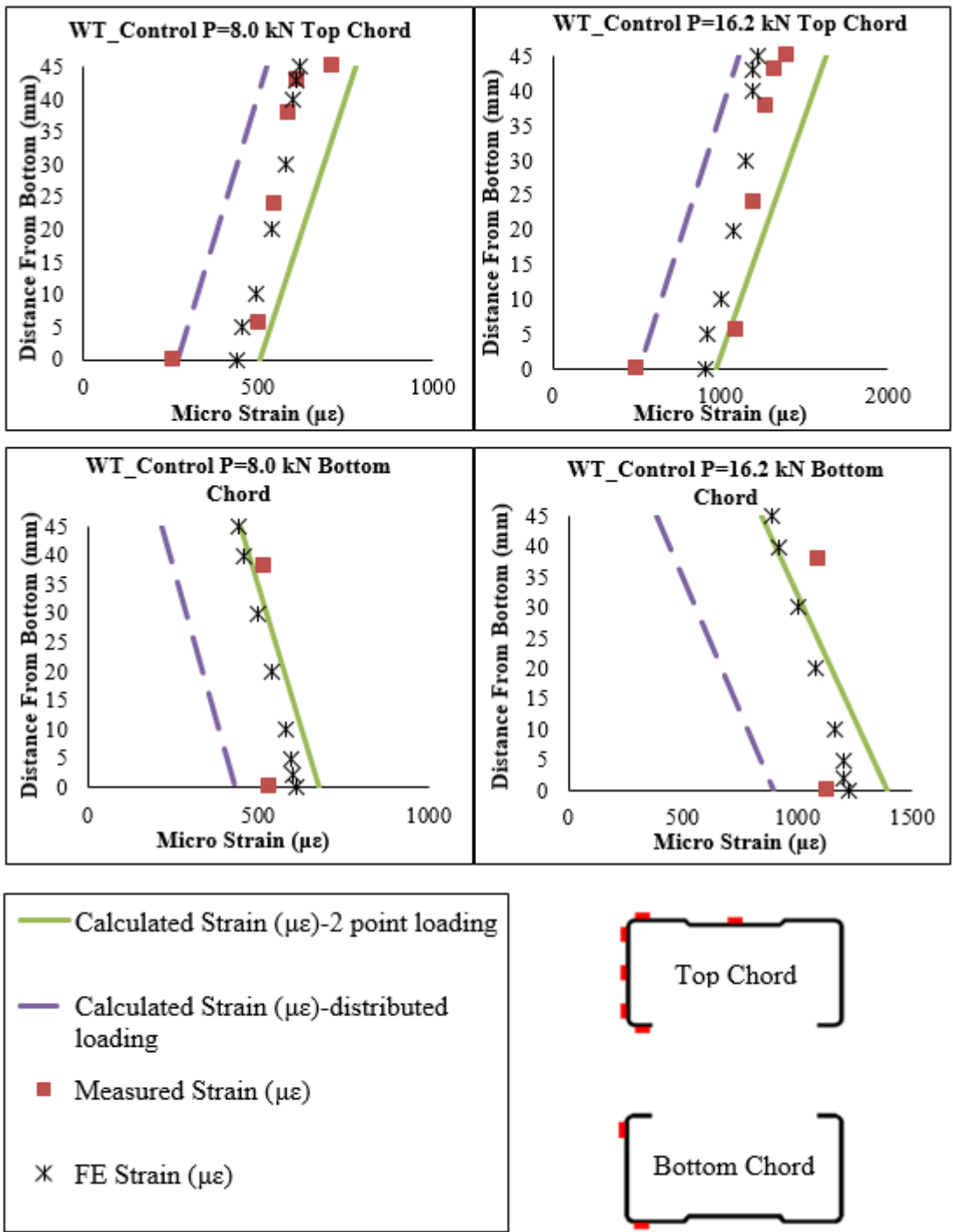
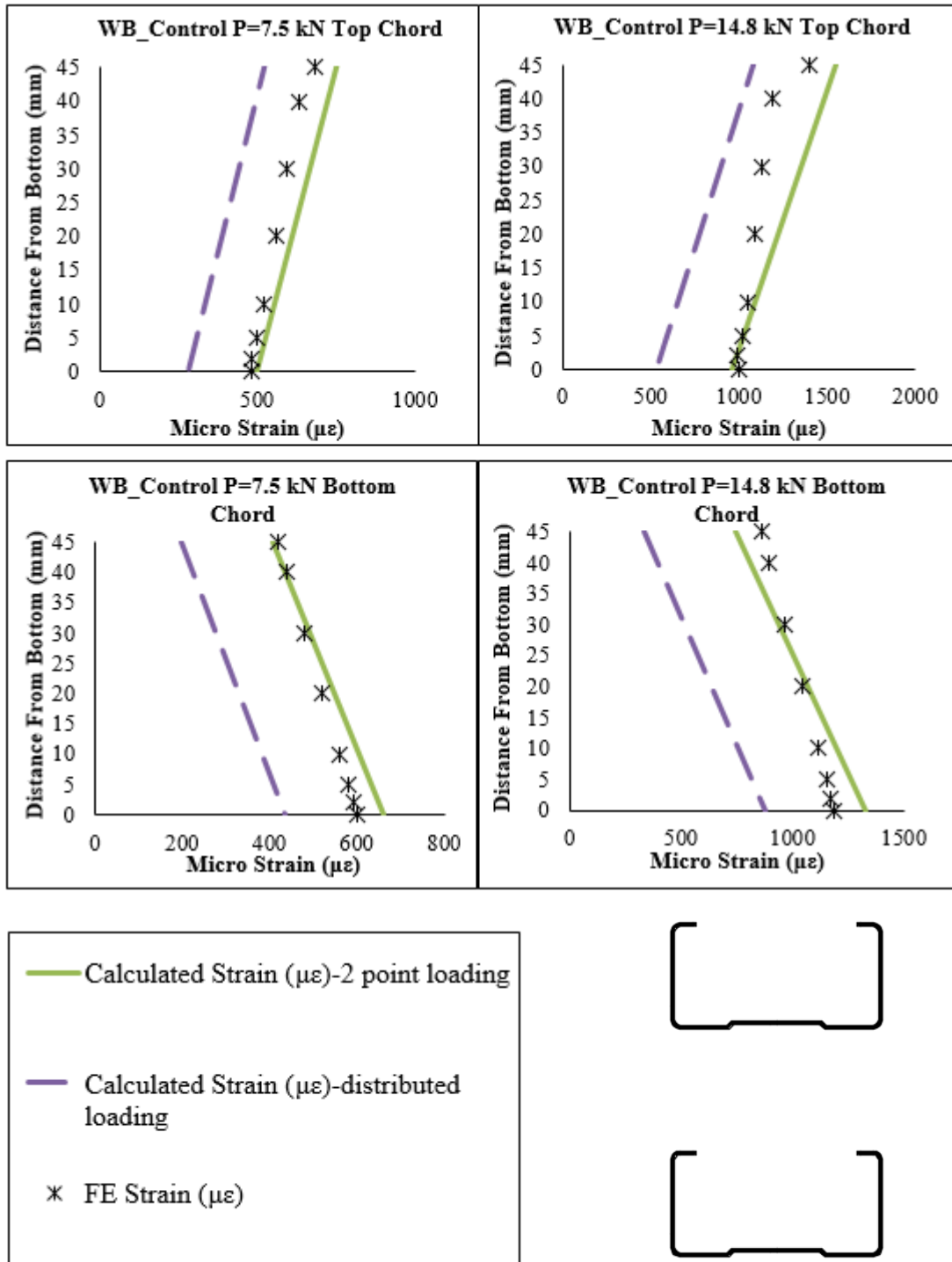


Figure 70. Truss WT\_Control comparison of estimated chord strains

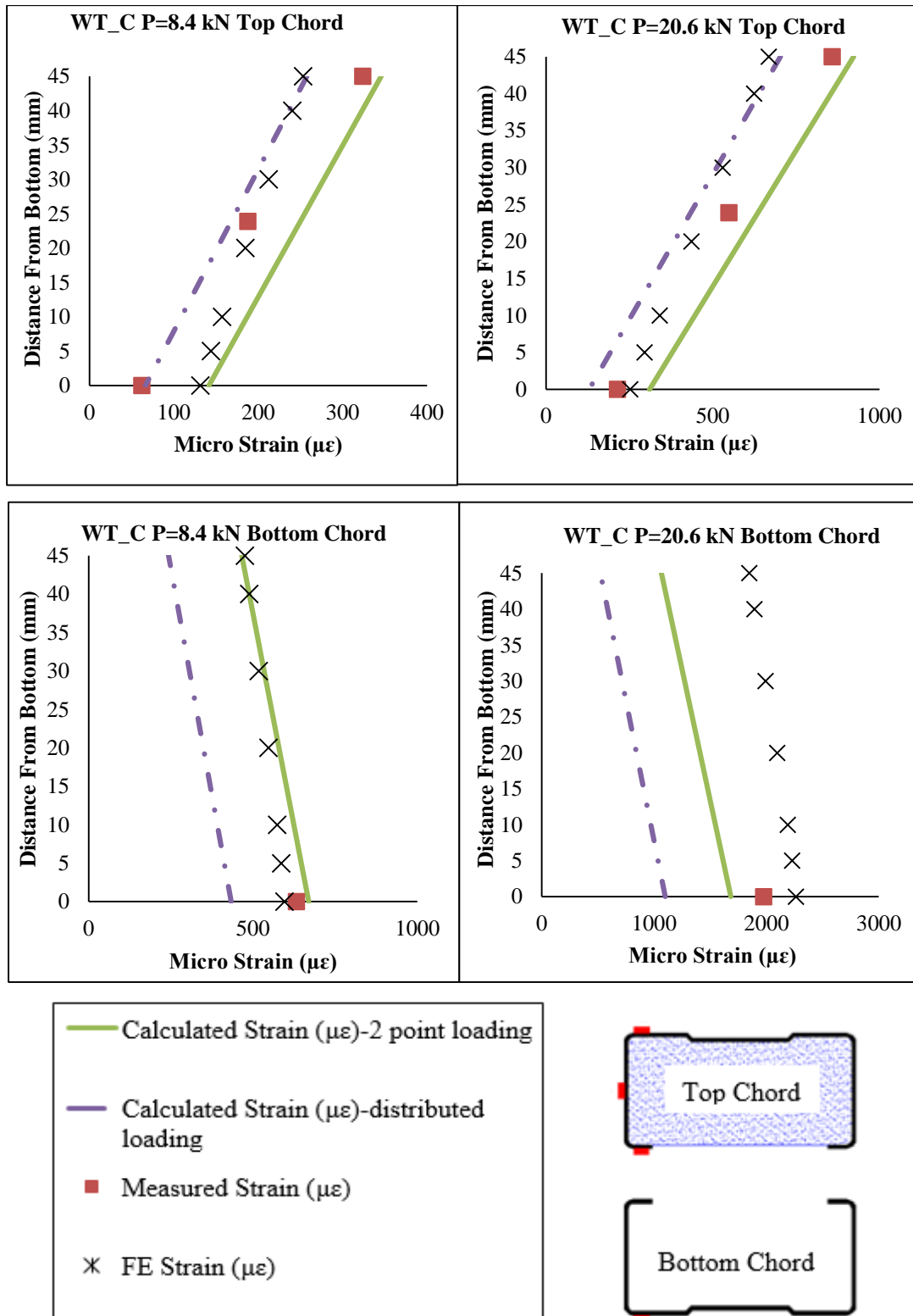


**Figure 71.** Truss WB\_Control comparison of estimated chord strains

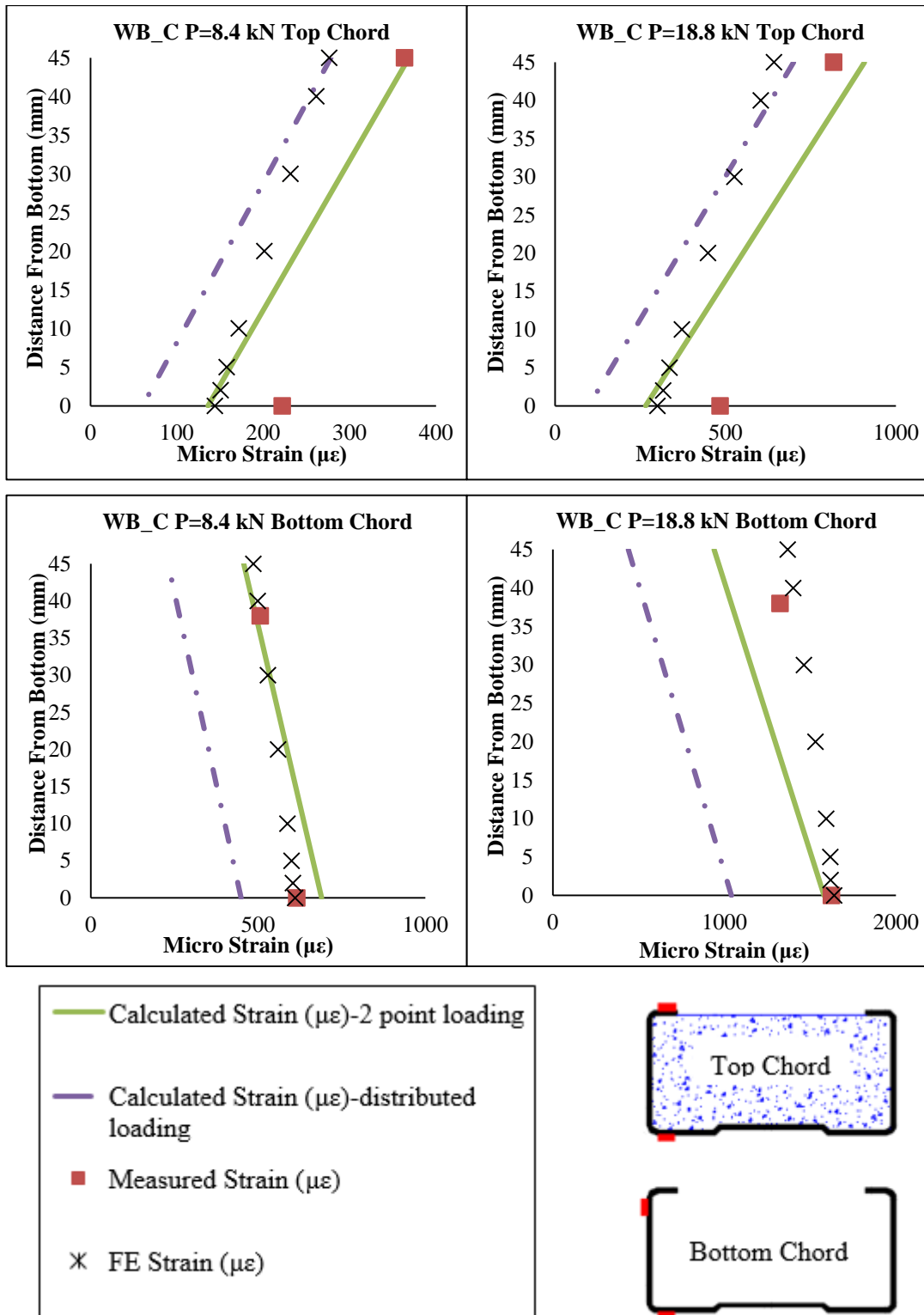
#### **4.1.2. Concrete Infilled Trusses**

The analytically determined chord strain profiles for trusses with concrete infilled top chord are provided in Figure 72 for web-top orientation and in Figure 73 for web-bottom orientation. Generally, an acceptable match between the cross-sectional strain profiles determined from FE models and those determined from the proposed analytical procedure is evident in results. The analytically determined cross-sectional strain profiles seem to be off for bottom chord members especially when the level of load gets close to the load capacity of trusses. This is due to the fact that significant bottom chord yielding was observed in trusses with concrete infilled specimens during experiments and also in FE models. The proposed analytical method, on the other hand, is based on linear elastic response. This is the source of discrepancy between the analytically determined strain values and those obtained from FE models and experiments.





**Figure 72.** Truss WT\_C comparison of estimated chord strains

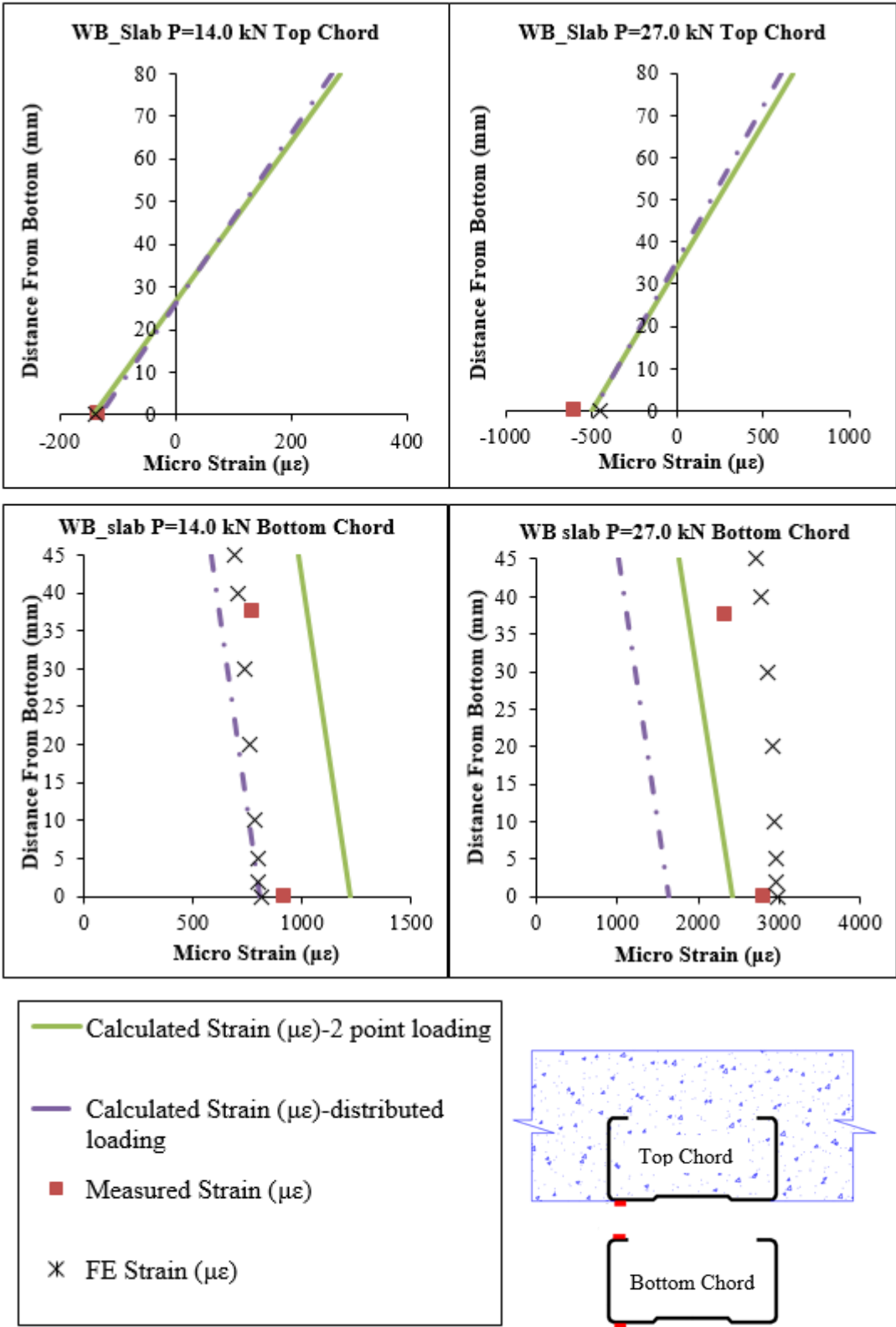


**Figure 73.** Truss WB\_C comparison of estimated chord strains

#### **4.1.3. Truss with Concrete Slab**

The bottom chord cross-sectional strains determined using the proposed analytical procedure for the truss that has a concrete slab placed on top (truss WB\_Slab) are presented in this section. The top chord CFS member in this truss is embedded inside the concrete slab. Different from the other trusses investigated, the top chord member in truss WB\_Slab is under the effect of tensile forces, because the neutral axis is located inside the concrete slab. In this case, the internal compressive effects are resisted by not only the top chord CFS member as in the case of other trusses, but by part of the concrete slab. For this reason, the top chord cross-sectional strains were not studied for this truss configuration.

Cross-sectional strain profiles for the bottom chord CFS member are given in Figure 74. The FE and experimental results are also superimposed on the plots. In the elastic range (i.e.,  $P=14.0$  kN) the analytical strain profile based on distributed loading agrees well with the strain values determined from the FE model. When the truss is loaded beyond the elastic limit (i.e.,  $P=27.0$  kN), the proposed analytical method underestimates the cross-sectional strains when compared to FE and experimental results. As mentioned earlier, such discrepancy in strain values occurs as a result of the fact that the proposed method does not consider the bottom chord yielding and cannot capture the inelastic response that was observed in experiments and FE models. Therefore, the proposed method can accurately be used to predict the truss response as long as it is within linear elastic range.



**Figure 74.** Truss WB\_slab comparison of estimated chord strains

## 4.2. Truss Stiffness and Load Capacity Predictions

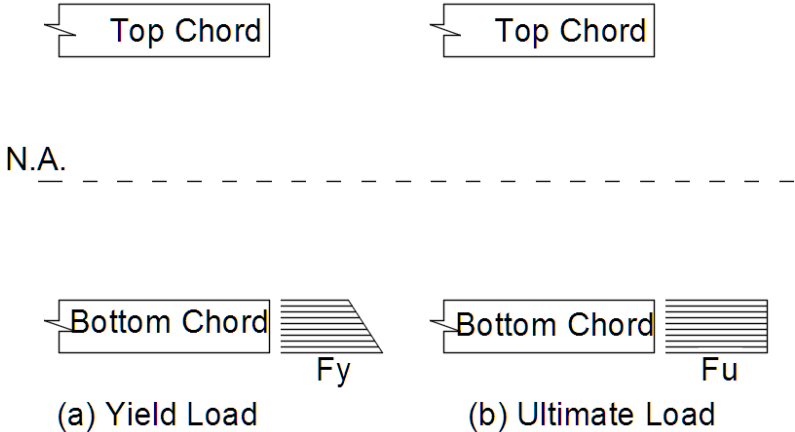
In the previous section, it has been shown that chord strains calculated based on the proposed analytical procedure agree both with the experimental results and the finite element estimations. Using the calculated chord strain values, it is possible to calculate the load capacity of trusses corresponding to the limit state of bottom chord yielding. Since it is known that the maximum tension is observed at the bottom chord, by assuming yield strain at this point, the load that causes this failure can be calculated. Knowing that the 2-point loading assumption provides a good estimation for the bottom chord cross-sectional strains, the calculations were followed by this assumption. The total strain at the maximum tension location of the bottom chord member was determined following the procedure outlined in the previous section. The loading that will cause the bottom chord to yield was calculated by assuming the midspan bottom chord maximum tension strain value to be equal to yield strain as shown in Figure 75(a). It is important to mention that the additional external moment due to self-weight of the specimen was included in the calculations. The truss self-weight was considered as a distributed load.

The analytically determined yield load of trusses was compared with the yield load determined based on experimental data. In order to extract the truss yield load from the experimental data, strain gage readings taken from the bottom part of the CFS section in bottom chord member were used. A yield strain value of  $1750 \mu\epsilon$  was utilized. It should be noted that the experimentally determined yield load is not available for truss specimen WB\_C\_100, as no strain gage was used on this specimen during load tests.

The moment of inertia of truss cross section was calculated by considering the top and bottom chords only, without taking the diagonal members into consideration. Transformed section approach was used to determine the geometric properties of trusses with concrete infilled top chord or with a concrete slab.

The initial truss stiffness was determined as the ratio of the yield load and the deflection value calculated at the yield load. Earlier research on similar trusses [30] have concluded that the flexibility of the connection between the diagonal and chord members depends on the number of rivets and screws used for the connection details.

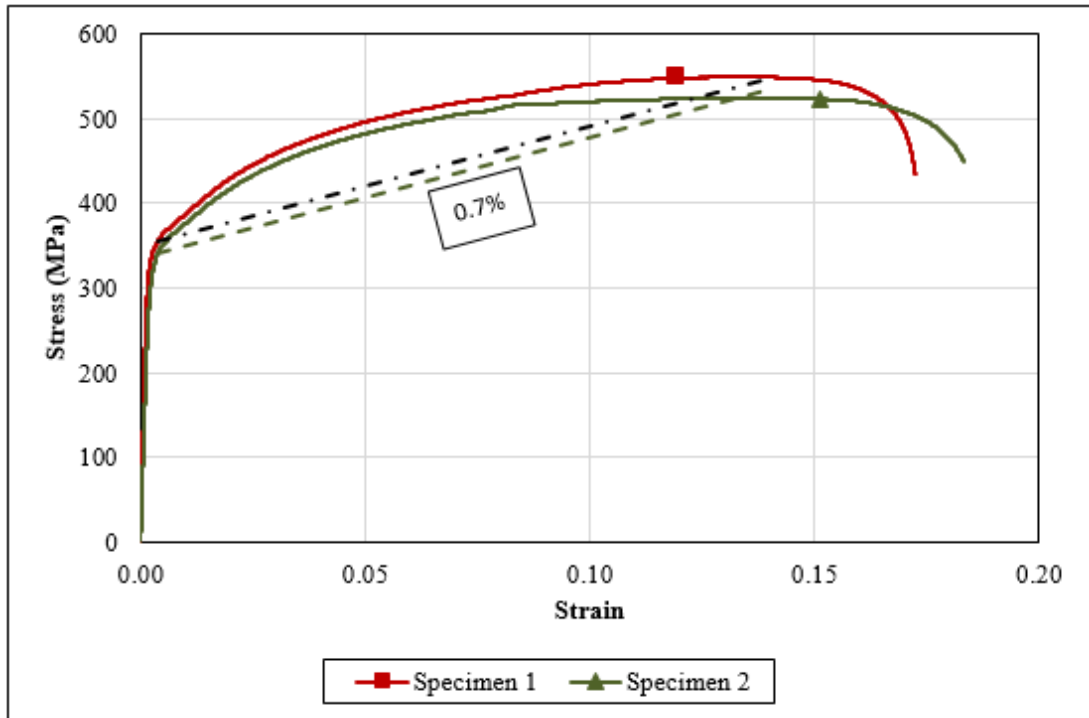
With a connection formed by two rivets and four screws it was estimated that the truss stiffness is approximately 80% of that based on the axially rigid connection assumption. In order to consider the effect of connection flexibility, the computed moment of inertia of the truss cross section was reduced by 20%. Experimental results obtained from bare steel trusses show that the measured truss stiffness agrees well with the stiffness value that is equal to 80% of the calculated truss stiffness.



**Figure 75.** Schematic analytical calculation assumptions: (a) yield load, (b) ultimate load

The theoretical ultimate load capacity of trusses corresponds to the bottom chord stress distribution shown in Figure 75(b). Loading of truss specimens was terminated when significant levels of midspan deflection were achieved. At this stage, the theoretical ultimate load capacity of trusses was not reached as the stress distribution in bottom chord members was somewhere between the two distributions shown in Figure 75. In order to determine the maximum value of tensile stress in bottom chord member at the end of load testing strain gage readings taken from the bottom part of the bottom chord CFS member were used. Experimentally determined bottom chord maximum tensile strains are reported in Table 3. A hardening modulus that is equal to 0.7% of the initial modulus of elasticity was used to determine the bottom chord tensile stress values corresponding to the experimentally determined maximum strain values. The hardening modulus is determined considering the yield and ultimate

strength points obtained from the coupon tests. This approach is illustrated in Figure 76. The maximum bottom chord tensile stress values determined this way are also reported in Table 3.



**Figure 76.** Determination of maximum bottom chord stress using idealized stress-strain behavior

**Table 3.** Estimated maximum strain and strength values

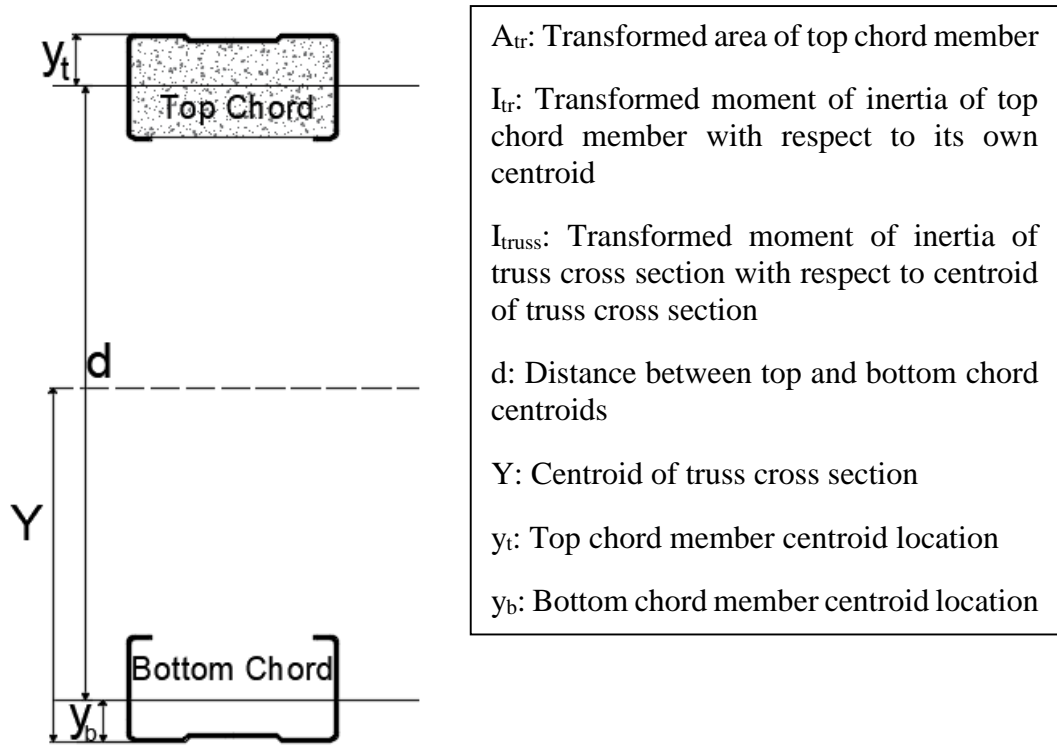
Truss Configuration	Maximum Strain $\epsilon_{\max}$ ( $\mu\epsilon$ )	Maximum Stress $f_{\max}$ (MPa)
WT_C	6500	416
WB_C	6700	419
WB_Slab	9200	447

The axial force in bottom chord corresponding to the stress distribution shown in Figure 75(b) was calculated considering the maximum stress values shown in Table 3. The calculated bottom chord axial force values were then utilized to determine the

corresponding truss external loading using Equation 9. In this equation  $f_{max}$  is the maximum tensile stress in bottom chord,  $A_{chord}$  is the bottom chord cross-sectional area and  $d$  is the distance between the top and the bottom chord centroids. The truss maximum load determined following this analytical procedure was compared to the experimentally determined maximum load of each truss specimen.

$$M_{truss} = f_{max}A_{chord}d \quad (9)$$

The cross-sectional geometric properties used in the analytical procedures explained above are illustrated in Figure 77 and the corresponding values are given in Table 4.



**Figure 77.** Cross-sectional geometric properties for trusses



**Table 4.** Truss cross-sectional properties

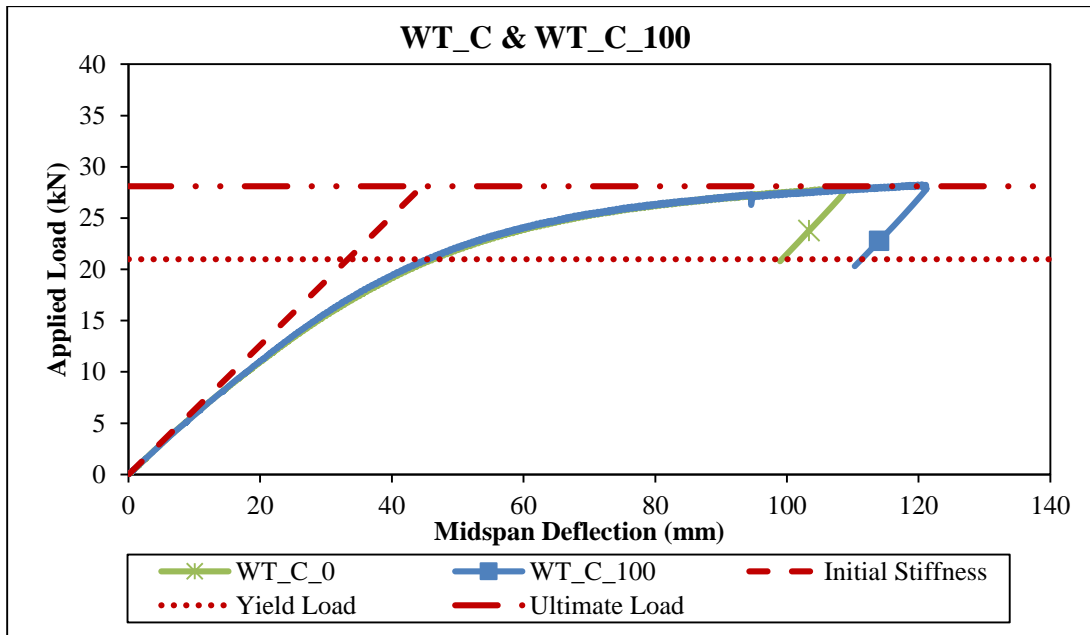
Truss Configuration	$A_{tr}$ (mm <sup>2</sup> )	$I_{tr}$ (mm <sup>4</sup> )	$I_{truss}$ (mm <sup>4</sup> )	E (MPa)	d (mm)	Y (mm)	$y_t$ (mm)
WT_C	5680	1136044	103881673	31800	266.0	212.6	19.7
WB_C	5680	1136044	99633972	31800	260.4	208.5	25.3
WB_Slab	49938	$27340 \times 10^3$	$173931 \times 10^3$	31800	303.0	283.7	40.9

\* For bare CFS cross section the area is equal to 308.25 mm<sup>2</sup>, the moment of inertia is equal to 79581 mm<sup>4</sup> and the centroid is located 14.32 mm from the web.

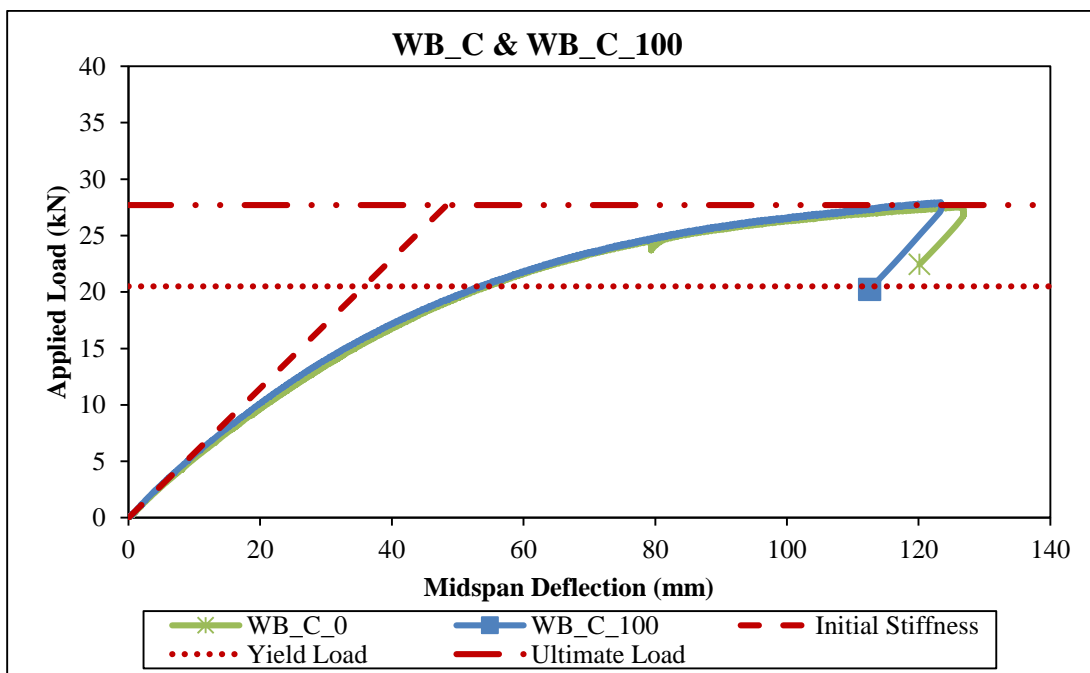
#### 4.2.1. Comparison of Analytically Determined and Measured Responses

The analytically determined initial stiffness, yield load and maximum load for truss configurations WT\_C, WB\_C and WB\_Slab are shown in Figures 78–80 together with the experimentally determined load-deflection response of the corresponding truss specimens. For all three truss configurations the initial stiffness and the maximum load values determined following the analytical procedure provide an accurate estimation of the response of test specimens. As indicated in Tables 5–7, the difference between the analytical and experimental maximum load values is less than 1%.

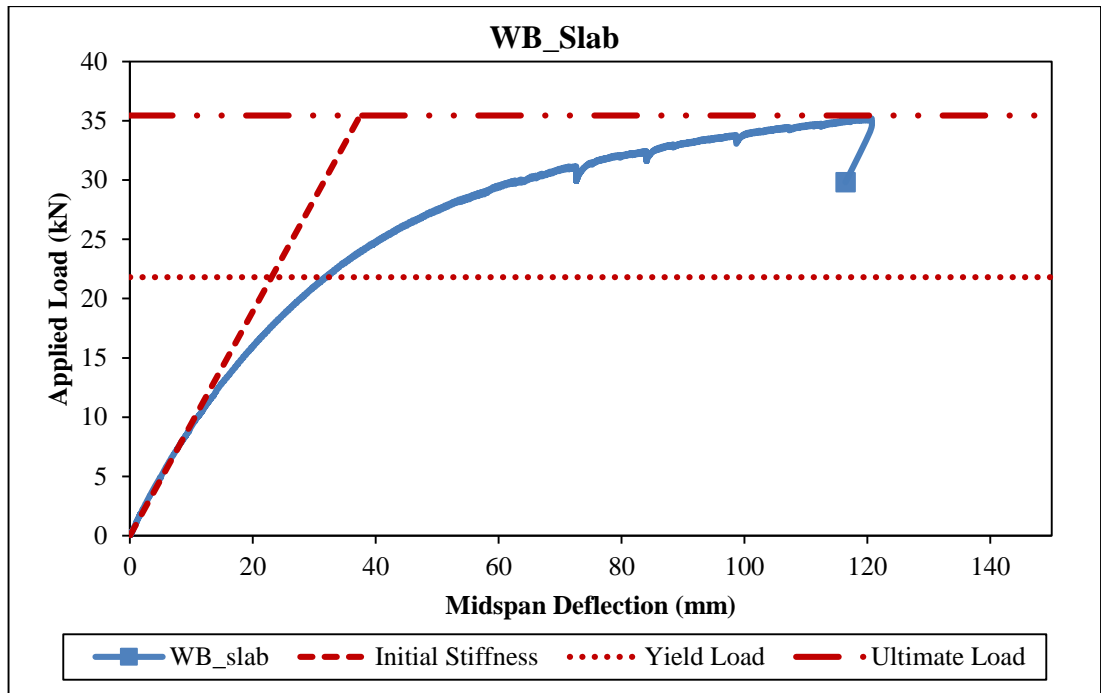
Another observation that is valid in Figures 78–80 is that the analytically determined yield load does not correspond to any definite yield point on the experimental load-deflection curve. For all five composite truss specimens analyzed here, the experimental load-deflection curve consists of two linear portions connected by a nonlinear portion. The transition between these portions is rather gradual with no distinct point marking the transition. The analytically determined yield loads fall within the nonlinear portion for all three truss configurations. The measured yield load is determined as the load at which the bottom chord maximum strain is equal to yielding strain, which is 1750  $\mu\epsilon$ . As presented in Tables 5–7, the analytical procedure is able to predict the yield load of truss specimens with differences changing between 1.8% and 8.5%.



**Figure 78.** Comparison of analytical and experimental responses for trusses WT\_C and WT\_C\_100



**Figure 79.** Comparison of analytical and experimental responses for trusses WB\_C and WB\_C\_100



**Figure 80.** Comparison of analytical and experimental responses for truss WB\_Slab

**Table 5.** Measured and the predicted yield and ultimate load values for trusses WT\_C and WT\_C\_100

Predicted Yield Load (kN)	Measured Yield Load (kN)	
21.0	WT_C	WT_C_100
	19.47	19.35
DIFFERENCE (%)	7.8	8.5
Predicted Ultimate Load (kN)	Measured Ultimate Load (kN)	
28.1	WT_C	WT_C_100
	27.9	28.3
DIFFERENCE (%)	0.7	0.7

**Table 6.** Measured and the predicted yield and ultimate load values for trusses WB\_C and WB\_C\_100

<b>Predicted Yield Load (kN)</b>	<b>Measured Yield Load (kN)</b>
20.5	19.69
DIFFERENCE (%)	4.1
<b>Predicted Ultimate Load (kN)</b>	<b>Measured Ultimate Load (kN)</b>
27.7	27.6
DIFFERENCE (%)	0.4

**Table 7.** Measured and the predicted yield and ultimate load values for truss WB\_Slab

<b>Predicted Yield Load (kN)</b>	<b>Measured Yield Load (kN)</b>
21.8	22.2
DIFFERENCE(%)	1.8
<b>Predicted Ultimate Load (kN)</b>	<b>Measured Ultimate Load (kN)</b>
35.4	35.2
DIFFERENCE (%)	0.5

## CHAPTER 5

### SUMMARY AND CONCLUSIONS

A combined numerical and experimental study was conducted to investigate the flexural behavior of steel-concrete composite trusses made of CFS sections. The trusses tested as part of the study were manufactured from 1.6 mm thick and 90 mm deep CFS lipped channel sections. The top chord members in composite specimens were filled with concrete in an attempt to control the local/distortional buckling mode that is observed in trusses with bare CFS chord members. The trusses were tested in pairs with the top chord CFS member looking up and looking down. One additional truss specimen was tested with a concrete slab of 80 mm depth and 600 mm width placed on top of the truss such that the top chord member is embedded inside the concrete.

Test results indicated that the two specimens tested with no concrete filling or concrete slab experienced local buckling of the top chord CFS member. Presence of concrete filling inside compression chord CFS section and the presence of concrete slab prevented the formation of top chord local/distortional buckling. In these specimens the failure mode was tension yielding of bottom chord CFS section. The bottom chord yielding is evident with the measured cross-sectional strains, as well as the highly ductile load-deflection response of specimens. With the introduction of top chord concrete filling and concrete slab, significant improvement in the truss response in terms of increase in stiffness and load capacity was obtained. No significant difference was observed in response of trusses tested with two different top chord member orientations. In specimens tested with concrete infilled top chord CFS member no relative slip was observed between the CFS member and concrete infill, indicating a proper force transfer and composite action between the two members. Concrete cracking starting at the bottom surface of the slab and extending

through the sides was observed during testing of the specimen that included a concrete slab placed over the CFS truss.

Finite element models of trusses were created using shell elements for chord members, beam elements for diagonal members and solid elements for concrete infill and concrete slab. Contact surfaces were defined between diagonal and web members, as well as between CFS and concrete parts. Three type of analysis, namely Materially Nonlinear Analysis (MNA), Geometrically and Materially Nonlinear Analysis (GMNA) and Geometrically and Materially Nonlinear Analysis with Imperfections (GMNIA), were conducted using the FE models. For the MNA model, only material nonlinearity was activated. For the GMNA model, both the material nonlinearity and the geometric nonlinearity were activated. The geometric nonlinearity was triggered by allowing large deformations in the model. In this analysis, second order effects and buckling deformations were also considered. In the GMNIA model the imperfections in CFS members were imposed in the model according to the determined eigenmodes of the system.

The FE models were able to predict the experimentally observed failure mode of trusses. The numerically determined load-deflection responses agreed well with the experimental response. All three types of analyses resulted in identical initial stiffnesses for all truss configurations studied. The difference between GMNIA and GMNA is visible only when the ultimate load is reached, in other words, when buckling occurs. When imperfections are present in the model the truss tends to fail at a slightly lower load and midspan deflection. The measured and numerically predicted behaviors of the specimens were also compared in terms of local chord strains. There was an acceptable agreement between the measured and predicted strain profiles at the top and bottom chord CFS members. Similar to the experimentally determined response, the FE models indicated strain gradients in top and bottom chord CFS members. This is an indication of the presence of bending effect in chord members in addition to pure axial force condition. While the FE model was able to simulate the strain distribution for stiffened elements at the compression chord CFS section, the measured and numerically predicted strain values differ significantly for the lip part of the section. The measured lip strains are significantly

smaller than those predicted by the FE model. This suggests that the lip part of the CFS section in compression chord does not resist stresses as effectively as the rest of the cross section. Although similar behavior was valid for trusses tested both with and without concrete infill, the difference in the concrete infilled specimens is not as critical. In models simulating trusses with concrete infilled top chord and concrete slab, significantly large tensile strains occur at the web part of bottom chord members, indicating the yielding of this member under load levels well below the experimentally measured maximum loads.

Additional analytical studies were conducted to predict the behavior of composite trusses without the need of a detailed analysis or load tests. The procedure adopted for the analytical approach is based on calculating the chord cross-sectional strain and then determining the yield and maximum load capacities using this strain information.

The chord strain values measured during the experiments and those obtained from FE models were verified using a simple mechanics approach. The externally applied load on trusses creates both axial strain and bending strain on chord members. The chord strains were estimated by calculating the sum of strains due to these two effects. The bending strain in chord members was calculated by making use of the vertical deflections measured at midspan section of truss specimens. Assuming that the midspan deflection of the truss is equal to the midspan deflection of the chord member itself, the chord bending moment and the corresponding bending strains were calculated. The results suggest that the proposed analytical procedure provides relatively accurate estimation of cross-sectional strain profiles for both the top and bottom chord CFS members when compared to the experimental results and those from the FE models. The analytically determined cross-sectional strain profiles seem to be off for bottom chord members in trusses with concrete infilled top chord and concrete slab, especially when the level of load gets close to the capacity of trusses. This is due to the fact that significant bottom chord yielding was observed in these trusses during experiments and also in FE models. The proposed analytical method, on the other hand, is based on linear elastic response.

The theoretical ultimate load capacity of composite trusses corresponds to the bottom chord stress distribution where all fibers reach to the ultimate strength of steel. Loading of truss specimens was terminated when significant levels of midspan deflection were achieved. At this stage, the theoretical ultimate load capacity of trusses was not reached as the stress level in fibers of the bottom chord CFS member was between the yield strength and the ultimate strength. In order to determine the maximum value of tensile stress in bottom chord member when the maximum load was reached, strain gage readings taken from the bottom part of the bottom chord CFS member were used. These experimentally determined bottom chord maximum tensile strains were then converted into stress values by assuming a slope for the hardening branch of the stress-strain behavior.

For all composite truss configurations, the initial stiffness and the maximum load values determined following the proposed analytical procedure provided an accurate estimation of the response of test specimens. The difference between the analytical and experimental maximum load values was less than 1% for all composite trusses studied. The analytically estimated yield loads did not correspond to any definite yield point on the experimental load-deflection curves. For all composite trusses the experimental load-deflection curve consisted of two linear portions connected by a nonlinear portion. The transition between these portions was rather gradual with no distinct point marking the transition. The analytically determined yield loads fell within the nonlinear portion for all three truss configurations.



## REFERENCES

- [1] W. Yu and R. A. LaBoube, *Cold-formed steel design*. Hoboken, NJ: John Wiley & Sons, 2010.
- [2] N. Duggal, M. A. Ahmetoglu, G. L. Kinzel, and T. Altan, "Computer Aided Simulation of Cold Roll Forming - A Computer Program for Simple Section Profiles," *J. Mater. Process. Technol.*, vol. 59, no. 1–2, pp. 41–48, 1996.
- [3] W. K. Kenneth, "Corner Properties of Cold-Formed Steel Shapes," *J. Struct. Div. Proc. Am. Soc. Civ. Eng.*, vol. 93, no. 1, pp. 401–432, 1967.
- [4] S. By, A. Chajes, K. W. Karren, and G. Winter, "Effects of Cold-Straining on Structural Sheet Steels," *J. Struct. Div. Proc. Am. Soc. Civ. Eng. Struct. Div. Proc. Am. Soc. Civ. Eng.*, vol. 89, no. 2, pp. 1–32, 1963.
- [5] W. K. Kenneth, M. ASCE, G. Winter, and F. ASCE, "Effects of Cold-forming on Light-gage Steel Members," *J. Struct. Div. Proc. Am. Soc. Civ. Eng.*, vol. 93, no. 1, pp. 433–469, 1967.
- [6] P. Kyvelou, L. Gardner, and D. A. Nethercot, "Composite Action Between Cold-Formed Steel Beams and Wood-Based Floorboards," *Int. J. Struct. Stab. Dyn.*, vol. 15, no. 08, p. 1540029, 2015.
- [7] C. C. Weng and T. Pekoz, "Residual Stresses in Cold-Formed Steel Members," in *International Specialty Conference on Cold-Formed Steel Structures*, 1988, no. 9.
- [8] E. M. Batista and F. C. Rodrigues, "Residual Stress Measurements on Cold-Formed Profiles," *Exp. Tech.*, vol. 16, no. 5, pp. 25–29, 1992.
- [9] N. Abdel-Rahman and K. S. Sivakumaran, "Material Properties Models for Analysis of Cold-Formed Steel Members", *J. of Struct. Eng.* vol. 123. no.9. 1997.

- [10] B. W. Schafer and T. Peköz, “Computational modeling of cold-formed steel: characterizing geometric imperfections and residual stresses,” *J. Constr. Steel Res.*, vol. 47, no. 3, pp. 193–210, 1998.
- [11] R. G. Dawson and A. C. Walker, “Post-buckling of geometrically imperfect plates,” *J. Struct. Div. Proc. Am. Soc. Civ. Eng.*, vol. 98, no. 1, pp. 75–94, 1972.
- [12] D. T. Dat and T. Peköz, “The strength of cold-formed steel columns,” *Center of Cold-Formed Steel Structures Library*. 110, 1980.
- [13] G. P. Mulligan and T. Peköz, “The influence of local buckling on the structural behavior of singly-symmetric cold-formed steel columns,” *Center of Cold-Formed Steel Structures Library*. 117, 1983.
- [14] *North American Specification for the Design of Cold Formed Steel Structural Members*. Washington DC, 2016.
- [15] S. Ádány, N. Silvestre, B. W. Schafer, and D. Camotim, “GBT and cFSM : Two Modal Approaches to the Buckling Analysis of Unbranched Thin-Walled Members,” *Advanced Steel Construction* vol. 5, no. 2, pp. 195–223, 2009.
- [16] G. Hancock, “Cold-formed steel structures,” *J. Constr. Steel Res.*, vol. 59, no. 4, pp. 473–487, 2003.
- [17] G. Winter, “Commentary on the 1968 Edition of the Specification for the Design of Cold-formed Steel Structural Members,” *AISI-Specifications Des. Cold-Formed Steel Struct. Members*, p. 102, 1970.
- [18] B. W. Schafer, “Review: The Direct Strength Method of cold-formed steel member design,” *J. Constr. Steel Res.*, vol. 64, no. 7–8, pp. 766–778, 2008.
- [19] C. Yu and W. Yan, “Effective Width Method for determining distortional buckling strength of cold-formed steel flexural C and Z sections,” *Thin Walled Struct.*, vol. 49, no. 2, pp. 233–238, 2011.
- [20] B. W. Schafer and T. Peköz, “Direct Strength Prediction of Cold-Formed Steel

- Members using Numerical Elastic Buckling Solutions,” in *Fourteenth International Speciality Conference on Cold-Formed Steel Structures*, 1998, p. 4.
- [21] B. W. Schafer, “Local, Distortional, and Euler Buckling of Thin-Walled Columns,” *J. Struct. Eng.*, vol. 128, no. 3, pp. 289–299, 2002.
- [22] J. V. Wood and J. L. Dawe, “Small-scale Test Behavior of Cold-Formed Steel Roof Trusses,” *J. Struct. Eng.*, vol. 132, no. April, pp. 608–615, 2006.
- [23] J. L. Dawe, Y. Liu, and J. Y. Li, “Strength and behaviour of cold-formed steel offset trusses,” *J. Constr. Steel Res.*, vol. 66, no. 4, pp. 556–565, 2010.
- [24] A. Hanaor, “Tests of composite beams with cold-formed sections,” *J. Constr. Steel Res.*, vol. 54, no. 2, pp. 245–264, 2000.
- [25] C. T. T. Hsu, S. Punurai, W. Punurai, and Y. Majdi, “New composite beams having cold-formed steel joists and concrete slab,” *Eng. Struct.*, vol. 71, pp. 187–200, 2014.
- [26] M. A. Youns, S. A. Hassaneen, M. R. Badr, and E. S. Salem, “Composite Beams of Cold Formed Steel Section and Concrete Slab,” *Int. J. Eng. Dev. Res.*, vol. 4, no. 4, pp. 165–177, 2016.
- [27] B. S. Lakkavalli and Y. Liu, “Experimental study of composite cold-formed steel C-section floor joists,” *J. Constr. Steel Res.*, vol. 62, no. 10, pp. 995–1006, 2006.
- [28] T. V. Ipe, H. S. Bai, K. M. Vani, M. Mohd, and Z. Iqbal, “Flexural behavior of cold-formed steel concrete composite beams,” *Steel Compos. Struct.*, vol. 14, no. 2, pp. 105–120, 2013.
- [29] S. Haris, Zaidir, R. Thamrin, and L. Buthi, “Bending capacity of composite cold-formed steel and concrete of a strip plate structure,” *Int. J. Civ. Eng. Technol.*, vol. 8, no. 10, pp. 1191–1198, 2017.
- [30] Ç. Dizdar, “Experimental and Analytical Investigation of Cold-Formed Steel

Floor Trusses Under Gravity Loading,” M.S. Thesis, Middle East Technical University, 2017.

[31] ANSYS® Academic Research Mechanical, Release 18.2.

[32] ANSYS® Academic Research Mechanical User Manual, Release 18.2.